

University of Southampton Research Repository ePrints Soton

Copyright © and Moral Rights for this thesis are retained by the author and/or other copyright owners. A copy can be downloaded for personal non-commercial research or study, without prior permission or charge. This thesis cannot be reproduced or quoted extensively from without first obtaining permission in writing from the copyright holder/s. The content must not be changed in any way or sold commercially in any format or medium without the formal permission of the copyright holders.

When referring to this work, full bibliographic details including the author, title, awarding institution and date of the thesis must be given e.g.

AUTHOR (year of submission) "Full thesis title", University of Southampton, name of the University School or Department, PhD Thesis, pagination

UNIVERSITY OF SOUTHAMPTON

FACULTY OF PHYSICAL AND APPLIED SCIENCES

School of Electronics and Computer Science

**Investigation of Nonlinear Processes and Device Designs Applicable to the
Creation of a Compact, Broadly Tunable Laser Based on a Tantalum Pentoxide
Planar Lightwave Circuit Platform**

by

Ruiqi Chen

Thesis for the degree of Doctor of Philosophy

December, 2010

UNIVERSITY OF SOUTHAMPTON

ABSTRACT

FACULTY OF PHYSICAL AND APPLIED SCIENCES

SCHOOL OF ELECTRONICS AND COMPUTER SCIENCE

Doctor of Philosophy

INVESTIGATION OF NONLINEAR PROCESSES AND DEVICE DESIGNS
APPLICABLE TO THE CREATION OF A COMPACT, BROADLY TUNABLE
LASER BASED ON A TANTALUM PENTOXIDE PLANAR LIGHTWAVE
CIRCUIT PLATFORM

by Ruiqi Chen

Nonlinear photonic devices utilize phase-matched parametric wavelength conversion in a nonlinear medium to create a widely tunable pulsed laser source. Currently most of nonlinear lasers are based on bulk optics or photonic fibres. Lasers based on bulk optics utilizing nonlinear crystals in conjunction with high intensity pulsed laser pumps, which are very powerful and often used as pump lasers for nonlinear experiments, but they are very large in size, and expensive to purchase. Although marketed as ‘turn key’ solutions, they require expert alignment, are difficult to use and are not suitable for deployment to environments other than environmentally stable optics labs. The photonic crystal fibres based lasers are very useful for optical communication purposes, but they are not as powerful as the bulk optics lasers and hard to be integrated with semiconductor devices due to their cylindrical structures. This thesis investigates the viability of creating an alternative widely tunable laser in a planar lightwave circuit (PLC) format. The overall aim of this project was to investigate the viability of creating a functional on-chip tunable laser, develop some of the key components, the base technologies required to do this job.

Required sub-components include efficient: supercontinuum generation, harmonic generation, and parametric wavelength conversion devices, all of which should ideally be powered by a compact, low cost, solid state pump source. To complicate matters further, requirements for parametric conversion include precise phase-matching of up to four participating beams, each of which may have a different wavelength. Furthermore, to provide broadband tunability, phase-matching condition must be maintained as the wavelengths of all participating beams are tuned. Hence the parametric conversion must take place in a device supporting ‘variable phase-matching’.

One of the key sub-components of a broadband tunable laser is a supercontinuum (SC) source. Supercontinuum (SC) generation is a nonlinear optical phenomenon that generates a spectrum across a wide range of frequencies. The SC component is itself very useful for many optical applications including: optical coherence tomography (OCT), frequency metrology, pulse compression, wavelength division multiplexing (WDM) and hence, attracts great research interests. Up to now, about 99% of the SC devices are based on optical fibres or nonlinear crystals. This thesis starts an in depth investigation of the generation of SC in planar waveguides reviewing the key linear and nonlinear optical effects associated with SC generation, making comparisons to prior literature.

All devices studied in this thesis were based on rib and ridge waveguides consisting of a tantalum pentoxide (Ta_2O_5) core and silicon dioxide (SiO_2) cladding materials. The simulated dispersion properties of such planar waveguides are presented. The experimental results on frequency tripling, SC generation and parametric effects along the waveguides are demonstrated. Further optimization procedures and potential applications are suggested subject to the current results and the nonlinear properties obtained from the Ta_2O_5 waveguide samples.

Contents

CHAPTER 1	INTRODUCTION	1
1.1	PROJECT AIM	3
1.2	THESIS OVERVIEW	5
CHAPTER 2	LITERATURE REVIEW	6
2.1	GROUP VELOCITY DISPERSION (GVD)	6
2.2	NONLINEAR OPTICAL EFFECTS	7
2.2.1	<i>Optical Kerr Effect</i>	8
2.2.2	<i>Self-Phase Modulation (SPM)</i>	9
2.2.3	<i>Optical Solitons</i>	11
2.2.3.1	Modulation Instability (MI)	12
2.2.3.2	Higher-Order Effects	13
2.2.4	<i>Stimulated Raman Scattering (SRS)</i>	14
2.2.5	<i>Cross-Phase Modulation (XPM)</i>	15
2.2.6	<i>Four-Wave Mixing (FWM)</i>	16
2.2.6.1	Third Harmonic Generation (THG)	18
2.2.7	<i>Stimulated Optical Parametric Amplification</i>	19
2.2.7.1	Review of Current Works	19
2.3	SUPERCONTINUUM (SC) GENERATION	20
2.3.1	<i>Pumping with Picosecond Pulses or CW Pulses</i>	21
2.3.2	<i>Pumping with Femtosecond Pulses</i>	23
2.3.3	<i>Other Issues Related to Supercontinuum</i>	24
2.3.4	<i>Supercontinuum (SC) Generation Applications</i>	25
2.3.4.1	Optical Parametric Oscillator/Amplifier (OPO/OPA)	25
2.3.4.2	Optical Coherence Tomography (OCT)	26
2.3.4.3	Frequency Metrology	27
2.3.4.4	Pulse Compression	28
2.3.4.5	Wavelength Division Multiplexing (WDM)	29
2.3.5	<i>Supercontinuum Generation in Different Guiding Mediums</i>	30
2.3.5.1	Conventional Fibres	30
2.3.5.2	Highly Nonlinear Fibres (HNLFs)	31
2.3.5.3	Planar Waveguides	38
CHAPTER 3	SIMULATION OF TANTALUM PENTOXIDE PLANAR WAVEGUIDE DISPERSION PROPERTIES	42
3.1	PLANAR WAVEGUIDE APPROACH	42
3.2	DISCUSSION OF NUMERICAL ACCURACY	44

3.3	SIMULATION RESULTS	45
3.3.1	<i>1-D Slab Waveguides</i>	45
3.3.2	<i>2-D Rib/Ridge Waveguides</i>	48
CHAPTER 4 NONLINEAR SUSCEPTIBILITY OF PLANAR WAVEGUIDES		58
4.1	THIRD-HARMONIC GENERATION AND MEASUREMENT OF CHI 3.....	58
4.1.1	<i>Planar Waveguide Samples</i>	60
4.1.2	<i>Experiment Setup</i>	60
4.1.3	<i>Third-Harmonic Generation (THG) Results</i>	61
4.2	CALCULATION OF THIRD-ORDER SUSCEPTIBILITY.....	62
4.2.1	<i>Chi 3 Calculations</i>	67
4.3	CHI 3 DISPERSION OF TANTALUM PENTOXIDE	69
4.4	SUMMARY	72
CHAPTER 5 EXPERIMENTAL RESULTS OF SUPERCONTINUUM GENERATION.....		74
5.1	SUPERCONTINUUM (SC) OUTPUT SPECTRA	75
5.1.1	<i>Output Spectra at ~1200 nm</i>	75
5.1.2	<i>Output Spectra at ~1600 nm</i>	81
5.2	RELATIONS BETWEEN OUTPUT SPECTRA AND MATERIAL PROPERTIES	85
CHAPTER 6 PUMP-PROBE EXPERIMENT ON PLANAR TANTALUM PENTOXIDE WAVEGUIDES.....		87
6.1	PUMP-PROBE EXPERIMENT SETUP	88
6.1.1	<i>Device Fabrication and Testing</i>	88
6.1.2	<i>Pump-Probe Setup</i>	89
6.1.2.1	<i>Pump and Seed Optical Path</i>	90
6.1.2.2	<i>Zero-Time Delay Detection</i>	90
6.1.2.3	<i>Results Collection</i>	93
6.2	PUMP-PROBE EXPERIMENT RESULTS	93
6.2.1	<i>Visible Seeding Results</i>	93
6.2.2	<i>IR Seeding Results</i>	98
6.2.3	<i>Four-Wave Parametric Amplification Gain from Er doped Tantalum Pentoxide ridge waveguide devices</i>	102
6.3	PUMP-PROBE EXPERIMENT RESULTS DISCUSSION	104
6.3.1	<i>Relationships between Output Intensity and Pump/Seed Intensity</i>	104
6.3.2	<i>Relationship between Output Intensity and Pump-Seed Phase-Matching condition</i>	106
6.4	SUMMARY	111
CHAPTER 7 FUTURE WORKS.....		112
7.1	OPTIMIZATION OF THIRD HARMONIC GENERATION (THG)	112
7.1.1	<i>Dual-Band Optical Coherence Tomography (OCT)</i>	114
7.1.2	<i>OCT with Fluorescence Detection</i>	115

7.2	OPTIMIZATION OF SUPERCONTINUUM (SC) GENERATION	115
7.3	OPTIMIZATION OF OPTICAL PARAMETRIC CONVERSIONS – VIABILITY OF LOW COST FULLY INTEGRATED ON-CHIP TUNABLE LASER	117
7.4	PHOTONIC CRYSTAL STRUCTURES DESIGNS	119
7.5	COMPUTATIONAL MODELLING OF PHOTONIC CRYSTAL DEVICES	123
CHAPTER 8	CONCLUSIONS	125
APPENDIX A:	TANTALUM PENTOXIDE AND TITANIUM DIOXIDE MATERIAL DISPERSION – EQUATIONS & PARAMETERS.....	127
APPENDIX B:	SILICON DIOXIDE MATERIAL DISPERSION – SELLMEIER EQUATION	129
APPENDIX C:	TELLURITE MATERIAL DISPERSION.....	130
APPENDIX D:	FINITE-DIFFERENCE TIME-DOMAIN (FDTD) METHOD	131
APPENDIX E:	SC OUTPUT SPECTRA	134
REFERENCES	135

List of Figures

FIGURE 1: EXAMPLE OPO/OPA SYSTEMS FROM NEWPORT CO. AND COHERENT INC. [1, 2]	2
FIGURE 2: SELF-PHASE MODULATION OF OPTICAL PULSE: (A) PULSE WAVEFORM AND (B) INSTANTANEOUS ANGULAR FREQUENCY/WAVELENGTH CHANGE [14].....	10
FIGURE 3: ILLUSTRATION OF OPTICAL SOLITONS EFFECT IN FIBRE [3]	11
FIGURE 4: TEMPORAL PULSE SHAPE VARIATION OF THE THIRD-ORDER OPTICAL SOLITON [14]	12
FIGURE 5: GROWTH OF SIDE-BAND COMPONENTS (INDICATED BY RED ARROWS) BY THE MODULATION INSTABILITY IN OPTICAL FIBRE WITH INPUT POWER: (A) LOW, (B) 5.5 W, (C) 6.1 W, AND (D) 7.1 W [14].....	13
FIGURE 6: RAMAN GAIN SPECTRUM OF SILICA GLASS [14]	14
FIGURE 7: FREQUENCY ARRANGEMENT OF FWM SATISFYING THE PHASE-MATCHING CONDITION IN ZERO-DISPERSION REGION: (A) NON-DEGENERATE CASE AND (B) DEGENERATE CASE [14]	17
FIGURE 8: GENERATED WAVE EFFICIENCY AS A FUNCTION OF CHANNEL SPACING [14]	18
FIGURE 9: SIMULATION RESULTS OF THE SPECTRAL AND TEMPORAL CHARACTERISTICS OF THE SC GENERATED BY SELECTED PUMP WAVELENGTHS IN A 2 M LONG PCF WITH 500 W – 20 PS INPUT (DASHED LINE INDICATES THE ZERO- DISPERSION WAVELENGTH) [11]	22
FIGURE 10: SIMULATION RESULTS OF THE SPECTRAL AND TEMPORAL CHARACTERISTICS OF THE SC GENERATED BY SELECTED PUMP WAVELENGTHS IN A 2 M LONG PCF WITH 10 kW – 50 FS INPUT (DASHED LINE INDICATES THE ZERO- DISPERSION WAVELENGTH) [11]	24
FIGURE 11: OPTICAL PATH OF AN OPA9400 (INSET: THE SCHEMATIC ILLUSTRATION OF AN OPA9400) [1].....	25
FIGURE 12: FREQUENCY COMB FROM A MODE-LOCKED LASER [34].....	28
FIGURE 13: DETERMINATION OF ABSOLUTE FREQUENCY OFFSET FROM ZERO BY MIXING TWO COMPONENTS OF AN OCTAVE- SPANNING SPECTRUM [34]	28
FIGURE 14: PRISM SEQUENCE HAVING NEGATIVE DISPERSION (THE PRISMS ARE USED AT MINIMUM DEVIATION AND ORIENTED SO THAT THE RAYS ENTER AND LEAVE AT BREWSTER'S ANGLE. THE ARRANGEMENT IS SYMMETRIC ABOUT THE PLANE MM') [39]	29
FIGURE 15: OPTICAL SPECTRA AT THE OUTPUT OF A 9 CM-LONG TAPERED FIBRE WITH A 2-MICRON WAIST. THE AVERAGE POWER WAS 380 MW, 210 MW, AND 60 MW FROM TOP TO BOTTOM ALONG WITH THE INPUT SPECTRUM AS THE FOURTH CURVE [51].....	31
FIGURE 16: CONTINUUM SPECTRA OF TAPERED FIBRE WITH CORE DIAMETER OF 0.92 MICRONS PUMPED BY 282 W PEAK POWER, 7 NS PULSES LASER AT 532 NM [52]	32
FIGURE 17: OUTPUT SPECTRA WITH A 10 M LONG FIBRE AND FOR INPUT PEAK POWERS OF 675 W, 225 W, AND 120 W (FROM TOP TO BOTTOM) [54].....	33
FIGURE 18: SUPERCONTINUUM SPECTRA AS FUNCTION OF CW INPUT POWER IN PCF LENGTH OF (A) 0.5, (B) 1.0, AND (C) 1.5 KM [55]	34

FIGURE 19: SC IN A 75 CM LONG PCF. DASHED CURVE SHOWS THE SPECTRUM OF THE 100 FS – 0.8 NJ INPUT PULSES [56]	34
FIGURE 20: SC SPECTRUM OUTPUT OF AN 8 MM TELLURITE PCF PUMPED BY 1.9 NJ, 100 FS LASER AT 1550 NM. SPECTRUM IS ANALYZED BY OPTICAL SPECTRUM ANALYZER (OSA) AND MONOCHROMATOR WITH LEAD SELENIDE (PbSe) OR MERCURY CADMIUM TELLURIDE (MCT) [57].....	35
FIGURE 21: CONTINUUM GENERATION IN THE CASE OF (A) SINGLE (532NM) AND (B) DUAL PUMP (532 AND 1064 NM) CONFIGURATION. PICTURE: DIFFRACTED BEAMS. GRAPH: CORRESPONDING RECORDED POWER SPECTRA. INSET: FAR FIELD PATTERN OF THE CORRESPONDING SINGLE MODE TRANSVERSE ENERGY DISTRIBUTION [58].....	36
FIGURE 22: MEASURED SUPERCONTINUUM SPECTRUM USING A 20 M PCF [59].....	37
FIGURE 23: SUPERCONTINUUM IMAGES UNDER LINEAR (LEFT), ELLIPTICAL (MIDDLE), AND CIRCULAR (RIGHT) POLARIZATION EXCITATION CONDITIONS [60].....	38
FIGURE 24: EFFECT OF INPUT POLARIZATION ON SC, AT THE DEGREE OF POLARIZATION OF (A) 0°, (B) 45°, (C) 90° WITH 200 FS – 56 MW INPUT PULSES (DASHED LINE INDICATES THE ZDW POSITION) [61].....	38
FIGURE 25: DISPERSION PROPERTIES OF THE 1 μM AND 1 X 1 μM RIB WAVEGUIDE WITH TANTALUM PENTOXIDE AS CORE MATERIAL, RIB (SOLID LINE) AND SLAB STRUCTURE (DASHED LINE) [12].....	39
FIGURE 26: AIR-TAFD ₅ -SiO ₂ PLANAR WAVEGUIDE: (A) RIDGE STRUCTURE WITH A = 4 μM, D = 1 μM, AND F = 0.5 μM (B) GVD PROPERTIES OF THE WAVEGUIDE [13].....	39
FIGURE 27: SC GENERATED 2 X 1.8 μM RIB WAVEGUIDE PUMPED AT 1.55 MICRONS [12].....	40
FIGURE 28: SC GENERATED IN THE AIR-TAFD ₅ -SiO ₂ RIDGE WAVEGUIDE: (A) SPECTRUM, INPUT (GREEN DASHED LINE) AND OUTPUT (RED SOLID LINE) (B) TEMPORAL SHAPE [13].....	41
FIGURE 29: LINEAR REFRACTIVE INDEX OF POTENTIAL CORE MATERIALS, SOLID LINES ARE REAL PART AND DASHED LINES ARE IMAGINARY PART OF THE REFRACTIVE INDEX [62-64].....	43
FIGURE 30: SLAB WAVEGUIDE (INSETS SHOW ELECTROMAGNETIC FIELD DISTRIBUTION OF TE AND TM MODES) [14].....	46
FIGURE 31: GVD CURVE OF THE SYMMETRICAL SLAB WAVEGUIDE WITH CORE THICKNESS OF 4 μM.....	47
FIGURE 32: ZDW VS. CORE THICKNESS FOR SYMMETRICAL SLAB WAVEGUIDE.....	48
FIGURE 33: CROSS-SECTIONAL VIEW OF THE 25% AND 50% ETCHED RIDGE WAVEGUIDES.....	49
FIGURE 34: FUNDAMENTAL TE MODE PROFILES AT INPUT WAVELENGTH OF 1 μM IN 2.0 X 1.8 μM RIDGE WAVEGUIDES WITH THE ETCHING PROFILES: (A) 25%, (B) 50%, (C) 75%, AND (D) 100% (I.E. RIB).....	51
FIGURE 35: GVD CURVES OF 2 X 1.8 μM RIDGE WAVEGUIDES WITH THE ETCHING PROFILES: (A) 25%, (B) 50%, (C) 75%, AND (D) 100% (I.E. RIB).....	53
FIGURE 36: ZWD VS. WIDTH WITH RESPECT TO THICKNESS OF THE 25% ETCHED RIDGE WAVEGUIDES.....	54
FIGURE 37: ZDW VS. WIDTH WITH RESPECT TO THICKNESS OF THE 50% ETCHED RIDGE WAVEGUIDES.....	54
FIGURE 38: ZDW VS. WIDTH WITH RESPECT TO THICKNESS OF THE 75% ETCHED RIDGE WAVEGUIDES.....	55
FIGURE 39: ZDW VS. WIDTH WITH RESPECT TO THICKNESS OF THE 100% ETCHED RIDGE WAVEGUIDES (RIB WAVEGUIDES)	55
FIGURE 40: ZDW VS. WIDTH WITH RESPECT TO THE ETCH PROFILE OF 1.2 μM THICK RIDGE WAVEGUIDES.....	56
FIGURE 41: EXPERIMENTAL SETUP FOR THE THIRD-ORDER NONLINEAR SUSCEPTIBILITY (INSET: SEM IMAGE OF CROSS- SECTIONAL VIEW).....	60

FIGURE 42: OUTPUT SPECTRUM OF IR AND THE CORRESPONDING GENERATED THG AT 2 MW PUMP POWER (INSETS ARE MODE IMAGES FROM EXPERIMENT AND SIMULATED MODE PROFILES OF IR AND VISIBLE OUTPUT MODES, RESPECTIVELY)	62
FIGURE 43: REFRACTIVE INDICES OF THE WAVEGUIDES AT CORRESPONDING WAVELENGTHS FROM SIMULATION	64
FIGURE 44: WAVE NUMBER DIFFERENCES OF THE WAVEGUIDES (INSETS: MODE IMAGES AND MODE PROFILES FROM EXPERIMENT AND SIMULATION, RESPECTIVELY)	65
FIGURE 45: SPECTRAL FITTING FOR IR OUTPUT SHOWN IN FIGURE 42	66
FIGURE 46: CALCULATED THIRD-ORDER NONLINEAR SUSCEPTIBILITY OF TANTALUM PENTOXIDE WAVEGUIDE SAMPLES. SAMPLE A: SOLID TRIANGLE (BLACK) FOR 1.5 MW AND OPEN TRIANGLE (RED) FOR 2 MW PUMP POWER; SAMPLE B: SOLID SQUARE (GREEN) FOR 1.5 MW AND OPEN SQUARE (BLUE) FOR 2 MW PUMP POWER. PURPLE DOTTED LINE INDICATES THE TREND OF THIRD-ORDER NONLINEAR SUSCEPTIBILITY CHANGES WITH WAVELENGTH.....	70
FIGURE 47: CONSTANT-INITIAL-STATE CURVES OBTAINED FROM MEASURED SPECTRA CORRESPONDING TO P1, P2, P3, P4, AND P5 FEATURES OF THE VALENCE BAND, FOR (A) STOICHIOMETRIC AND (B) REDUCED TANTALUM PENTOXIDE [92]	71
FIGURE 48: ESTIMATED (DASHED LINE) THREE-PHOTON RESONANCE PEAK OF THIRD-ORDER NONLINEAR SUSCEPTIBILITY OF Ta_2O_5 BASED ON EXPERIMENTAL RESULTS (SOLID LINE)	72
FIGURE 49: OUTPUT SPECTRA OF G5 AT 1195 NM: (A) AT DIFFERENT AVERAGE POWER LEVELS (B) SPECTRAL FITTING FOR 1.5 MW OUTPUT (INSET: MODE PROFILE IMAGE) (C) SPECTRAL FITTING FOR 2 MW OUTPUT (INSET: MODE PROFILE IMAGE)	77
FIGURE 50: OUTPUT SPECTRA OF G36 COUPLING POSITION 1 AT 1200 NM: (A) AT DIFFERENT AVERAGE POWER LEVELS (B) SPECTRAL FITTING FOR 1 MW OUTPUT (INSET: MODE PROFILE IMAGE) (C) SPECTRAL FITTING FOR 3 MW OUTPUT (INSET: MODE PROFILE IMAGE)	78
FIGURE 51: OUTPUT SPECTRA OF G36 COUPLING POSITION 2 AT 1200 NM: (A) AT DIFFERENT AVERAGE POWER LEVELS (B) SPECTRAL FITTING FOR 1 MW OUTPUT (INSET: MODE PROFILE IMAGE) (C) SPECTRAL FITTING FOR 3 MW OUTPUT (INSET: MODE PROFILE IMAGE)	79
FIGURE 52: OUTPUT SPECTRA OF G5 AT 1610 NM: (A) AT DIFFERENT AVERAGE POWER LEVELS (B) SPECTRAL FITTING FOR 1.5 MW OUTPUT (INSET: MODE PROFILE IMAGE) (C) SPECTRAL FITTING FOR 2 MW OUTPUT (INSET: MODE PROFILE IMAGE)	82
FIGURE 53: OUTPUT SPECTRA OF G36 COUPLING POSITION 1 AT 1610 NM: (A) AT DIFFERENT AVERAGE POWER LEVELS (B) SPECTRAL FITTING FOR 1 MW OUTPUT (INSET: MODE PROFILE IMAGE) (C) SPECTRAL FITTING FOR 2 MW OUTPUT (INSET: MODE PROFILE IMAGE)	83
FIGURE 54: OUTPUT SPECTRA OF G36 COUPLING POSITION 2 AT 1610 NM: (A) AT DIFFERENT AVERAGE POWER LEVELS (B) SPECTRAL FITTING FOR 1 MW OUTPUT (INSET: MODE PROFILE IMAGE) (C) SPECTRAL FITTING FOR 2 MW OUTPUT (INSET: MODE PROFILE IMAGE)	84
FIGURE 55: CROSS-SECTIONAL SEM IMAGES OF 7 MM LONG WAVEGUIDE SAMPLE FACETS AFTER EXPERIMENTS. ALL WAVEGUIDES HAVE THICKNESS OF 500 NM AND WIDTHS AS FOLLOWS: 6.6 μ M (TOP LEFT) G14, 9.41 μ M (TOP RIGHT) G20, 9.85 μ M (BOTTOM LEFT) G21, AND 11.65 μ M (BOTTOM RIGHT) G25 RESPECTIVELY	89

FIGURE 56: EXPERIMENTAL SETUP FOR THE ON-CHIP FOUR-WAVE PARAMETRIC AMPLIFICATION DEMONSTRATION. PUMP AND SEED BEAMS ARE BROUGHT TOGETHER AS A CO-LINEAR BEAM PAIR USING A REFLECTIVE BANDPASS FILTER (M8) BEFORE BEING COUPLED INTO THE WAVEGUIDE SAMPLES. THE OUTPUT CONSISTS OF RESIDUAL PUMP, RESIDUAL SEED, AND PARAMETRIC OUTPUT, WHICH PASSES THROUGH A KERR GATE WHEN REQUIRED, ARE COLLECTED BY MONOCHROMATOR AND IR/VISIBLE CAMERAS	89
FIGURE 57: EXPERIMENTAL SETUP OF THE ZERO-TIME DELAY DETECTION WITH OPTICAL PATH DISTANCE INFORMATION (UNIT: MM)	91
FIGURE 58: OPTICAL DELAY LINE POSITIONS FOR ZERO-TIME DELAY VS. SEED BEAM CENTRAL WAVELENGTHS.....	92
FIGURE 59: PARAMETRIC GAINS VS. VISIBLE SEED (SIGNAL) WAVELENGTHS OF STIMULATED FOUR-WAVE PARAMETRIC AMPLIFICATION FROM PLANAR Ta_2O_5 WAVEGUIDE G20. INSET: GUIDE LOSSES AT EXAMINED VISIBLE WAVELENGTHS	95
FIGURE 60: PARAMETRIC OUTPUT DATA OF GUIDE G25 FROM VISIBLE SEEDING. (A) PARAMETRIC OUTPUT SPECTRA FOR DIFFERENT PUMP POWER LEVELS WITH THE SAME SEED POWER INPUT (B) THEORY EXPECTATION (LINE) AND EXPERIMENTAL RESULTS (DOTS) OF INTENSITIES OF PARAMETRIC OUTPUTS VS. INPUT PUMP POWERS (C) THEORY EXPECTATION (LINE) AND EXPERIMENTAL RESULTS (DOTS) OF PEAK PARAMETRIC OUTPUT WAVELENGTH VS. INPUT SEED WAVELENGTH.....	97
FIGURE 61: PARAMETRIC OUTPUT DATA OF GUIDE G25 FROM VISIBLE SEEDING. (A) PARAMETRIC OUTPUT SPECTRA FOR DIFFERENT SEED POWER LEVELS WITH THE SAME PUMP POWER INPUT (B) THEORY EXPECTATION (LINE) AND EXPERIMENTAL RESULTS (DOTS) OF INTENSITY OF PARAMETRIC OUTPUT VS. INPUT SEED POWER	98
FIGURE 62: PARAMETRIC GAINS VS. IR SEED (IDLER) WAVELENGTHS OF STIMULATED FOUR-WAVE PARAMETRIC AMPLIFICATION FROM Ta_2O_5 PENTOXIDE WAVEGUIDE G20. INSET: GUIDE LOSSES AT EXAMINED IR WAVELENGTHS	100
FIGURE 63: PARAMETRIC OUTPUT DATA FROM IR SEEDING. (A) PARAMETRIC OUTPUT SPECTRA FOR DIFFERENT PUMP POWER LEVELS WITH THE SAME SEED POWER INPUT (B) THEORY EXPECTATION (LINE) AND EXPERIMENTAL RESULTS (DOTS) OF INTENSITY OF PARAMETRIC OUTPUTS VS. INPUT PUMP POWERS (C) THEORY EXPECTATION (LINE) AND EXPERIMENTAL RESULTS (DOTS) OF PEAK PARAMETRIC OUTPUT WAVELENGTHS VS. INPUT SEED WAVELENGTHS. THE IMAGE ALSO SHOWS EXPECTED THG OUTPUTS (DOTTED LINE), AND THE SPECTRA PROFILES OF THE PARAMETRIC OUTPUTS FOR EACH SEED WAVELENGTH.....	102
FIGURE 64: FOUR-WAVE PARAMETRIC AMPLIFICATION GAIN MEASURED ON A 6.6 μm WIDE LOW LOSS ER DOPED TANTALUM PENTOXIDE RIDGE WAVEGUIDE (G18).....	104
FIGURE 65: ILLUSTRATIONS OF THE STIMULATED CO-LINEAR PARAMETRIC FOUR-WAVE AMPLIFICATION PROCESS IN PLANAR Ta_2O_5 WAVEGUIDES.....	105
FIGURE 66: TIME DEPENDENT SPECTRA OUTPUT PROFILES FROM TESTED WAVEGUIDES OF BOTH VISIBLE AND IR SEEDS WITH SEED PEAK CHANGES INDICATED BY CIRCLES (DIAMETERS RELATIVE TO INTENSITY) WITHIN AROUND +/- 100 FS. (A) GUIDE G14 SEEDED AT 577 NM, (B) GUIDE G21 SEEDED AT 577 NM, (C) GUIDE G25 SEEDED AT 577 NM, (D) GUIDE G20 SEEDED AT 1300 NM	108
FIGURE 67: DISPERSION MEASUREMENTS ON THE EXAMINED WAVEGUIDE (G20). (A) WAVEGUIDE DISPERSION WITHOUT PATH DISPERSION CORRECTIONS, (B) OPTICAL PATH DISPERSION, (C) PARAMETRIC OUTPUT MODE IMAGES FROM	

STIMULATED FOUR-WAVE AMPLIFICATION EFFECT, AND (D) DISPERSION MEASUREMENTS BY KERR GATE WITH THE RSoft SIMULATION RESULTS OF THE REFRACTIVE INDEX FOR 12 SUPPORTED MODES	110
FIGURE 68: TAPERED PLANAR WAVEGUIDE	113
FIGURE 69: PHOTONIC CRYSTAL SLAB WITH LINE DEFECT [66]	114
FIGURE 70: ILLUSTRATION OF THE GENERATION MECHANISM OF VECSEL LASERS [113]	117
FIGURE 71: CONCEPT DESIGN FOR ON-CHIP TUNABLE LASER USING PLANAR PHOTONIC CRYSTAL WAVEGUIDE TECHNIQUE	119
FIGURE 72: (A) PHOTONIC CRYSTAL SLAB WAVEGUIDE, AND (B) WAVEGUIDE DISPERSION PROPERTIES FOR 4 TE MODES	120
FIGURE 73: SETUP FOR EXAMINING DIRECTIONAL PHASE-MATCHING EFFECTS AND WAVELENGTH TUNING WITHIN THE CRYSTAL STRUCTURES BY ADJUSTING THE INCIDENCE BEAM DIRECTION	121
FIGURE 74: BAND DIAGRAM OF A RECTANGULAR PHOTONIC CRYSTAL LATTICE	121
FIGURE 75: SPECTROSCOPIC ANGULAR SURFACE REFLECTOMETRY BEAM COUPLING VIA LEAKY MODES TO INVESTIGATE PHASE-MATCHING IN PC.....	122
FIGURE 76: OUTPUT SPECTRA WITH PUMP WAVELENGTH RANGE OF 1000 – 1610 NM	134

List of Tables

TABLE 1: CALCULATED AVERAGE NONLINEAR COEFFICIENTS FOR EACH PUMP WAVELENGTH	69
TABLE 2: FITTING PARAMETERS OF OUTPUT SPECTRA AT PUMP WAVELENGTH OF ~1200NM	80
TABLE 3: FITTING PARAMETERS OF OUTPUT SPECTRA AT PUMP WAVELENGTH OF ~1600NM	85
TABLE 4: FITTING PARAMETERS FOR Ta_2O_5 AND TiO_2 MATERIAL DISPERSION [63]	128
TABLE 5: SELLMIEER COEFFICIENTS OF PURE AND DOPED SILICA GLASSES [15].....	129
TABLE 6: CAUCHY PARAMETERS FOR TeO_x [64]	130

Academic Thesis: Declaration Of Authorship

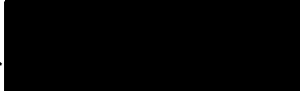
I,RUIQI CHEN..... [please print name]

declare that this thesis and the work presented in it are my own and has been generated by me as the result of my own original research.

[title of thesis] ...**Investigation of Nonlinear Processes and Device Designs Applicable to the Creation of a Compact, Broadly Tunable Laser Based on Tantalum Pentoxide Planar Lightwave Circuit Platform ...**

I confirm that:

1. This work was done wholly or mainly while in candidature for a research degree at this University;
2. Where any part of this thesis has previously been submitted for a degree or any other qualification at this University or any other institution, this has been clearly stated;
3. Where I have consulted the published work of others, this is always clearly attributed;
4. Where I have quoted from the work of others, the source is always given. With the exception of such quotations, this thesis is entirely my own work;
5. I have acknowledged all main sources of help;
6. Where the thesis is based on work done by myself jointly with others, I have made clear exactly what was done by others and what I have contributed myself;
7. Either none of this work has been published before submission, or parts of this work have been published as: [please list references below]:

Signed:.....

Date:20 December 2010.....

Acknowledgements

I'd like to thank Dr. Martin Charlton and Prof. Pavlos Lagoudakis for their wonderful supervision and always being there to help me on both experimental and theoretical difficulties. I also would like to thank every member of the Laboratories for Hybrid Optoelectronics group in School of Physics for their help and valuable suggestions on my experiments. I appreciate all the supports and encouragements I received from every friend I know. Finally, I would like to thank my wife and my family for their genuine love to me, and their unconditional supports to my study over the years.

Publications List

1. R. Y. Chen, M. D. B. Charlton, P. G. Lagoudakis, “Chi 3 dispersion in planar tantalum pentoxide waveguides in the telecommunications window,” *Optics Letters*, vol. 34, pp. 1135-1137, Apr 1 2009.
2. R. Y. Chen, M. D. B. Charlton, P. G. Lagoudakis, “Reference free Chi 3 dispersion measurements in planar tantalum pentoxide waveguides,” *Proceedings of the SPIE - The International Society for Optical Engineering*, vol. 7420, pp. 74200D (12 pp.)-74200D (12 pp.), 2009.
3. R. Y. Chen, M. D. B. Charlton, P. G. Lagoudakis, “Experimental Demonstration of On-Chip Optical Parametric Conversion in Planar Tantalum Pentoxide Waveguides”, *Proceedings of the SPIE - The International Society for Optical Engineering*, vol. 7781, pp. 778108 (5 pp.), 2010.
4. R. Y. Chen, M. D. B. Charlton, P. G. Lagoudakis, “On-Chip Ultrafast Optical Parametric Conversions in Planar Tantalum Pentoxide Waveguides”, to be published.

Abbreviations

AOM	Acousto-Optic Modulator
CW	Continuous-Wave
FDTD	Finite difference time domain
FEM	Finite Element Method
FOPA	Fibre-Optic Parametric Amplifier
FT	Fourier Transform
FWHM	Full Width at Half Maximum
FWM	Four-Wave Mixing
GVD	Group Velocity Dispersion
IC	Integrated Circuit
IR	Infrared
MCT	Mercury Cadmium Telluride
MI	Modulation Instability
NLSE	Nonlinear Schrödinger Equation
OCT	Optical Coherence Tomography
OPA	Optical Parametric Amplification/Amplifier
OPO	Optical Parametric Oscillation/Oscillator
OSA	Optical Spectrum Analyzer
PCF	Photonic Crystal Fibre
PLC	Planar Lightwave Circuit
SBS	Stimulated Brillouin Scattering
SC	Supercontinuum
SHG	Second-Harmonic Generation
SEM	Scanning Electron Microscope
SESAM	Semiconductor Saturable Absorber Mirror
SOP	State of Polarization
SPM	Self-Phase Modulation
SPR	Surface Plasmon Resonance
SRS	Stimulated Raman Scattering
THG	Third-Harmonic Generation

VECSEL	Vertical-External Cavity Surface-Emitting Lasers
WDM	Wavelength Division Multiplexing
XPM	Cross-Phase Modulation
ZDW	Zero-Dispersion Wavelength

Chapter 1 Introduction

The objective of this thesis was to investigate the viability of creating a widely tunable solid state waveguide laser in a compact planar lightwave circuit (PLC) form factor, capable of being pumped by a compact solid state light source. Conventional semiconductor lasers rely on electron transitions between well defined energy states to provide emission of light at specific wavelengths through electrical carrier injection to a junction region and radiative recombination of electron-hole pairs (excitons). The wavelength of solid state lasers is therefore highly dependent on the band gap energy of the semiconductor material from which the junction region is made. Some small level of colour variation can be achieved by inducing strain to modify the electronic band structure of a semiconductor material, but this approach leaves a wide range of wavelengths unobtainable by direct carrier injection alone, and excludes the possibility of wide wavelength tunability.

To access the wide range of intermediate wavelengths, nonlinear optical processes can be applied to the optical output of a solid state laser device to allow manipulation of emitted photon wavelengths (as opposed to manipulation of electron energies). In recent years, a range of mechanisms have been employed to reduce the footprint of bulk optics based high power laser systems. Some of the most successful approaches include the use of second harmonic generation, parametric wavelength conversions, and supercontinuum wavelength generation.

Commercially available widely tunable laser systems achieve wavelength conversion to frequencies which cannot be met by semiconductor band structure engineering alone, by utilizing a variety of nonlinear effects. Optical parametric oscillators (OPO) and optical parametric amplifiers (OPA) are the most successful widely tunable laser

systems available to date (see fig. 1), utilizing nonlinear conversions of a pump signal to other wavelengths through a combination of nonlinear mechanisms including: second harmonic generation ($\omega_{output} = 2\omega_{pump}$), supercontinuum generation, and parametric wavelength conversion ($\omega_{signal} = \omega_{pump} - \omega_{idler}$) in conjunction with selectable phase-matching. Currently available OPOs and OPAs are large, expensive, and sensitive pieces of equipment, requiring a high power, ultrafast pump source (typically 5–10 W pump). All of this keeps them confined to specialized optics labs and makes them unsuitable for real world mass market applications.



Figure 1: Example OPO/OPA systems from Newport Co. and Coherent Inc. [1, 2]

Broadband tunable laser systems, for example OPO/OPA, require precisely phase-matched condition for mixing of a pump beam, and a supercontinuum (SC) beam. Both the pump beam and the SC beam are obtained using nonlinear crystals, e.g. β -barium borate ($\beta - BaB_2O_4$ or BBO) crystal and sapphire plate, through harmonic generation and several nonlinear optical processes, respectively. Recent works in nonlinear planar waveguides show the possibility of making the optical parametric conversions on a single chip, i.e., on-chip tunable lasers.

Supercontinuum (SC) is a critical sub requirement for the realization of a broadband tunable laser. SC is a phenomenon where a pulse propagating through a nonlinear medium experiences extreme spectral broadening over a frequency range which can exceed 100 THz [3]. SC generation is a hot research topic in itself as it can be used for a large range of applications including: optical parametric amplifier/oscillator (OPA/OPO) [3, 4], absorption spectroscopy [5], dispersion measurement [6], frequency metrology [7], optical coherence tomography (OCT) [8], wavelength division multiplexing (WDM) source [6], sensor techniques [9], and biomedical applications [10]. The recent development of the microstructured fibres and the high

power femtosecond laser sources after year 2000 gives a rise to this field and a detailed physical understanding the SC generation is provided for the fibres [11]. Although the fibres are most commonly used in the optical research for optical communications, it is very interesting that the planar waveguides could provide better integration capability to the modern integrated circuit (IC) industry, where the smaller and cheaper optical chips could be fabricated and used for the replacements of bulky nonlinear crystals or optical fibres.

1.1 Project Aim

The overall aim of this project is to investigate the viability and to develop base technologies required to fabricate an on-chip broadband tunable laser, as the most significant advantage of planar waveguides is their capability of integration with other components to constitute a building block in integrated optical circuits [12, 13]. This involves producing supercontinuum, performing parametric wavelength conversion within a nonlinear phase-matching element, using a set of potentially different planar waveguide devices within the same chip, all of which must be powered by a compact low cost solid state laser source.

In contrast to photonic crystal fibres, planar waveguides require a core material with a large nonlinear coefficient to achieve the desired nonlinear effect within a short distance of propagation (typically 1 cm rather than 10s of cm for a fibre). Also the predominant contributory effects are not necessarily the same. Hence the nonlinearity of the waveguide devices is critical for the design. In depth study was performed in chapter 4 to investigate wavelength dependence of $\chi^{(3)}$, which is the dominating factor within the waveguide devices studied in this thesis. The other important property related to the design is linear dispersion of the waveguide devices. This includes material dispersion, and guide dispersion that changes with waveguide geometry. The dispersion results in group velocity dispersion (GVD) of the input beams within the waveguide devices. The waveguide dispersion, including GVD, could affect the whole design as it is affecting the phase-matching condition and the forming mechanisms of outputs from the waveguide. Software simulations are

performed in chapter 3 to accurately model the dispersion, and to provide geometry information for waveguide designs.

One of the most difficult and critical part of the design is to achieve SC using compact planar lightwave circuit (PLC) technology. Supercontinuum generation is a very complex process which can involve a wide range of nonlinear processes. Previously, researchers have demonstrated the generation of supercontinuum in planar waveguides [12], but have not investigated the fundamental physical processes in detail. This thesis therefore focuses initially on the investigation of physical processes involved in the generation of SC on planar waveguides for the purpose of chip design integration (chapter 5). Another goal of this project is therefore to design the planar waveguides to obtain a supercontinuum (SC) spectrally matched to the applications, with high coupling efficiency at interfaces between sub-components. This involves a detailed study of the mechanism of the formation of the SC in the current planar waveguides, and the issues of integration with the currently commonly used optical devices, particularly optical fibres.

Another important element of the design is to investigate the capability of performing parametric conversions within the waveguide devices. As reviewed in section 2.2.7, the parametric effect could be governed by the second order ($\chi^{(2)}$) or third order ($\chi^{(3)}$) nonlinear susceptibility where three- or four-photon process is involved. The parametric effect showed in the optical waveguide devices studied in this thesis could be categorized as a four-photon process, i.e. governed by $\chi^{(3)}$. The parametric conversion requires certain phase-matching condition between the pump and supercontinuum beams to provide amplifications to the desired output wavelength. The phase-matching condition are affected by both the input beams, and the waveguide geometry, where waveguide geometry changes the GVD of the waveguides. The parametric effect and phase-matching condition were then studied in chapter 6 to explore the possibilities of producing the on-chip tunable lasers.

1.2 Thesis Overview

This thesis starts with a review of linear and nonlinear effects related to the supercontinuum (SC) generation, and parametric conversions. Chapter 2 also reviews several examples of the SC, and parametric conversion results among the research works published to the state-of-art. Chapter 3 presents a theoretical investigation of dispersion properties of slab, rib, and ridge planar waveguides, including investigations of required numerical accuracy, and provides essential information for waveguide designs. Chapter 4 derives the third-order susceptibility and nonlinear coefficient of tantalum pentoxide (Ta_2O_5), which is the nonlinear waveguide material used for test sample, and the experimental demonstration of frequency tripling in the waveguides, i.e. third-harmonic generation (THG). Chapter 5 presents two examples of the current experimental results of SC on Ta_2O_5 planar waveguides in near infra-red wavelength range (990 – 1610 nm). To explore the possibility of making tunable lasers using planar Ta_2O_5 waveguides, chapter 6 demonstrated the experiment results from pump-probe experiment with measured dispersion properties of the waveguides. Based on the progress and the aim of the project, chapter 7 provides a plan for future theoretical and experimental work. The last chapter concludes this thesis with a brief outlook of the project.

Chapter 2 Literature Review

Both parametric wavelength conversion and supercontinuum (SC) generation devices are key sub-components for a broadband tunable laser. Parametric effects are one of the most important nonlinear effects associated with supercontinuum generation. Supercontinuum is created by inducing spectral broadening on an optical pulse from a pump laser. The spectral broadening process involves a combination of linear and nonlinear optical effects. The linear effect is often referred to as group velocity dispersion (GVD) and there are several nonlinear effects which act together with GVD during the time while the light pulse propagates in the waveguide. In the mean time, there are several other factors that will affect the generation mechanism, e.g. input pulse duration and the properties of the waveguide [11]. This chapter provides an overview of the key effects that relate to optical parametric oscillation and supercontinuum generation. A brief review of state of the art technologies for getting parametric effects and producing the SC is also given in this chapter.

2.1 Group Velocity Dispersion (GVD)

Dispersion in the waveguide, often referred to as chromatic dispersion, comprises the material dispersion and the waveguide dispersion. Material dispersion can be described as the refractive index variation of the waveguide material dependent upon the wavelength of the spectral components in the pulse and waveguide dispersion is induced by the confinement of the light within the waveguide structure [3, 14]. In reality, the pulse travelling in the waveguide has a temporal distribution, i.e. an envelope, which travels at the speed of v_g , the group velocity [3, 15]. The dispersion

of the group velocity (D), described by the second derivative of v_g , is defined as the group velocity dispersion as [3]:

$$D = -\frac{\lambda}{c} \frac{d^2 n}{d\lambda^2} \quad (1)$$

where λ is the wavelength, c is the speed of light in vacuum, and n is the refractive index of the material at λ .

In the case of $D = 0$, the wavelength corresponding to the zero dispersion is therefore called zero-dispersion wavelength (ZDW): $\lambda = \lambda_D$. When $D < 0$, i.e. $\lambda < \lambda_D$, the region is referred to as normal GVD regime. High frequency components of an optical pulse travel slower than the low frequency components of the same pulse. The opposite occurs in the so called anomalous GVD regime, where $D > 0$ and $\lambda > \lambda_D$ [3].

GVD alone can introduce the broadening of the pulse over a sufficient length of propagation (the dispersion length L_D) since the pulse can maintain its width only if all spectral components arrive together. If the propagation length L is also longer than the length over which nonlinear effects are significant (the nonlinear length L_{NL}), the nonlinear optical effects will act together with the dispersion leading to different behaviour than the GVD alone [3].

2.2 Nonlinear Optical Effects

All dielectric materials exhibit optical nonlinearities for very intense electro-magnetic fields. These originate from an induced anharmonic motion (polarization field) of bound electrons under the influence of the applied optical field [3]. This nonlinear optical phenomena is commonly described by expressing the induced polarization (P) in terms of the applied electric field strength (E). The time-varying polarization can induce electromagnetic charge acceleration, which in turn generates electromagnetic radiation (i.e. new components of the electromagnetic field) [4]. The total polarization induced by electric dipoles satisfies the following relation [3]:

$$P = \varepsilon_0 \cdot (\chi^{(1)} E + \chi^{(2)} EE + \chi^{(3)} EEE + \dots) \quad (2)$$

where ε_0 is the vacuum permittivity and $\chi^{(j)}$ ($j=1, 2, \dots$) is the j th order susceptibility. The linear susceptibility ($\chi^{(1)}$) has the most dominant effect on P , relating to dispersion and attenuation effects described in the above section. The second-order susceptibility ($\chi^{(2)}$) is responsible for nonlinear effects such as second-harmonic generation (SHG) and sum/difference-frequency generation, but only exists for materials with non-centrosymmetric crystal lattice. The third-order susceptibility ($\chi^{(3)}$) exists in all materials and is involved in most nonlinear interactions such as third-harmonic generation (THG), and four-wave mixing (FWM) [3, 4]. Therefore, for materials with centrosymmetric crystal lattice, $\chi^{(3)}$ dominates most of the nonlinear effects, and other higher order nonlinear coefficients can be negligible. Hence, the nonlinear polarization (P_{NL}) could be simplified to [3]:

$$P_{NL} = \varepsilon_0 \chi^{(3)} EEE \quad (3)$$

Some of the nonlinear optical effects associated with pulse broadening are responsible for the generation of extra frequency components in the SC leading to enhanced broadening. These effects are caused by the optical response (and temporary modification) of a nonlinear material under the application of a large optical field, and include Optical Kerr Effect, Self-Phase Modulation (SPM), Optical Solitons, Cross-Phase Modulation (XPM), Stimulated Raman Scattering (SRS), and Four-Wave Mixing (FWM). The next section explains each of these nonlinear optical effects in turn to provide an insight to expected nonlinear effects that can occur inside the waveguides.

2.2.1 Optical Kerr Effect

The optical Kerr effect is the phenomenon in which the refractive index of the medium changes when the electron orbit becomes deformed by the strong electric field [14]. This could be expressed as [14, 16]:

$$n(t) = n_0 + n_2 I(t) \quad (4)$$

where n_0 is the linear refractive index, I is the optical intensity, and n_2 the Kerr coefficient (or nonlinear refractive index). In solid semiconductors, n_2 is related to third-order susceptibility ($\chi^{(3)}$) by the following equation [17]:

$$n_2 = \frac{16\pi^2}{cn_0^2} |\chi^{(3)}| \quad (5)$$

where c is the speed of light in vacuum.

2.2.2 Self-Phase Modulation (SPM)

SPM is a phenomenon caused by the optical Kerr effect (which induces intensity dependent index change in the refractive index of a material) causing broadening of the pulse spectra. It is a pulse effect that leads to the preceding edge of the pulse being red-shifted and the trailing edge to be blue-shifted as shown in Figure 2(a) [14]. In the mean time, the angular frequency decreases at the preceding edge of the pulse and increases at the trailing edge, see Fig. 2(b) [14]. The above time-dependent change, or modulation of the phase, leads to spectral broadening/frequency chirping ($\delta\omega$) of the optical pulse [14, 16].

The time dependence of the frequency variation induced by SPM for an optical pulse is given by [4]:

$$\omega(t) = \omega_0 + \delta\omega(t) \quad (6)$$

where ω_0 is the frequency of the original pulse, $\delta\omega(t) = \frac{d}{dt}\phi_{NL}(t)$ is the changing term, therefore, maximum frequency change of the pulse with initial pulse width of τ_0 is: $\delta\omega_{\max} \approx \frac{\Delta\phi_{NL}^{(\max)}}{\tau_0}$. The phase change term $\phi_{NL}(t)$ is given by [4]:

$$\phi_{NL}(t) = -n_2 I(t) \frac{\omega_0}{c} L \quad (7)$$

where $I(t)$ is the intensity change with respect to time, and the maximum phase change of the pulse $\Delta\phi_{NL}^{(\max)} \approx n_2 I_0 \frac{\omega_0}{c} L$, where I_0 and L are the original pulse intensity and interaction length, respectively. Therefore, the maximum change in frequency caused by SPM for $n_2 > 0$ is:

$$\delta\omega_{\max} \approx n_2 I_0 \frac{\omega_0}{c} L \frac{1}{\tau_0} \quad (8)$$

The spectral broadening effect on the optical pulse makes SPM one of the dominant effects responsible for generating the SC.

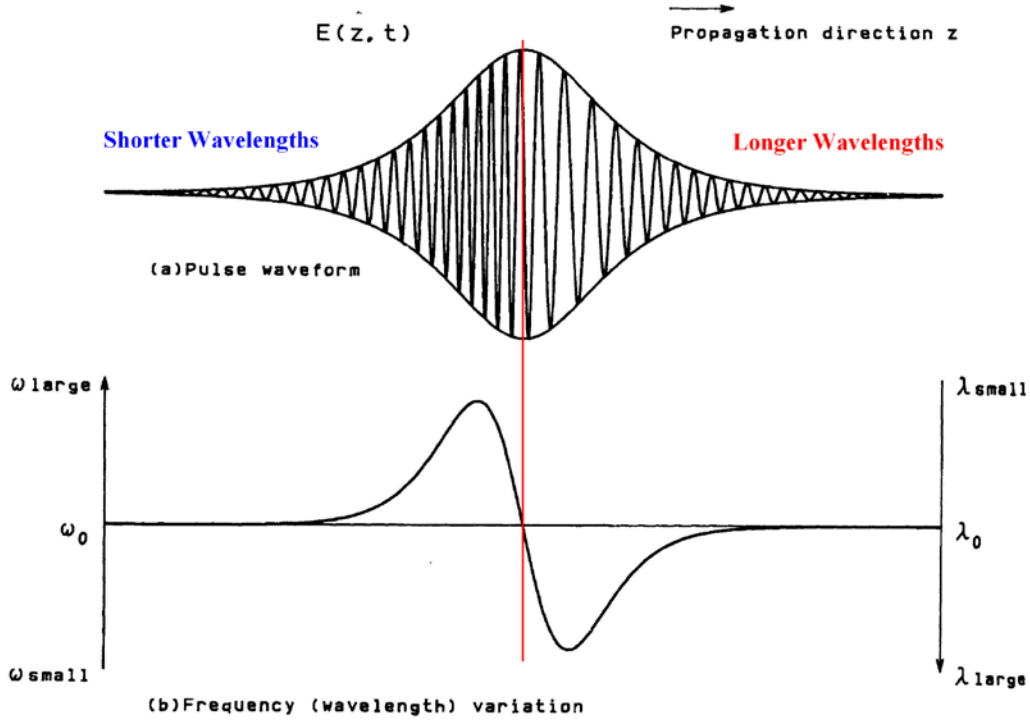


Figure 2: Self-phase modulation of optical pulse: (a) pulse waveform and (b) instantaneous angular frequency/wavelength change [14]

The SPM induced nonlinear spectral broadening can either be magnified or compensated by the GVD effect [16]. In the normal dispersion regime, the nonlinear dispersion is magnified by the GVD, which can result in enhanced broadening. The energy of the optical pulse is dispersed into the preceding and trailing edges and the pulse temporal shape becomes square. The latter effect of the pulse can be used for pulse compression when the pulse is passed through an anomalous medium like a grating pair [14, 16]. In the anomalous dispersion regime, the nonlinear dispersion is compensated by the GVD, since the GVD now has a compression effect on the optical pulse, which can lead to optical soliton formation if the compression balances the SPM broadening. If the system exhibits an instability that modulates the steady state of the soliton, the combined effect of SPM and GVD becomes a nonlinear

phenomenon called modulation instability (MI) [3, 16]. Both optical soliton and MI effects are described in the following section.

2.2.3 Optical Solitons

An optical soliton is a special kind of wave packet that can propagate undistorted over long distances [3]. Solitons occur when the nonlinear dispersion is exactly compensated by the GVD across the entire pulse [16], see Fig. 3 [3].

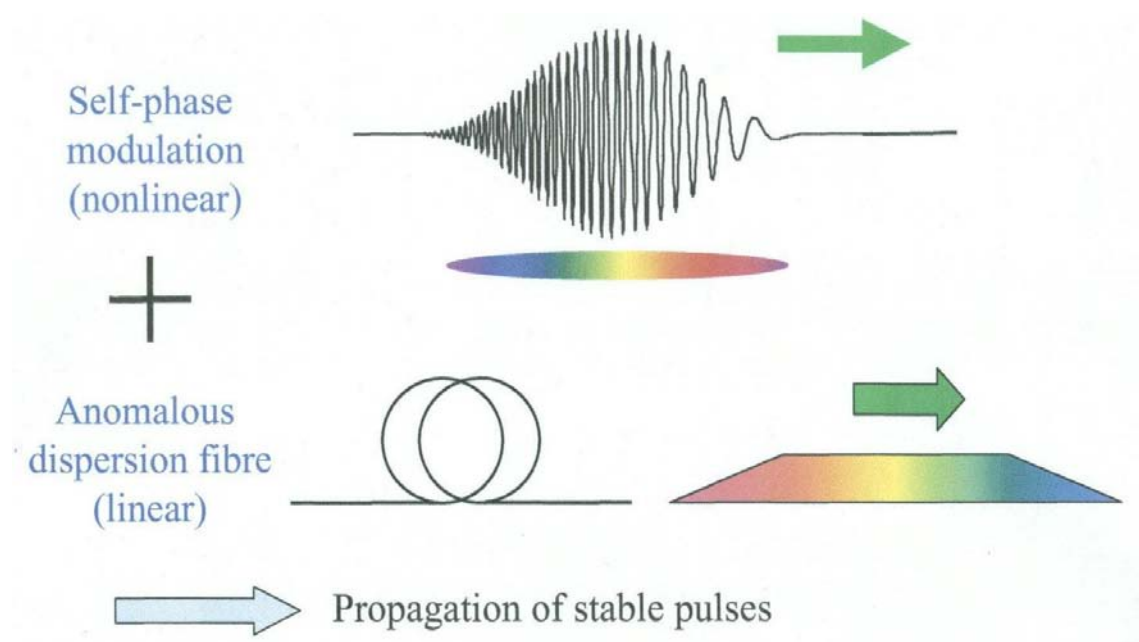


Figure 3: Illustration of optical solitons effect in fibre [3]

The simplest soliton is the fundamental soliton with the soliton order $N = 1$, where the pulse shape does not change on propagation. Higher-order solitons are also possible providing the peak power is N^2 times that required for the fundamental soliton, where higher-order solitons periodically change their temporal pulse shape (see Fig. 4 [14]) [3, 14]. Although solitons are not directly related to SC generation, the combination of solitons and other effects creates a lot of interesting phenomena that give rise to the spectral broadening and so are mentioned here.

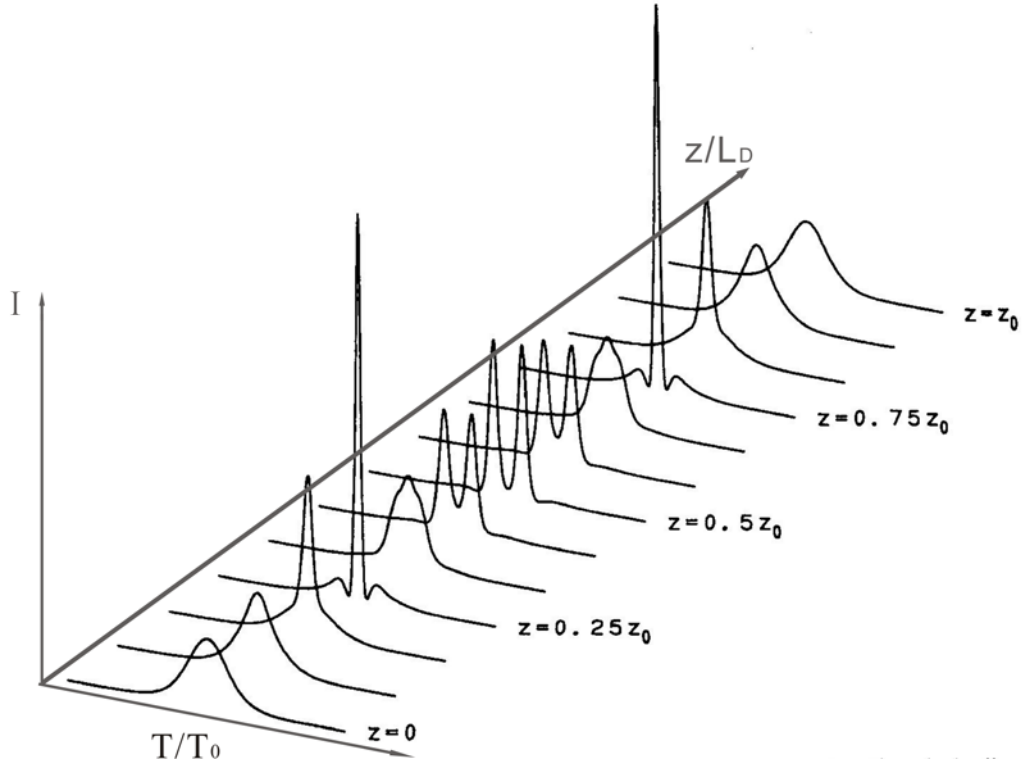


Figure 4: Temporal pulse shape variation of the third-order optical soliton [14]

2.2.3.1 Modulation Instability (MI)

Many nonlinear systems exhibit an instability that leads to modulation of the steady state as a result of interplay between nonlinear and dispersive effects. This phenomenon is referred to as the modulation instability (MI) in which the side-band component of the amplitude-modulated light grows exponentially under certain conditions [3, 14]. Figure 5 [14] shows the growth of side-band components by the MI in optical fibre with input power: (a) low, (b) 5.5 W, (c) 6.1 W, and (d) 7.1 W.

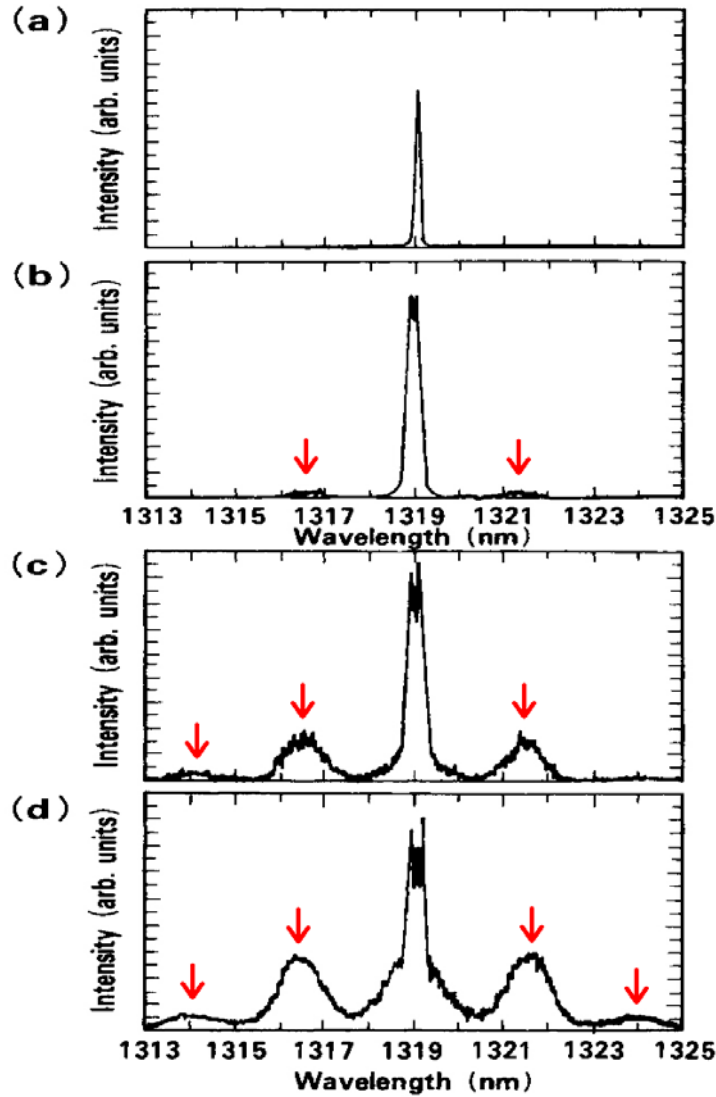


Figure 5: Growth of side-band components (indicated by red arrows) by the modulation instability in optical fibre with input power: (a) low, (b) 5.5 W, (c) 6.1 W, and (d) 7.1 W [14]

2.2.3.2 Higher-Order Effects

Higher-order effects such as higher-order dispersion, self-steepening, and intrapulse Raman scattering can introduce perturbations to solitons causing interesting effects like auto-solitons, soliton fission, and soliton self-frequency shift [3]. These parasitic effects all involve spectral broadening or generation of new frequency components, some of which have been shown to be the dominant effect responsible for SC generation [3, 9, 11, 16].

2.2.4 Stimulated Raman Scattering (SRS)

SRS was first observed in 1962 and is caused by the interaction between pump light photon and a solid, which is excited and releases a low-frequency photon by making transitions to a vibrational state. In SRS, both forward and backward scattered waves are generated and most of the pump energy is transferred to the so-called Stokes wave [3]. When there is no seed for the Stokes light for SRS, i.e. $I_s(0) = 0$ at $z = 0$, SRS can build up from spontaneous Raman scattering, which requires Stokes power equal

to the pump power to be at least $P_c = \frac{16A_{eff}}{g_R \cdot L_{eff}}$ [14]. Therefore, SRS in silica fibres

requires much high powers, typically > 1 W, and the Raman shift is around 13.2THz for silica fibre [3, 14, 16]. The generated Stokes light intensity along the propagation direction ($I_s(L)$) could be obtained by [14]:

$$I_s(L) = I_s(0) \cdot \exp(g_R \cdot I_0 \cdot L_{eff} - \alpha_s L) \quad (9)$$

where $L_{eff} = [1 - \exp(-\alpha_p L)] / \alpha_p$ is the effective length, I_0 is the pump intensity, g_R is the Raman gain coefficient, α_p and α_s are losses of pump and Stokes light, respectively. From equation 9 above, g_R is the most important quantity for describing SRS [3]. Figure 6 [14] below shows the Raman gain coefficient of the first Stokes light when pumped at $\lambda = 1\mu m$.

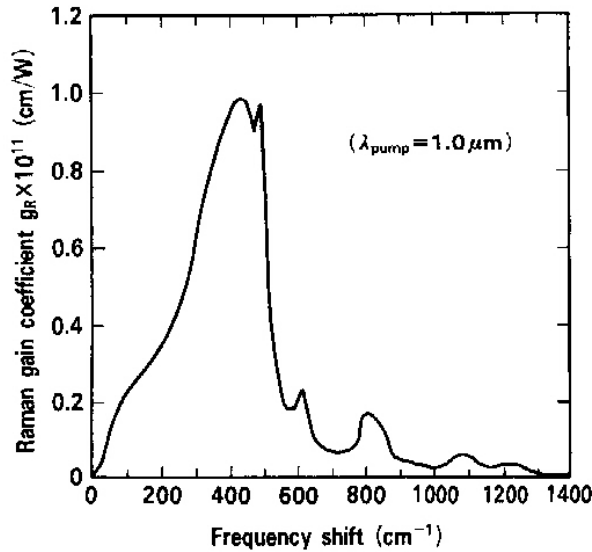


Figure 6: Raman gain spectrum of silica glass [14]

SRS is particularly important for SC since it is affected by the four-wave mixing process in any medium [3]. Therefore, SRS and parametric FWM between a pump and a Stokes wave can generate the anti-Stokes wave or, equivalently, two pump photons can simultaneously generate a Stokes and an anti-Stokes photon. This SRS-FWM process with high power picosecond pulses could be a dominant process for the generation of SC [16].

If the wavelengths of the pump and Raman pulses lie in the anomalous GVD regime, the Raman pulse could propagate as a soliton under certain condition. This is referred to as a Raman soliton [3]. Another higher-order effect related to Raman scattering is intrapulse Raman scattering, which is a phenomenon that can occur even before the threshold of noise-induced SRS is reached. When combined with the higher-order solitons, intrapulse Raman scattering could introduce the soliton self-frequency shift as stated in 2.2.4.2 [3].

2.2.5 Cross-Phase Modulation (XPM)

XPM is similar to SPM as both of the effects are caused by the Kerr effect [3]. The difference is XPM involves two optical beams with different wavelengths propagating inside the waveguide and SPM assumes only one inside the waveguide [16]. In XPM, the intensity modulation of one of the beams results in a phase modulation of the other, therefore, the XPM induced spectral broadening could be twice as large as in SPM. In practice, XPM always accompanies SPM when two or more optical fields are launched simultaneously into the waveguide [3, 16]. Since nonlinear effects such as stimulated Raman scattering and four-wave mixing are capable to generate waves at new wavelengths, XPM can either induce energy transfer between two waves or couple the two optical field without inducing any energy transfer between them [3].

By separating the rapidly varying part of the electric field and substituting it into equation 3, four terms depending on E_1 and E_2 are obtained [3]:

$$P_{NL}(\omega_1) = \chi_{eff} (|E_1|^2 + 2|E_2|^2) \cdot E_1 \quad (10)$$

$$P_{NL}(\omega_2) = \chi_{eff} (|E_2|^2 + 2|E_1|^2) \cdot E_2 \quad (11)$$

$$P_{NL}(2\omega_1 - \omega_2) = \chi_{eff} \cdot E_1^2 \cdot E_2^* \quad (12)$$

$$P_{NL}(2\omega_2 - \omega_1) = \chi_{eff} \cdot E_2^2 \cdot E_1^* \quad (13)$$

where χ_{eff} is the effective nonlinear parameter related to $\chi^{(3)}$. The new frequencies introduced in equations 12 and 13 originate from four-wave mixing effect discussed in the next section (i.e. section 2.2.6).

XPM can also result in several XPM-induced coupling effects such as a multi-peak temporal structure of the pulses, polarization-dependent spectral broadening, pulse trapping, and optical wave breaking [3, 16]. Experiments undertaken in chapter 5 show that XPM is a key process involved in SC generation in our waveguides.

2.2.6 Four-Wave Mixing (FWM)

FWM is one of the important nonlinear effects that contribute to the generation of SC. FWM is a nonlinear response of bound electrons of a material to an electromagnetic field, i.e. an optical field in context of nonlinear optics. FWM is a third-order parametric process which involves the nonlinear interaction among four optical waves [3]. The efficiency of this third-order nonlinear process strongly depends on the phase-matching condition [3, 14, 18]. In quantum-mechanical terms, FWM occurs when photons from one or more waves are annihilated and new photons are created during parametric wavelength conversion: $\omega_1 + \omega_2 \rightarrow \omega_3 + \omega_4$ [3, 18]. The intensity of the new component (I_4) is determined by the intensities of the other three (I_1 to I_3) through the general equation [18]:

$$I_4 = const \cdot |\chi^{(3)}|^2 \cdot I_1 \cdot I_2 \cdot I_3 \cdot l^2 \cdot \left[\frac{\sin(\Delta k \cdot l/2)}{\Delta k \cdot l/2} \right]^2 \quad (14)$$

where $\Delta k = |k_1 + k_2 - k_3 - k_4|$ is the phase-mismatch, and l is the effective propagation length.

In the above case, two photons with frequencies of ω_1 and ω_2 are annihilated, while two photons at frequencies ω_3 and ω_4 are created simultaneously such that $\omega_3 + \omega_4 = \omega_1 + \omega_2$. In general, $\omega_1 \neq \omega_2$, and two generated frequency components lie symmetrically at the side of a central pump frequency of $\frac{\omega_1 + \omega_2}{2}$. This is called non-degenerate FWM [14]. In the special case called degenerate FWM, where $\omega_1 = \omega_2$, a strong pump wave at ω_1 creates two sidebands located symmetrically at frequencies ω_3 and ω_4 [3]. Figure 7 [14] shows the frequency arrangement of (a) non-degenerate FWM, and (b) degenerate FWM, so called stimulated optical parametric amplification, in the zero-dispersion region.

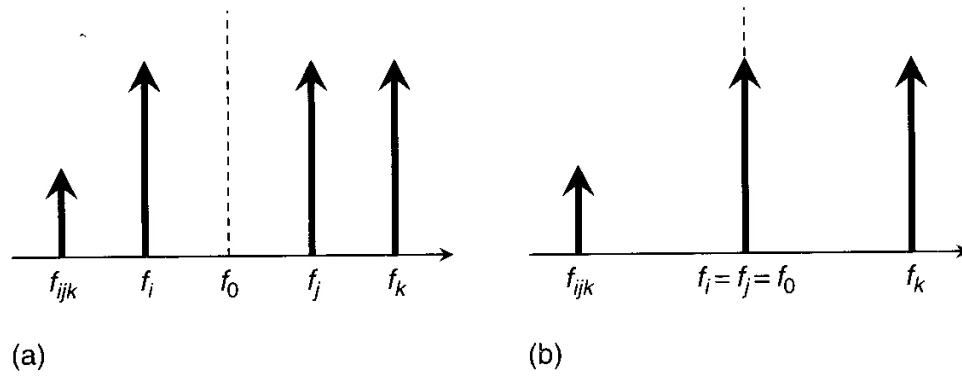


Figure 7: Frequency arrangement of FWM satisfying the phase-matching condition in zero-dispersion region: (a) non-degenerate case and (b) degenerate case [14]

Another factor that affects the FWM process is the high polarization-dependence since conservation of angular momentum is required among the four interacting photons. The efficiency of the newly generated waves in the process depends on the frequency separation, dispersion, and length of the waveguide [14]. Figure 8 [14] demonstrates the generated wave efficiency as a function of channel spacing in FWM.

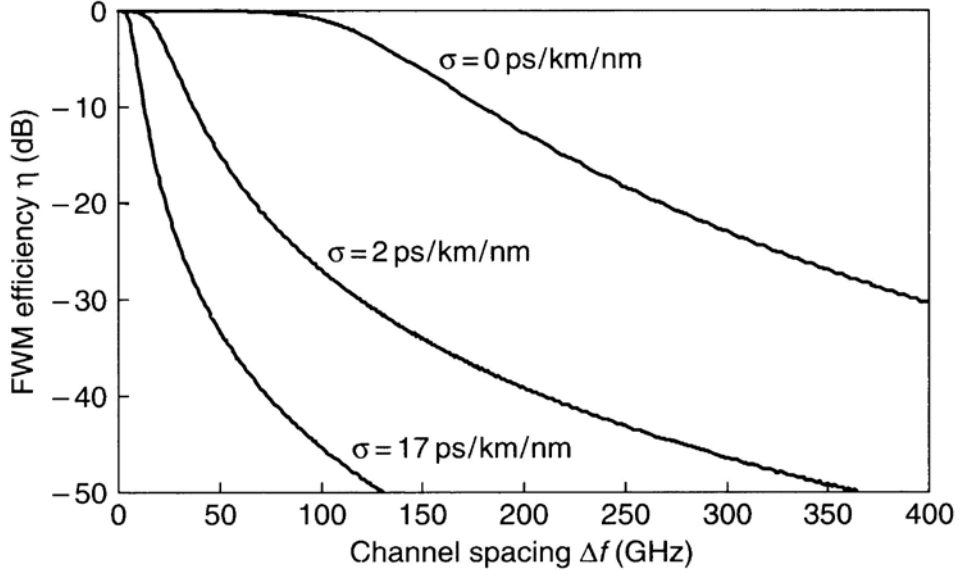


Figure 8: Generated wave efficiency as a function of channel spacing [14]

It is shown that FWM efficiency is quite high for fibre at zero-chromatic dispersion ($\sigma = 0$) when channel spacing ($\Delta f = f_k - f_i$ for degenerate FWM shown in figure 7b) is less than 100 GHz and will dramatically decrease as the $|\sigma|$ increases. The chromatic dispersion will be small enough if single mode fibre is considered. The reason for requiring a small dispersion is because the beam bandwidth (B) is inversely proportional to $\sqrt{\sigma}$ [14].

2.2.6.1 Third Harmonic Generation (THG)

One special case of the four-photon parametric interaction results in three photons transferring their energy to a single photon at frequency $\omega_4 - \omega_1 = \omega_2 + \omega_3$, and if $\omega_1 = \omega_2 = \omega_3$, this term is referred to as third harmonic generation (THG) [3, 18]. For THG, the phase-mismatch becomes $\Delta k = k_4 - 3k_1$ and equation 14 becomes [18]:

$$I_4 = const \cdot |\chi^{(3)}|^2 \cdot I_1^3 \cdot l^2 \cdot \left[\frac{\sin(\Delta k \cdot l/2)}{\Delta k \cdot l/2} \right]^2 \quad (15)$$

The experimental results of THG effects in planar waveguide samples are presented in detail in chapter 4.

2.2.7 Stimulated Optical Parametric Amplification

Stimulated optical parametric amplification (OPA) effect is one of the key effects used for tunable laser systems, such as optical parametric amplifier (OPA). The optical parametric amplifier could act as a versatile tunable source capable of producing beams in the infra-red (IR), visible, and ultraviolet spectral regions with either continuous-wave or pulse durations of nanoseconds, picoseconds, or femtoseconds [4]. Stimulated parametric amplification could be categorized as either a $\chi^{(2)}$ or $\chi^{(3)}$ governed effect, where three or four-photon interactions are involved, respectively. The parametric amplification generated from bulk crystals is based on a $\chi^{(2)}$ effect, and is the basis of operation for commercial OPA systems manufactured by Newport Co. and Coherent Inc., see fig. 1 in Chapter 1 [1, 2, 4, 19]. These laser systems provide very high quality tunable output with high power level, making them the industry standard pump source for nonlinear experiments.

When four-photon process are involved, the optical parametric amplification effect is categorized as a $\chi^{(3)}$ process, and is often referred to as degenerate four-wave mixing [3, 14]. Photonic crystal fibres and nonlinear waveguides made by different materials (including the planar waveguides used in this thesis), are used for $\chi^{(3)}$ type parametric amplification where the intensities follow the relationship [18]:

$$I_{output} = const \cdot |\chi^{(3)}|^2 \cdot I_{pump}^2 \cdot I_{seed} \cdot l^2 \cdot \left[\frac{\sin(\Delta k \cdot l / 2)}{\Delta k \cdot l / 2} \right]^2 \quad (16)$$

More detailed discussions of the above equation are given in chapter 6 where parametric outputs from waveguides are discussed in detail.

2.2.7.1 Review of Current Works

OPA governed by $\chi^{(2)}$ effects have been well established and commercialized as laser sources that provide tunable output with similar power across the wavelength range. For example, the optical parametric amplifier, OPA9400, manufactured by Coherent Inc., pumped by a 800 nm mode-locked femtosecond laser, could provides visible outputs between 500 – 700 nm and IR outputs from 900 – 2400 nm [1]. This

device has been used as source/pump for the THG, continuum generation, and pump-probe experiments in the following 3 chapters, respectively.

OPA examples governed by $\chi^{(3)}$ are normally achieved by using either photonic crystal fibre (PCFs) based on SiO_2 or planar waveguides. Experimental results from PCFs have been shown by Sharping *et al.* [20] and Sloanes *et al.* [21]. Both experiments demonstrate the OPA effect from a single seed wavelength. Silicon oxide PCF nanowires demonstrated spectral widening compatible with the parametric effect [21], but suffer from problems of low damage threshold and difficulty of chip level integration which prevent the PCF from replacing the bulky systems used nowadays. The $\chi^{(3)}$ OPA has also been demonstrated in planar waveguides with core materials of $LiNbO_3$ [22], silicon (Si) [23, 24], and chalcogenide (As_2S_3) [25-30] glasses. The damage threshold issues also apply to silicon and chalcogenide nanowire waveguides made from the above materials, this limits use of parametric effects to telecommunications applications, which do not require high powers to operate.

All the above examples operate at telecommunications wavelengths and have a very limited tuning range of less than 100 nm, (this is much narrower than the results obtained in this study presented in chapter 6). The damage threshold for the core materials of most of the examples above is also quite low compared to Ta_2O_5 , which is capable of withstanding peak power densities of $2.5 \times 10^7 \text{ GW} / \text{m}^2$, (these figures have been validated by SEM images of waveguide facets after the experiments). The majority of $\chi^{(3)}$ type parametric oscillators based on fibres and waveguides are also seeded and pumped close to the telecommunication wavelength and no inverse operation that leads to visible beams has ever been shown before.

2.3 Supercontinuum (SC) Generation

The phenomena of the SC generation were discussed in detail in the introduction to this thesis. This section briefly discusses the specific dominating nonlinear effect(s) that are responsible for creating SC under conditions relevant to our waveguides. Currently, SC is produced by propagation of various types of pulsed laser sources

through the waveguides. One way of summarizing these works is to categorize the pump laser source by their pulse width: picosecond pulses, continuous-wave (CW), and femtosecond pulses [3]. Nonlinear effects contributing to SC generation are dependent upon the pump pulse width and so are now considered separately.

2.3.1 Pumping with Picosecond Pulses or CW Pulses

For the case of picosecond pump pulses, SPM, SRS, and FWM along with dispersion effects in the waveguide are the key nonlinear processes which govern the mechanism of SC generation, except that CW pumping requires a much higher power source [3, 11, 16]. SPM can induce spectral broadening of the pulse, but SPM alone cannot produce a supercontinuum extending over 100 nm or more [3]. As soon as SPM broadens the pump by 5 nm or more SRS can amplify the pulse spectrum on the long-wavelength side of the pump, but it can only enhance the supercontinuum selectively on the long-wavelength side, i.e. no short-wavelength components are generated by SRS, and thus SRS alone creates an asymmetric spectrum [3, 11]. The short-wavelength components are produced by the FWM providing the phase matching condition are met. The output also depends on the pump wavelength with respect to the ZDW governed by the GVD [3, 16]. The wavelength-dependence of the mechanism is illustrated in Figure 9 [11]:

- For a pump wavelength far from the ZDW in the normal GVD regime:
FWM effect is not significant. Hence, in this case the supercontinuum is generated by SRS and then broadened by the combined effects of SPM and XPM [11] (see the first two graphs in Fig. 9 [11]).
- For a pump wavelength near to the ZDW in the normal GVD regime:
The new frequency components are first introduced by the higher-order dispersion phase-matched FWM before SRS can occur. After that, the spectrum is broadened by Raman and XPM effects close to the pump wavelength and the side band component induced by FWM in the anomalous GVD regime is broadened by the soliton-fission-like dynamics [11] (as shown in the third graph in Fig. 9 [11]).

- For a pump wavelength at the ZDW or in the anomalous GVD regime:
The mechanism is as describe above, where all of the effects act together to produce a relatively uniform SC, as shown in the 780 nm and 800 nm pump cases in Fig. 9 [11]. However, as the bottom graph of Fig. 9 shows, pumping further in the anomalous GVD regime results in disappearance of the spectrum in the normal GVD regime since the initial spectral broadening does not generate sufficient bandwidth [11].

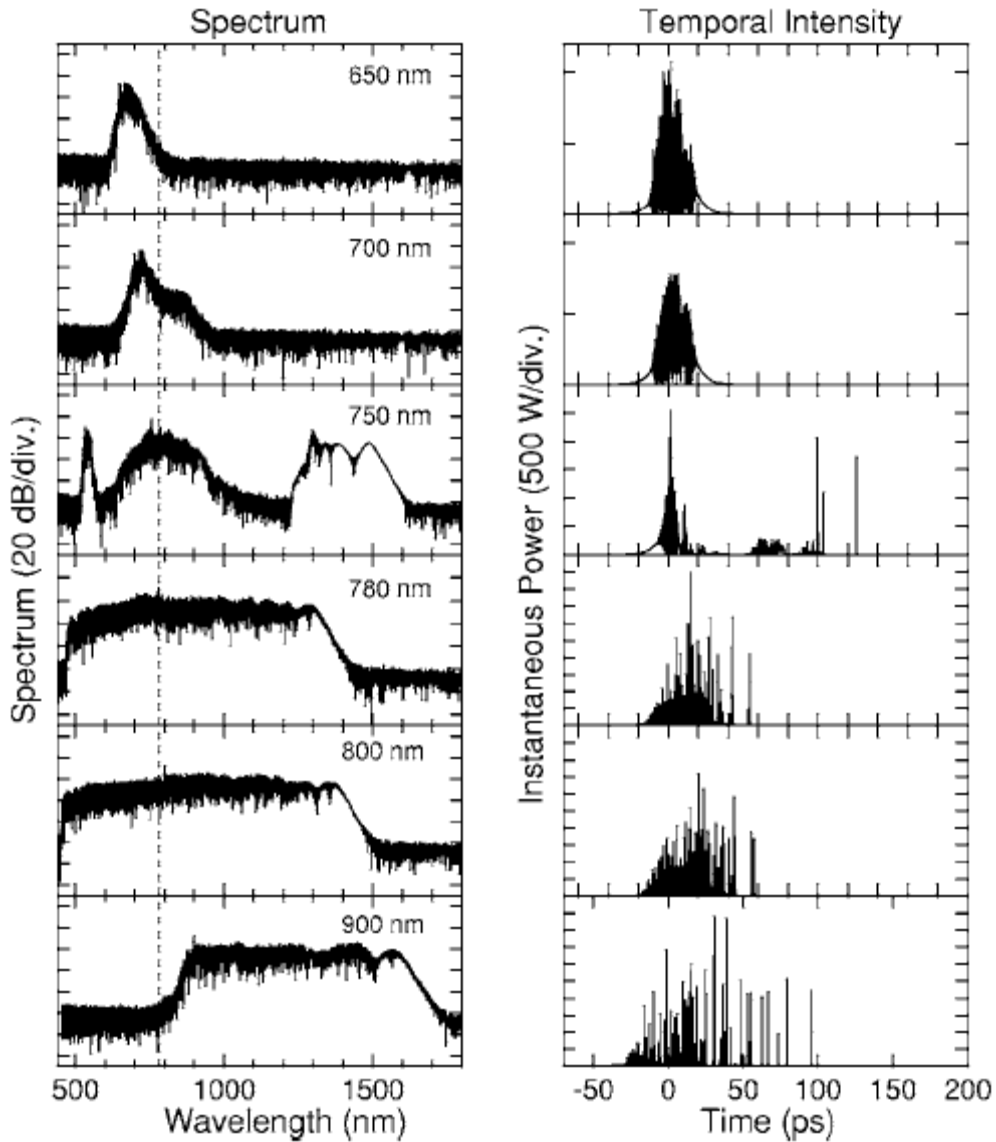


Figure 9: Simulation results of the spectral and temporal characteristics of the SC generated by selected pump wavelengths in a 2 m long PCF with 500 W – 20 ps input (dashed line indicates the zero-dispersion wavelength) [11]

2.3.2 Pumping with Femtosecond Pulses

For femtosecond pumping in the anomalous GVD regime, experiments on photonic crystal fibres (PCFs) show that the spectral broadening process is provided by the Raman effect, and the soliton fission which occurs within the first 1 cm of propagation [3, 11]. The weighting on spectral broadening caused by these two effects depends on the input pulse width of the pump. For input pulse duration larger than 200 fs, the Raman effect is dominant in the initial propagation stage; for pulse duration less than 20 fs, soliton fission is the primary effect to induce the spectral broadening. For the duration of the pulses in between, both effects contribute to the broadening with comparable weighting [11]. After 1 cm of propagation and initial spectral broadening, further propagation distance is associated with continuous red-shift of the long-wavelength but without further extension of the short-wavelength edge [11]. In case of the wavelength-dependence of the SC generated by the femtosecond pulses, ZDW is also the boundary line similar to the picosecond pulses [11]:

- For a pump wavelength far from ZDW in the normal GVD regime:
SPM is the dominant nonlinear process responsible for the spectral broadening to create SC [11] (see the first two graphs in Fig. 10) [11].
- For a pump wavelength close to the ZDW in the normal GVD regime:
Initial broadening is induced by SPM, and the generated frequency components in the anomalous GVD regime then follow the mechanism of broadening process as explained above [11] (see 700 nm case in Fig. 10) [11].
- For a pump wavelength at the ZDW or in the anomalous GVD regime:
The energy transfer mechanism is as explained above, in which case the Raman effects and the soliton fission are dominant. The results of pumping at this regime is demonstrated by the bottom three graphs in Figure 10 [11].

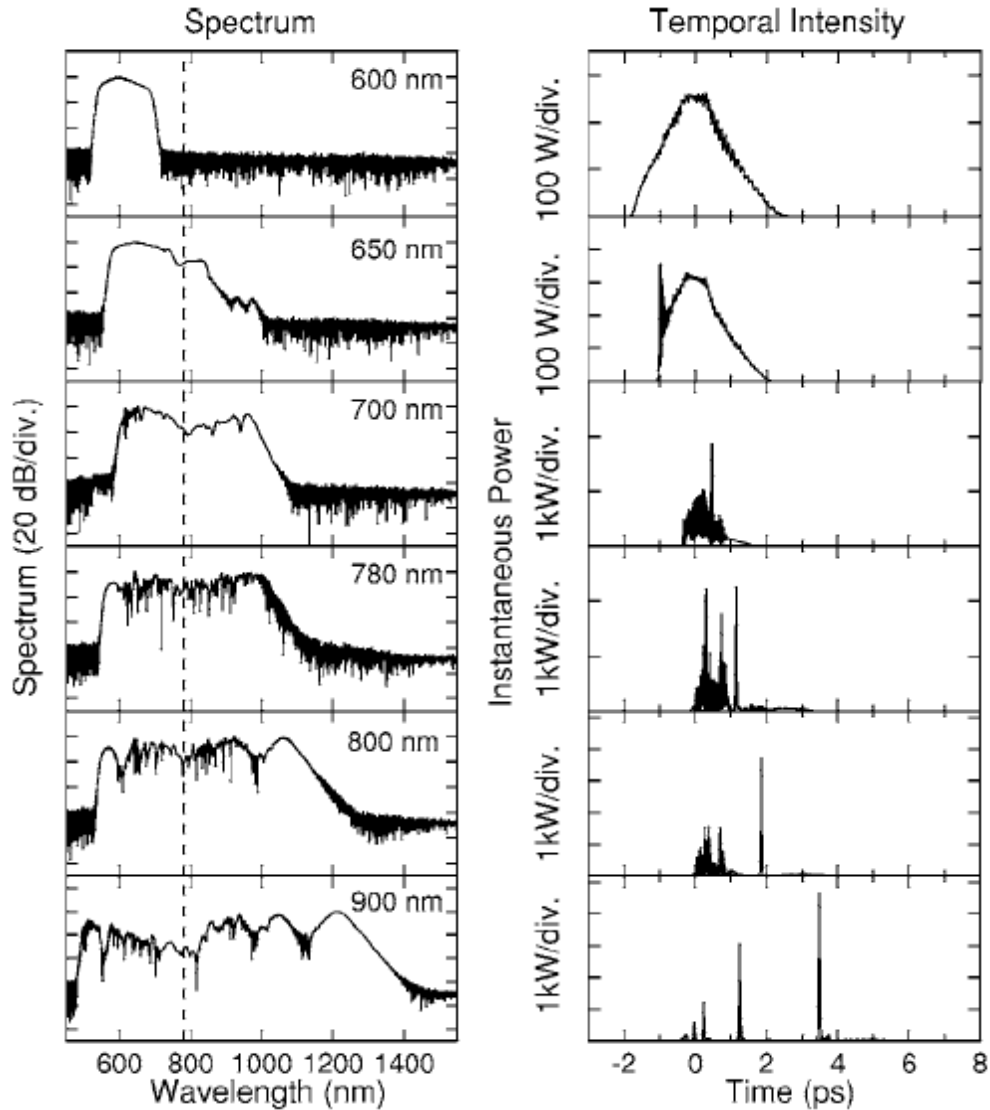


Figure 10: Simulation results of the spectral and temporal characteristics of the SC generated by selected pump wavelengths in a 2 m long PCF with 10 kW – 50 fs input (dashed line indicates the zero-dispersion wavelength) [11]

2.3.3 Other Issues Related to Supercontinuum

The process of SC formation includes pulse broadening as well as splitting. XPM could be introduced to create additional spectral components as two of the generated pulses overlap temporally and interact as they co-propagate some further distance. Thus, XPM is quite important for SC in highly nonlinear waveguides [3]. Since most of the nonlinear effects are directly dependent on the polarization state, the resulting SC also depend on the orientation of the input polarization, i.e. state of polarization

(SOP) [3, 11]. Another issue along with the SC is its coherence property which is affected by the fluctuations in the energy, width, arrival time of individual input pulses, and the input noises [3, 11].

2.3.4 Supercontinuum (SC) Generation Applications

This section briefly explains some of the key applications of SC generation such as: optical parametric amplifier (OPA), frequency metrology, optical coherence tomography (OCT), pulse compression, and wavelength division multiplexing (WDM).

2.3.4.1 Optical Parametric Oscillator/Amplifier (OPO/OPA)

OPO/OPA is a laser light source that emits light of adjustable wavelengths through an optical parametric amplification process [31]. OPA is a versatile source of frequency-tunable radiation throughout the infra-red, visible, and ultraviolet spectral regions. OPO/OPA could have continuous-wave, or pulse duration of nanoseconds, picoseconds, or femtoseconds depending on the pump source [4]. In order to achieve tunability in an OPA, it is necessary that one of the frequencies is adjustable, or alternatively has wide bandwidth. A supercontinuum (SC) source can therefore provide the necessary bandwidth, has a flat spectrum, and amplitude could be similar to the level of the other mixing component (usually a shorter wavelength output by harmonic generations).

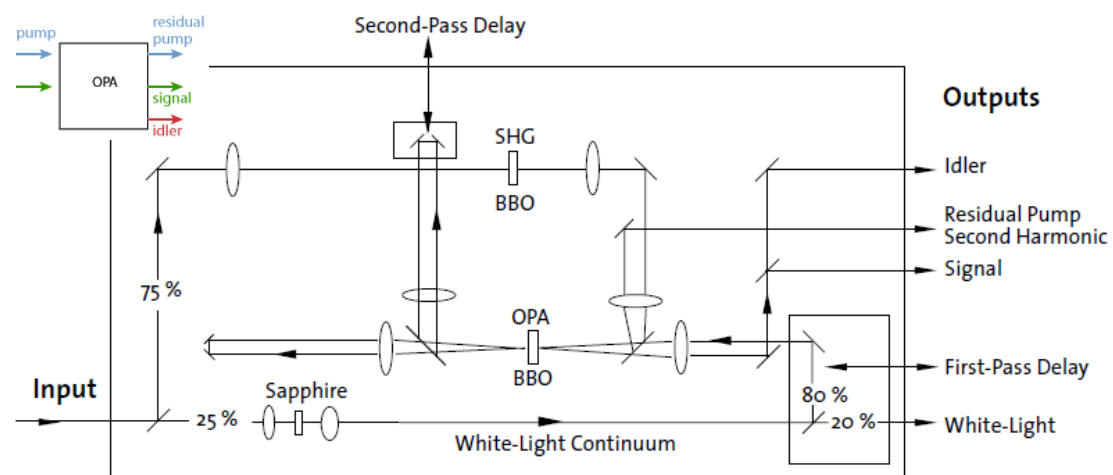


Figure 11: Optical path of an OPA9400 (Inset: the schematic illustration of an OPA9400) [1]

Figure 11 illustrates the internal optical path of a commercially available OPA system produced by Coherent Inc. [1] In this case SHG and continuum generation are generated from the same pump source. Alternatively they could be introduced separately by two different pump lasers. As the parametric processes are extremely sensitive to phase-matching condition, two pass delays are used to provide the phase-matching condition for parametric wavelength conversion. The results of the wave-mixing (either from sum/difference frequency generation govern by $\chi^{(2)}$ or non-degenerate four-wave mixing govern by $\chi^{(3)}$) give one beam and one idler output [31, 32]. The OPA system used for experiments in chapter 4, chapter 5, and chapter 6 gives two outputs at wavelength range of visible (480 – 700 nm) and infra-red (933 – 2300 nm), respectively. The fibre-based OPA is known as fibre-optic parametric amplifier (FOPA), where optical fibres are only used to provide the medium for wave-mixing [3], i.e. similar function as the OPA BBO in figure 11. One of the difficulties of using all-fibre configuration for an OPA is the control of propagation length to achieve the phase-matching condition, i.e. two pump beams have to arrive at the same time for wave-mixing process. With careful layout design, the SC and harmonic generation can be arranged in a planar arrangement to ensure that the two beams can meet the phase-matching condition, which means an on-chip tunable laser source is achievable from planar waveguides in a similar manner to the fibre devices (this is a key advantage of the approach adopted in this work).

2.3.4.2 Optical Coherence Tomography (OCT)

OCT is an imaging technology that allows *in-vivo* and *in-situ* cross-sectional morphological imaging of transparent and non-transparent biological tissue on a micrometer scale [8]. Therefore, OCT has many applications in the biomedical field, which include: ophthalmology (e.g. retina OCT/imaging at wavelengths around 840 nm), cardiovascular imaging, gastroenterology, and dermatology. The high speed capturing advantage of OCT makes the OCT based systems capable of providing 3D information based on sets of 2D scans at different depths using either B-scan or OCT for detecting early stage eye diseases. In the case of atherosclerotic lesions, the quality of OCT images have proved that it can match the gold standard for intracoronary imaging (intravascular ultrasound). The penetration depth for skin examination using OCT could reach up to ~2 mm, which is much more than ~0.25 mm using standard

confocal microscopy [33]. Because the longitudinal image resolution (Δz) is inversely proportional to the bandwidth ($\Delta\lambda$), and proportional to the square of the centre wavelength (λ_0), where $\Delta z = \frac{2\ln(2)}{\pi} \frac{\lambda_0^2}{\Delta\lambda}$, OCT typically operates at low resolution [6, 8]. Since the peaks and dips could result in artefacts in the OCT measurements, the SC source spectrum needs to be as smooth as possible. The flatness of the generated SC is one of the remaining challenges to the current devices, thus, a careful selection/design of the device is critical for OCT systems [6, 11]. Photonic crystal fibres (PCFs) currently used as SC sources for OCT struggle to achieve suitably flat spectral response since the SC generation processes rely on effects including SPM, XPM, SRS, and FWM and also input power density. One objective of this project is to investigate the creation of planar sources with improved spectral noise.

2.3.4.3 Frequency Metrology

Most spectroscopic experiments nowadays rely on the measurement of optical wavelengths rather than frequencies. Frequency metrology applies a Fourier transform (FT) to modes of a mode-locked femtosecond laser to produce a precise ruler in frequency space. The FT results in a series of frequency spikes called a frequency comb (see figure 12) [7, 34]. However, the absolute frequency offset from zero (ω_{CE}) is unknown. This can be determined by mixing two components of an octave-spanning spectrum as shown in figure 13 [34]. The broadband SC source is capable to be used in this method for precise measurement of frequencies in spectroscopic experiments since the frequency comb bandwidth is proportional to the spectral width [7]. One of the potential applications for frequency metrology is to develop an all-optical clock for satellite navigation, communication, and network synchronization [7].

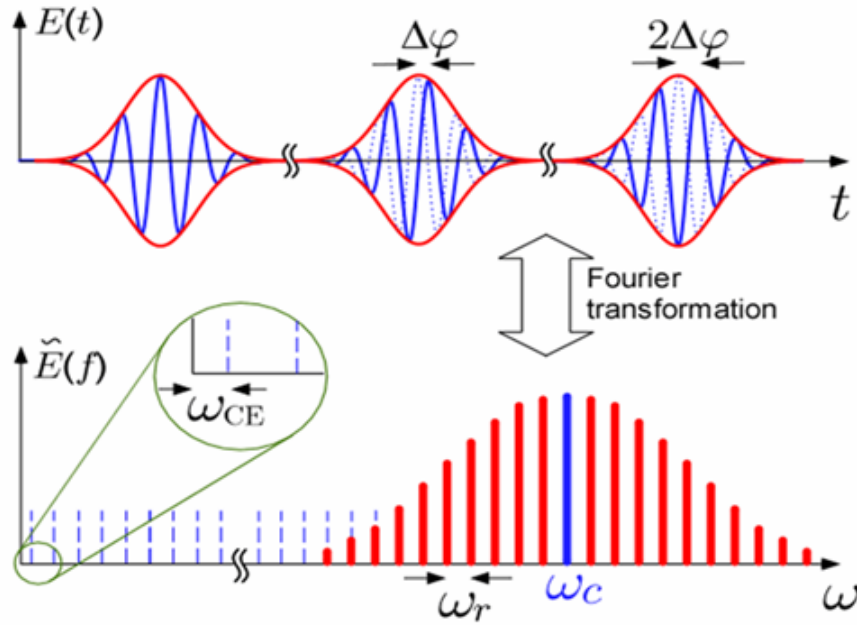


Figure 12: Frequency comb from a mode-locked laser [34]

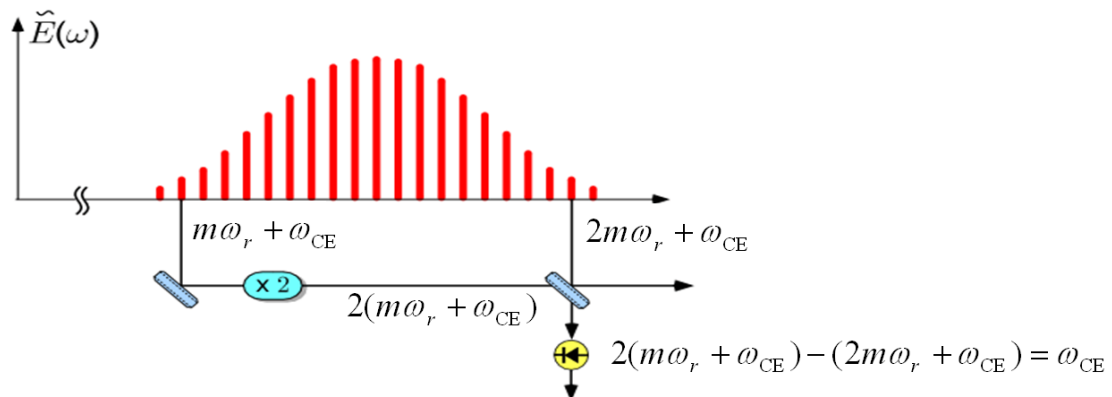


Figure 13: Determination of absolute frequency offset from zero by mixing two components of an octave-spanning spectrum [34]

Frequency metrology requires a phase-stable, octave-spanning SC source with good spectral flatness. Therefore, SC generated from high power femtosecond pulses in the anomalous dispersion regime could be the ideal solution for frequency metrology [11].

2.3.4.4 Pulse Compression

Pulse compression is widely reported in literature using several different approaches [35-38]. One common approach is to apply dispersion compensation to a SC, using chirped mirrors, such that the output pulses of a SC laser are compressed to the sub-10

fs regime [37]. Steinmeyer and Stibenz reported a method to compress the SC pulses down to duration of 3.8 fs using chirped mirrors in [37] in 2005, but the method is only valid for certain bandwidth of SC spectrum (300 nm at an 800 nm centre wavelength) [37]. The other common approach is to use prism pairs with negative dispersion to achieve the compression (see figure 14) [39].

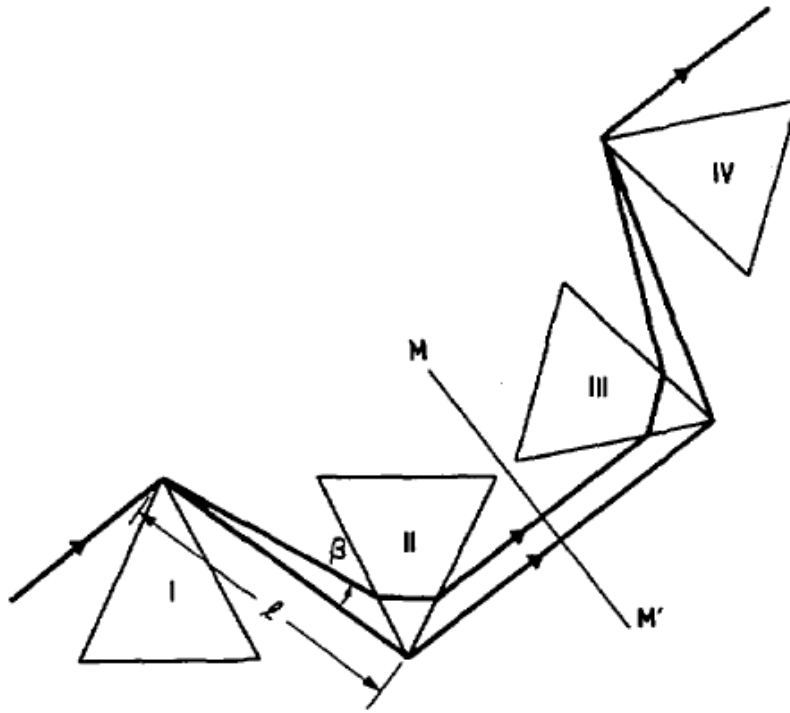


Figure 14: Prism sequence having negative dispersion (The prisms are used at minimum deviation and oriented so that the rays enter and leave at Brewster's angle. The arrangement is symmetric about the plane MM') [39]

The coherence and phase-stability properties of the SC source are essential for pulse compression, and the bandwidth of the spectrum varies depending on approach. Hence, the SC generated from input pump wavelengths either in the normal or in the anomalous dispersion regime could satisfy the requirements for performing pulse compression [11].

2.3.4.5 Wavelength Division Multiplexing (WDM)

Nonlinear effects, which lead to pulse broadening and cross talk, are mostly unwanted side effects in high bit-rate telecommunication systems. However, SC can be used in high transmission-power WDM systems that normally require hundreds of discrete

modulated lasers. By spectrally slicing a SC generated around 1550 nm, one can generate hundreds of channels with only a single laser. Each channel can subsequently be modulated separately to carry data [6]. Recent works done by Nakasyotani *et al.* [40] showed that it is possible to get over 10000 channels using a single 65 nm wide SC source, but the system suffered from several unsolved issues, such as channel spacing dependence of wavelengths [40].

For WDM applications it is desirable for the bandwidth of SC to be as wide as possible and have good coherence. Hence pumping in the anomalous dispersion regime is one of the ideal solutions for generating a SC source for WDM. Pumping in the normal dispersion regime will produce SC with good coherence properties, but will have reduced bandwidth. For WDM with lower requirement on the number of channels, a SC source with pump wavelength residing in the normal dispersion regime could possibly be the best solution [11].

2.3.5 Supercontinuum Generation in Different Guiding Mediums

Supercontinuum generation has been studied intensively in optical fibres, particularly photonic crystal fibres in recent research, both theoretically and experimentally. The majority of experiments with the fibres use silica or doped silica as the core material. However, there are several proposals for using other solid core materials, such as Tellurite (TeO_2) glass (index of 2.3-2.4) [41], chalcogenide ($As-Se$) glasses with high nonlinearity [42], and liquid core [43]. In the next section a few examples of planar waveguide designs for SC generation are reviewed.

2.3.5.1 Conventional Fibres

Before PCFs become commonly used for SC generation (around 1996), a lot theoretical and experimental work was done to analyze the nonlinear effects related to SC [11]. Experiments showed that Raman scattering, SPM, XPM, FWM are involved in SC generation [44-46]. The theoretical analysis of the nonlinear Schrödinger equation (NLSE), done by Hasegawa and Tappert [47], suggested that the soliton propagation in the anomalous GVD regime is possible, which opens up the possibilities for higher-order soliton and soliton fission [48] to occur in the fibres.

2.3.5.2 Highly Nonlinear Fibres (HNLFs)

Highly nonlinear fibres, in which the effective area, the effective length, and the nonlinear coefficient are modified, are designed and fabricated to enhance the nonlinearities discussed in the above two sections. HNLFs are usually obtained by reducing the effective area and increasing the index contrast of the fibres [3, 16]. Several types of HNLFs have been designed based on the above ideas, which include: doped silica fibres with reduced core area, tapered fibres, and PCFs [3, 16].

2.3.5.2.1 Tapered Fibres

The core diameter of tapered fibres can be reduced to below $2\ \mu\text{m}$ without losing the confinement of the optical mode to the core with air as the cladding material. Since the dispersion properties of the tapered structures depends strongly on the core diameter, the ZDW can be shifted down to around 500nm which makes most of a conventional pump source operating in the anomalous dispersion regime, where lots of interesting nonlinear effects occur [3]. SC was produced and studied by Leon-Saval *et al.* [49] and Cordeiro *et al.* [50] with further reduction in core diameter, (under $1\ \mu\text{m}$). Figure 15 [51] shows the optical spectra at the output for 100 fs pulses at average power levels from 60 mW to 380 mW for a 9 cm long tapered fibre with a $2\ \mu\text{m}$ waist. It is clear that the broadening of the spectrum increases with increase in average input power.

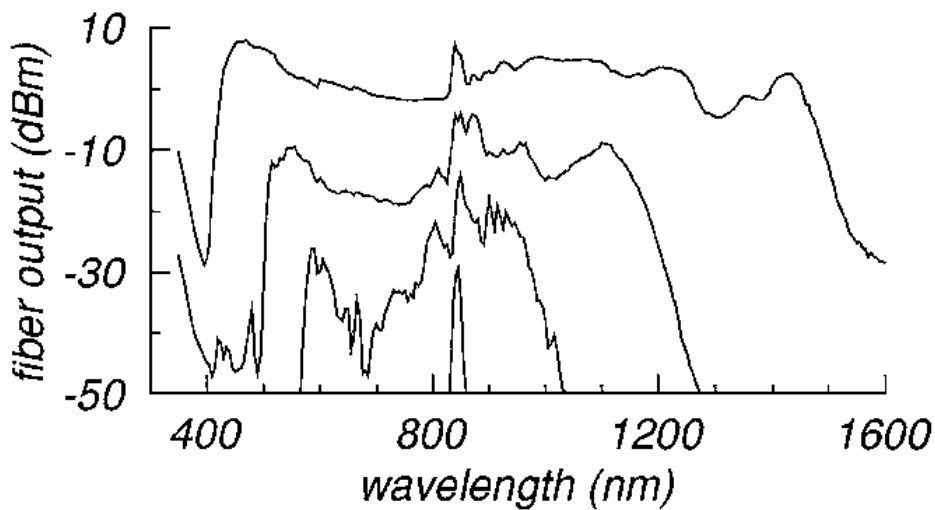


Figure 15: Optical spectra at the output of a 9 cm-long tapered fibre with a 2-micron waist. The average power was 380 mW, 210 mW, and 60 mW from top to bottom along with the input spectrum as the fourth curve [51]

Tapered fibres are not only suitable for the femtosecond pump regime but also for the nanosecond pump regime. Figure 16 [52] shows the generated continuum spectrum with over 400 nm bandwidth from a 100 mm long tapered fibre with core diameter of $0.92 \mu\text{m}$ pumped by a 7 ns pulses at 532 nm (repetition rate: 10 Hz) laser with peak power of 282 W [52].

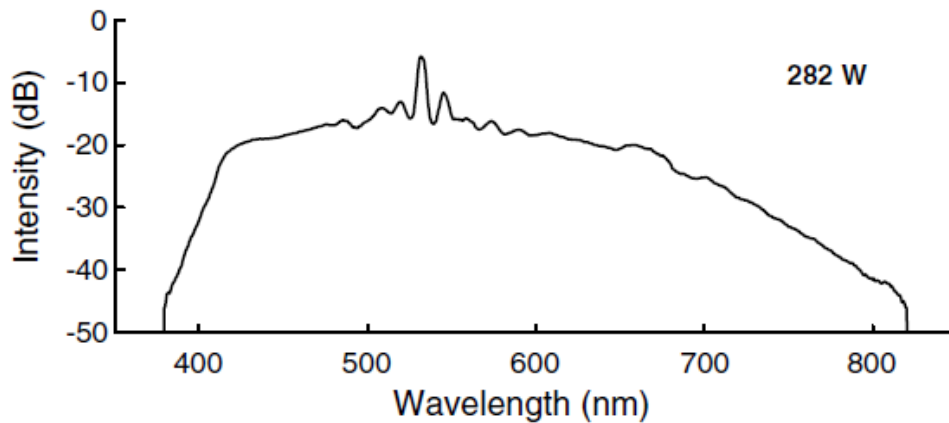


Figure 16: Continuum spectra of tapered fibre with core diameter of 0.92 microns pumped by 282 W peak power, 7 ns pulses laser at 532 nm [52]

2.3.5.2.2 Photonic Crystal Fibres (PCFs)

PCFs are often referred to as microstructured fibres. PCFs utilize photonic bandgap guiding instead of index guiding (as in conventional fibres), so that it is possible to make PCFs single mode at all wavelengths. This is referred to as the endlessly single-mode fibre [53]. PCFs are also capable of providing tight confinement and tunable dispersion properties, which are particularly suitable for the observation of nonlinear effects such as SC [16]. Due to the special properties of PCFs, a large amount of work has been done on SC generation since year 2000. This section provides several examples relating to the input pulse duration, ZDW properties, pump source, and polarization effects.

- Example of picosecond pump pulse:

Figure 17 [54] shows output spectra with a 10 m long fibre and input peak powers of 675 W, 225 W, and 120 W (from top to bottom) [54]. The experiment is carried out with 60 ps input pulses at wavelength of 647 nm, which is in the normal GVD regime of the fiber (ZDW at 675 nm) [54].

Although the coupling efficiency is only around 45%, the spectral broadening becomes quite obvious at peak power of 675 W [54]. As discussed in section 2.3.1, the initial broadening is provided by SRS, but this is not significantly wide. As the pulses propagate further, SPM-induced broadening gives rise to the SC spectrum [11, 54].

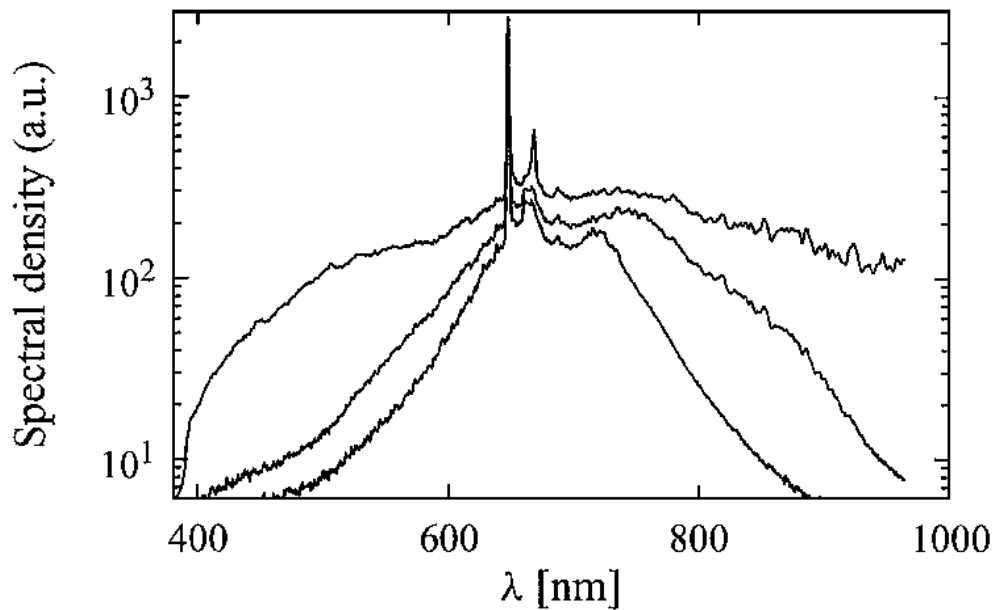


Figure 17: Output spectra with a 10 m long fibre and for input peak powers of 675 W, 225 W, and 120 W (from top to bottom) [54]

- Example of CW source:

The SC is also produced by CW input by Abeeluck *et al.* (see Fig. 18) in 2004 [55]. Three HNLFs were fabricated with ZDWs at 1481 nm, 1481 nm, and 1478 nm. A CW pump with wavelength of 1486 nm was used, which resides in the anomalous GVD regime of each HNLF. The results show that the spectral broadening could occur with input power of 0.4 W, but both the output spectral flatness and the spectral power are not good enough comparing to the higher power input. Comparing figures 18(a), 18(b), and 18(c), it shows that longer propagation distance gives a better flatness of SC at the output. Combined with the dispersion effect, the nonlinear effects initiated by the higher power input, MI, SRS, and FWM play important roles on the formation of SC when using CW pump input [3, 55].

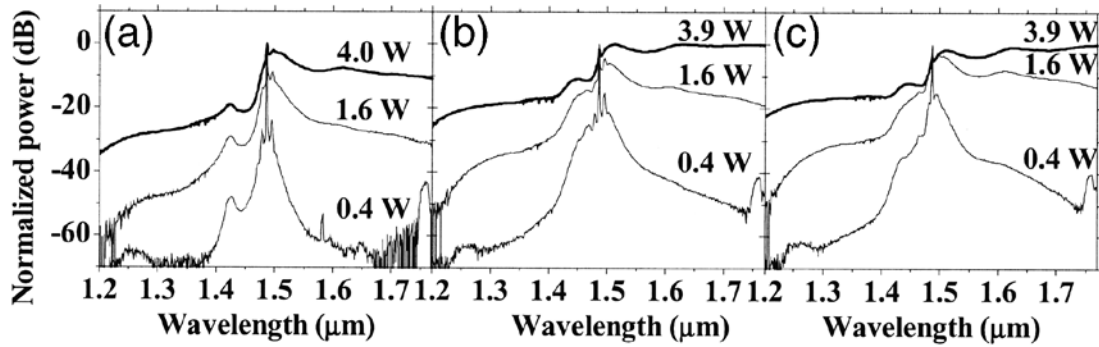


Figure 18: Supercontinuum spectra as function of CW input power in PCF length of (a) 0.5, (b) 1.0, and (c) 1.5 km [55]

- Example of femtosecond pump pulse:

Femtosecond pulses can be used to create SC in a PCF with the ZDW around 800nm and pump wavelength near the ZDW even for very short fibre lengths [3]. Figure 19 [56] shows the resulting SC created by 100 fs – 0.8 nJ pulses at 790 nm launched into a 75cm fibre demonstrated by Ranka *et al.* in 2000 [56]. The output spectrum shows extreme broadening expanding from 390 to 1600 nm with good flatness over the entire bandwidth. As discussed in section 2.3.3, SPM and SRS are the dominant nonlinear effects responsible for producing this flat SC when a femtosecond pump source is used [3, 11, 56].

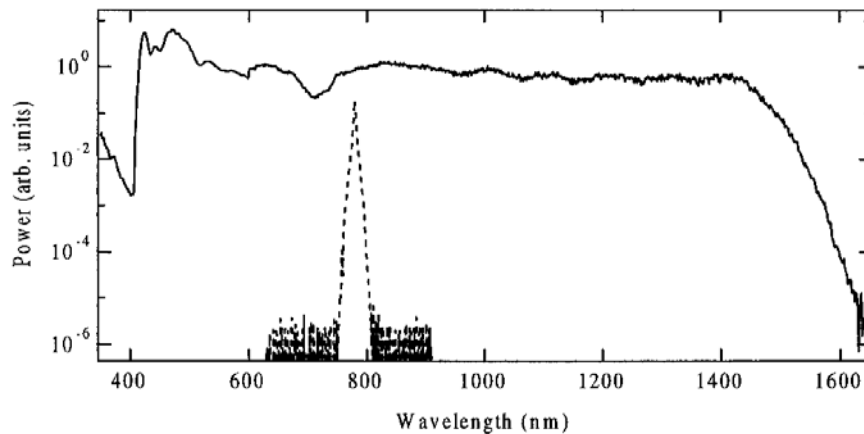


Figure 19: SC in a 75 cm long PCF. Dashed curve shows the spectrum of the 100 fs – 0.8 nJ input pulses [56]

The supercontinuum for highly nonlinear materials other than silica glasses has also been investigated. For example, photonic crystal fibres made from tellurite glass pumped by 100 fs pulses of 1.9 nJ at 1550 nm [57] show

extremely wide bandwidth (over 4000 nm) (see Figure 20 [57]), from 789 nm to 4870 nm.

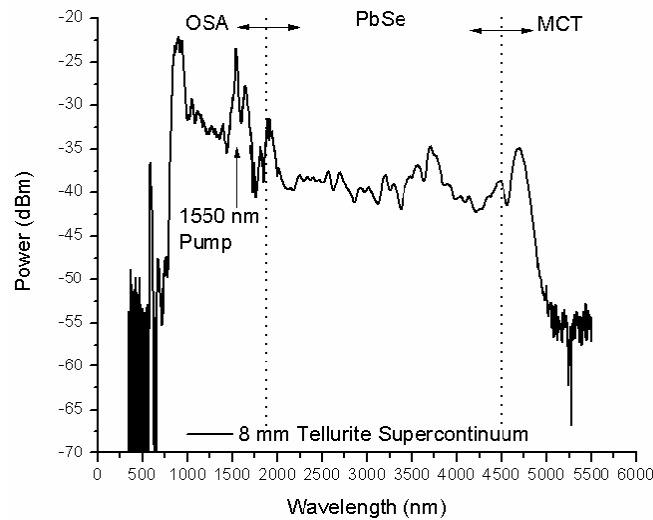


Figure 20: SC spectrum output of an 8 mm Tellurite PCF pumped by 1.9 nJ, 100 fs laser at 1550 nm. Spectrum is analyzed by optical spectrum analyzer (OSA) and monochromator with lead selenide (PbSe) or mercury cadmium telluride (MCT) [57]

- Example of multiple pumps:

When two or more pumps with different wavelengths are used as sources for SC generation in PCFs, XPM becomes more significant [3]. One example of dual pump source initiated SC is presented by Champert *et al.* [58] in 2004, (see Fig. 21) [58]. In the figure below, the pictures show the diffracted beams of the SC in the case of (a) single and (b) dual pump configuration. The graph shows the resulting power spectra for (a) single pump (532 nm), (b) dual pump (532 and 1064 nm), and the far field pattern of the corresponding single mode transverse energy distribution is shown in the inset [58]. Pulse durations for the two pumps were 420 ps and 600 ps for 532 nm and 1064 nm pulses, respectively [58]. The average power of the green pulses (532 nm) is 3 mW with peak power of 1.5 kW. Under single pump conditions, Raman scattering is dominant, and up to seven Raman orders are generated, (see fig. 21(a)). With the additional infrared (IR) pump (1064 nm), continuum is generated between 350 nm to 750 nm with great flatness (ignoring the peak at 532 nm [58]). Since two pumps are used, XPM affects both the larger wavelength region and smaller wavelength region (compared to 532 nm peak of the

spectrum) of the continuum. Other nonlinear processes responsible for the generation of SC include SPM, FWM, and SRS [58].

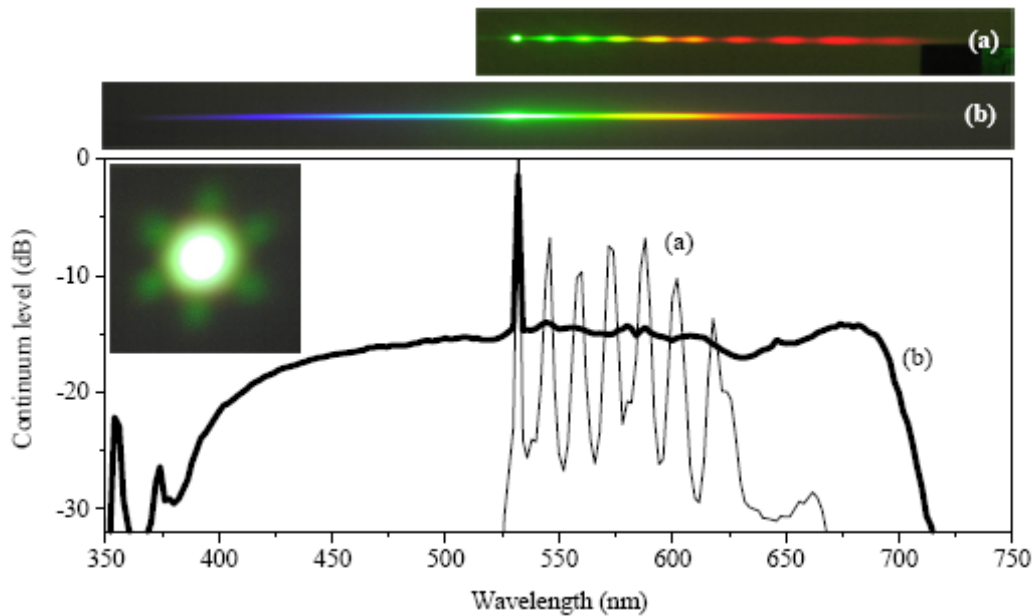


Figure 21: Continuum generation in the case of (a) single (532nm) and (b) dual pump (532 and 1064 nm) configuration. Picture: diffracted beams. Graph: corresponding recorded power spectra. Inset: far field pattern of the corresponding single mode transverse energy distribution [58]

- Example of PCF with two ZDW:

One special type of PCF has two ZDWs. Figure 22 [59] shows the measured supercontinuum spectrum obtained by pumping low power nanosecond pulses into a 20 m PCF with two ZDWs at 745 nm and 1175 nm [59]. In this experiment, the dual pump method is employed with pulse durations of 10 ns and two pump wavelengths at 1064 nm and 532 nm [59]. The dispersion profile of the PCF allows phase-matched degenerate FWM to occur in the anomalous dispersion regime at low powers. Similar nonlinear effects are involved in the creation of SC as the multiple pumps example above. The output spectrum in this experiment expands from 1050 nm and 1400 nm. Because the infrared pump can exacerbate the FWM and inhibit the SRS, the output continuum is a single-mode white laser [59].

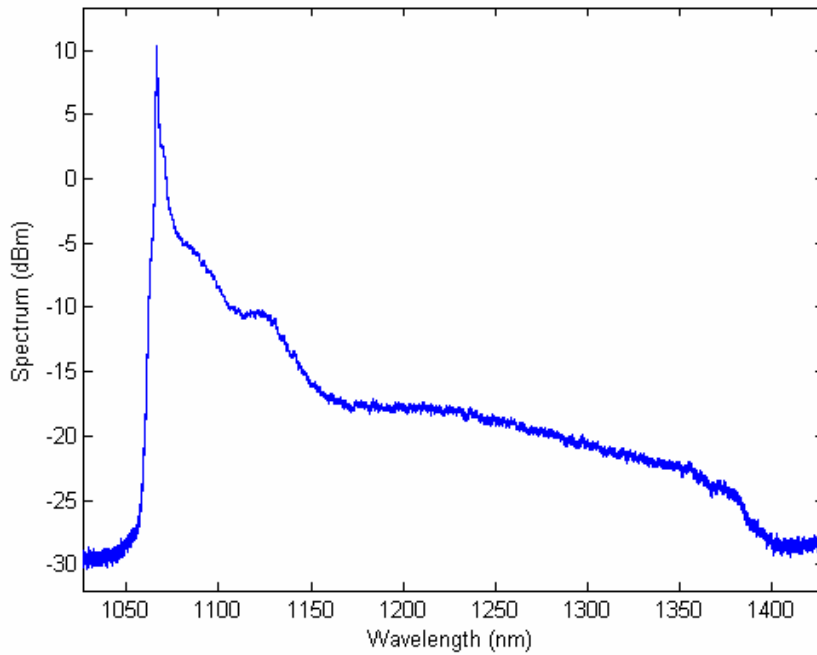


Figure 22: Measured supercontinuum spectrum using a 20 m PCF [59]

- Example of polarization effects on the SC:

Polarization effects can either be introduced by the state of polarization (SOP) of the input pulses or by the birefringent of the fibre [3]. Figure 23 [60] shows the supercontinuum output images for different input polarization states [60], and Figure 24 [61] shows the effect on output spectrum of input polarization on the SC: (a) $\phi = 0^\circ$ (fast axis), (b) $\phi = 45^\circ$, and (c) $\phi = 90^\circ$ (slow axis). The duration of the input pulse is 200 fs, with average power of 56 mW at wavelength of 732 nm [61]. The dashed lines in the figure indicate the ZDW of the fibre along the slow and fast axes, and demonstrate that the dispersion properties of the fibre are affected by the SOP as well [3, 61].

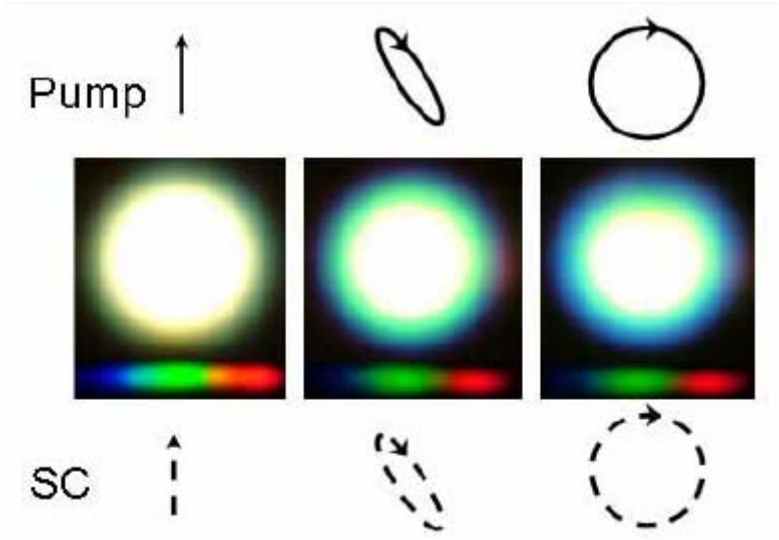


Figure 23: Supercontinuum images under linear (left), elliptical (middle), and circular (right) polarization excitation conditions [60]

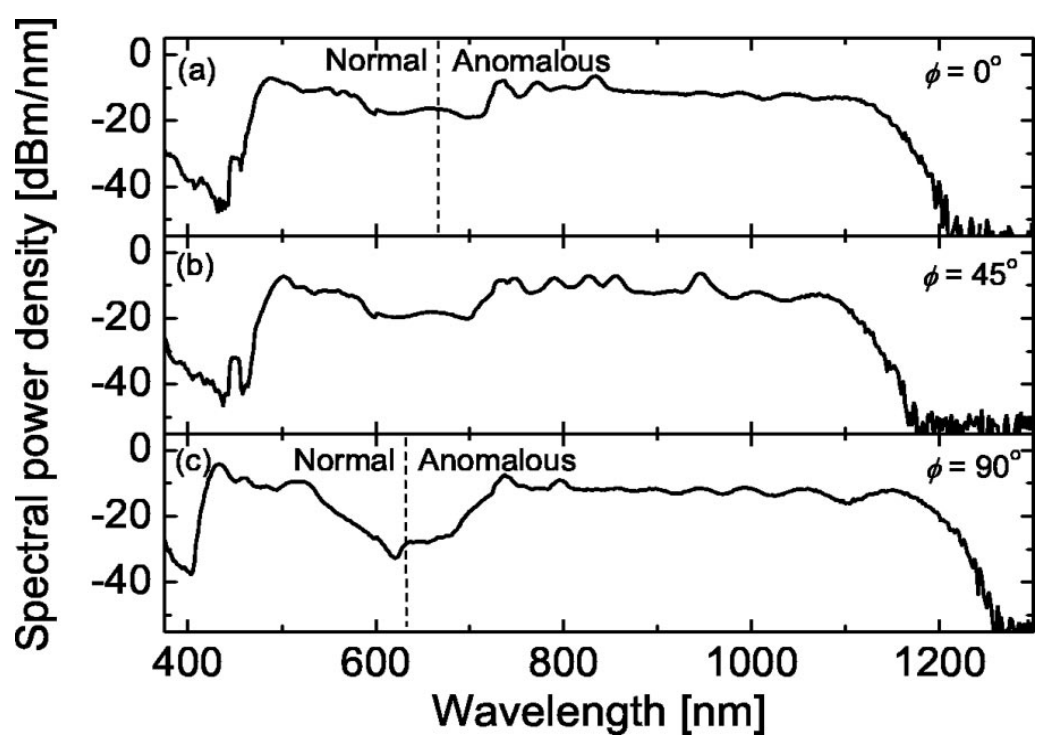


Figure 24: Effect of input polarization on SC, at the degree of polarization of (a) 0° , (b) 45° , (c) 90° with 200 fs – 56 mW input pulses (dashed line indicates the ZDW position) [61]

2.3.5.3 Planar Waveguides

There are very few examples in literature using high index planar waveguides for SC [12, 13]. Similar to fibres, the dispersion properties of planar waveguides vary with

the dimensions as well as the core materials [12, 13]. Figures 25 [12] and 26 [13] show the GVD properties of slab & rib, and ridge waveguides, respectively.

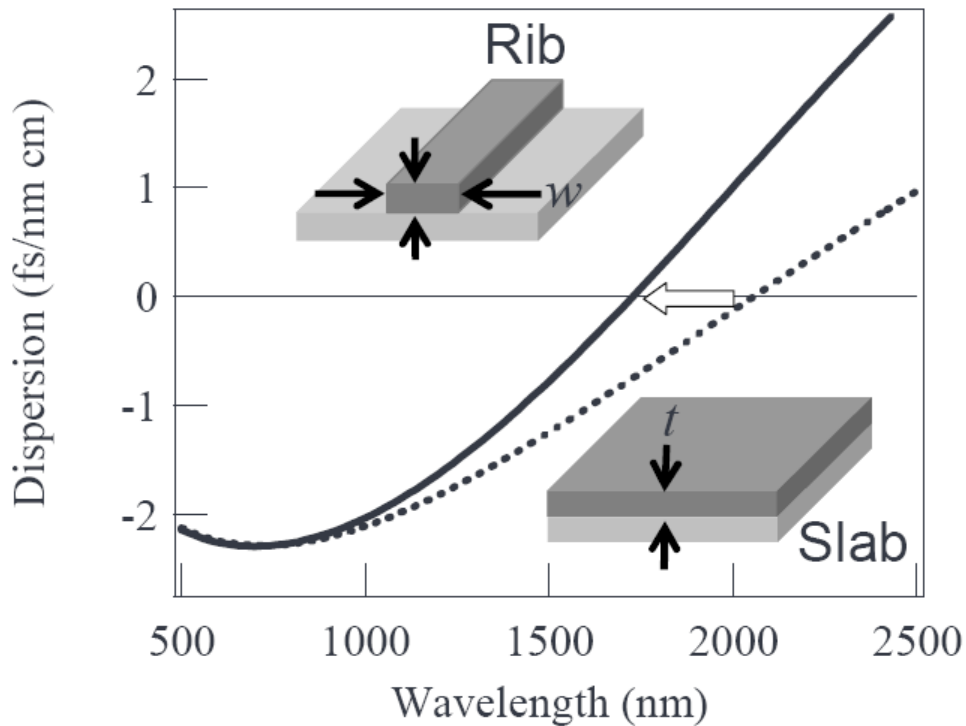


Figure 25: Dispersion properties of the 1 μm and 1 x 1 μm rib waveguide with tantalum pentoxide as core material, rib (solid line) and slab structure (dashed line) [12]

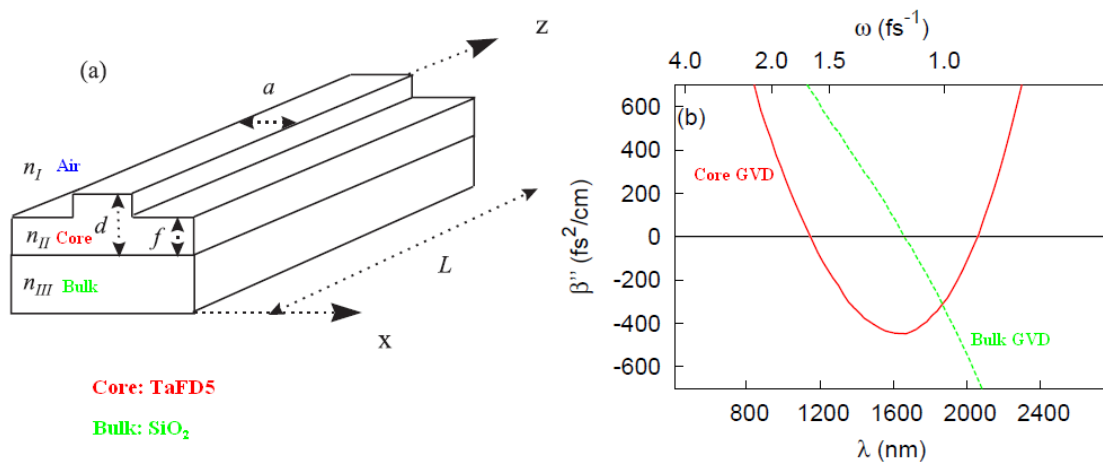


Figure 26: Air-TaFD₅-SiO₂ planar waveguide: (a) ridge structure with $a = 4 \mu\text{m}$, $d = 1 \mu\text{m}$, and $f = 0.5 \mu\text{m}$ (b) GVD properties of the waveguide [13]

Figures 27 [12] and 28 [13] show SC using femtosecond input pulses obtained from the planar waveguides shown above. For an 80 fs chirped input pulse at 1.55 μm (in

the normal dispersion regime) with power of 50 pJ, the result from rib waveguide (fig. 27) show that the SC spectrum expands from 950 nm to 1700 nm [12]. For a 150 fs input pulse at 1185 nm (in the anomalous dispersion regime near the first ZDW of the guide) with peak intensity of $0.2 \text{ TW}/\text{cm}^2$, the ridge waveguide result (fig. 28) shows that the spectrum expands from 750 nm to 2400 nm [13]. Both experiments have relatively wide spectrum, but it can be seen that the flatness of the spectra is not as excellent as the result obtained for femtosecond input in the PCF demonstrated by Ranka *et al.* in 2000 (see fig. 19) [56].

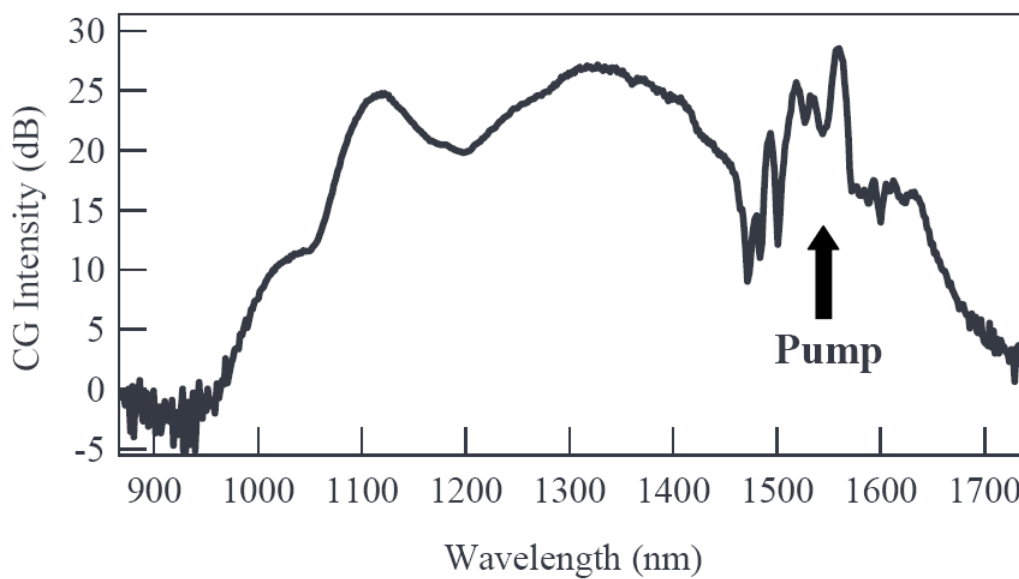


Figure 27: SC generated 2 x 1.8 μm rib waveguide pumped at 1.55 microns [12]

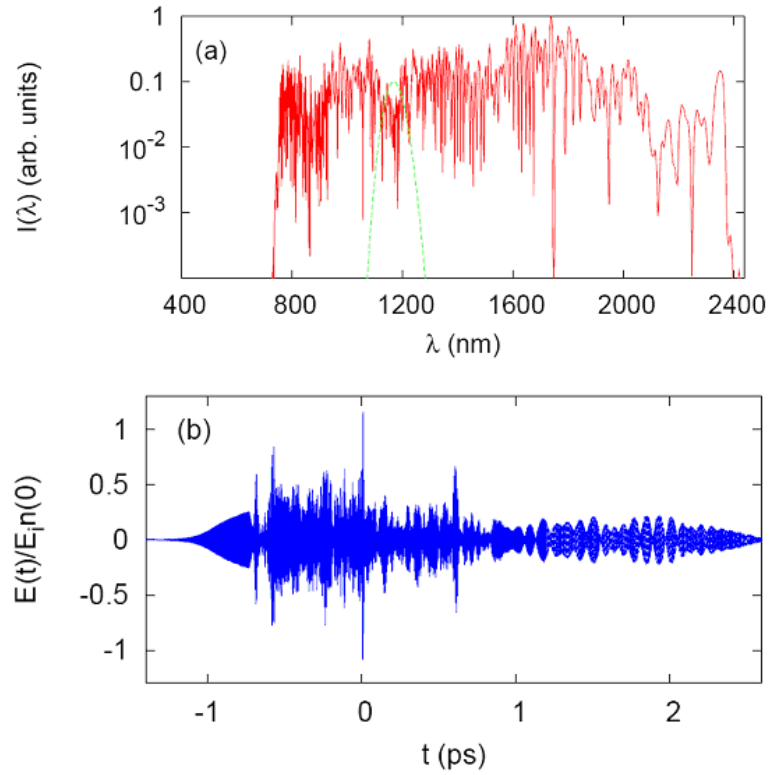


Figure 28: SC generated in the Air-TaFD₅-SiO₂ ridge waveguide: (a) spectrum, input (green dashed line) and output (red solid line) (b) temporal shape [13]

The mechanisms for generating the SC in the planar waveguides are expected to be similar to those in PCFs, but the dominant process has not yet been identified or discussed in current literature. Thus, further research is required for the planar waveguide designs, and is undertaken in the following chapters of this thesis.

Chapter 3 Simulation of Tantalum Pentoxide Planar Waveguide Dispersion Properties

3.1 Planar Waveguide Approach

As mentioned in the introduction to this thesis, planar waveguides not only provide a convenient interconnect interface between sub components of a PLC, but also provide much more important functionality when fabricated from a nonlinear material. In the context of nonlinear optics they provide a medium for phase-matching, which in turn affects most nonlinear processes including: XPM, FWM, and spectral broadening through Kerr nonlinearity, all of which are important for an on-chip tunable laser.

One of the key issues for nonlinear waveguide devices is the choice of the core material. The material must meet two criteria to satisfy the design requirement: 1) high refractive index, and 2) high nonlinearity. Some of the most promising candidate materials therefore include: titanium dioxide (TiO_2), Tellurite (TeO_2), chalcogenide ($As-Se$) glasses, and tantalum pentoxide (Ta_2O_5). Figure 29 shows a Matlab simulation of material dispersion for Ta_2O_5 , TiO_2 , TeO_2 , and SiO_2 according to spectroscopic ellipsometry studies in references [62-64] (see Appendix A, B, and C for material dispersion equations and fitting parameters). Tantalum pentoxide (Ta_2O_5) is chosen as the material of choice for this project due to availability and familiarity with processing techniques at Southampton. The linear refractive index of Ta_2O_5 is

larger than 2.05 ($n_{\text{Re}} > 2.05$), i.e. the real part of refractive index, for wavelengths longer than 300 nm, which introduces a large index difference with respect to silica glass (which normally has a refractive index of 1.455), and has little absorption, indicated by the imaginary part of refractive index in the figure, for any wavelength of light above 350 nm. The measurements taken by Tai *et al.* [65] for a 1 cm long rib waveguide in 2004 shows that nonlinear refractive index of Ta_2O_5 , $n_{2_Ta_2O_5} = (7.23 \pm 0.36) \times 10^{-19} m^2/W$ at a single fixed wavelength of 800 nm. This is higher than silica glass ($n_{2_SiO_2} \approx 2.2 \times 10^{-20} m^2/W$) by more than one order of magnitude [65].

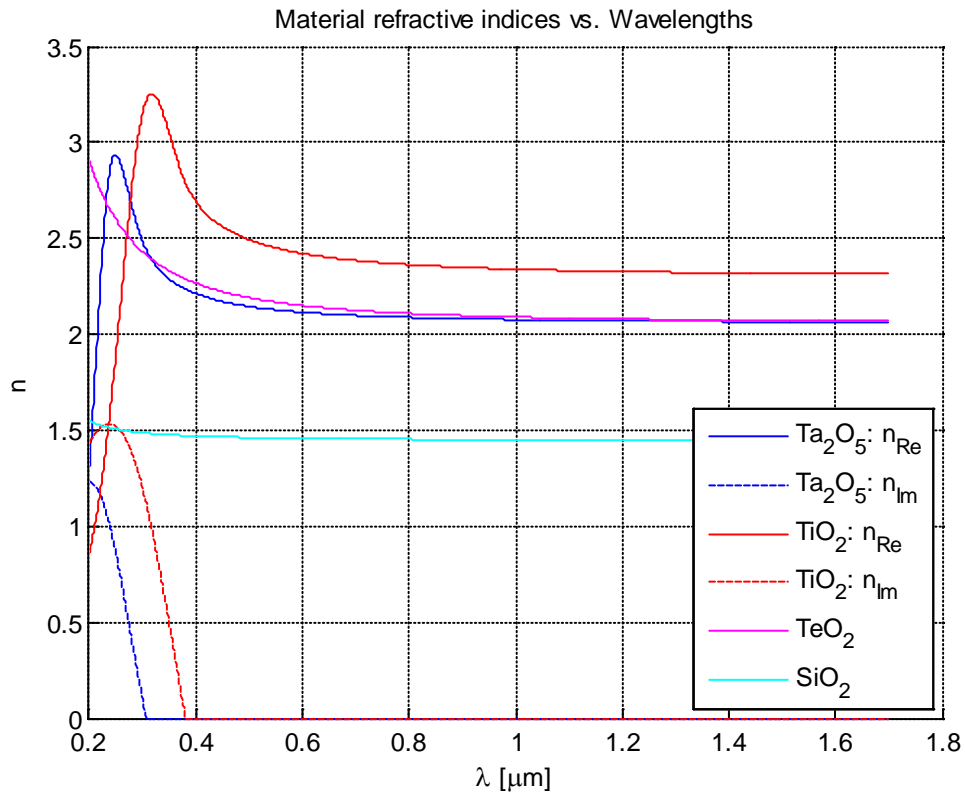


Figure 29: Linear refractive index of potential core materials, solid lines are real part and dashed lines are imaginary part of the refractive index [62-64]

A second key issue (apart from the choice of core material) is the waveguide geometry. This plays an important role in the design of nonlinear optical devices, by providing a means to manipulate the optical power density through spatial confinement of light, and enhancement and control of nonlinear effects through

modification of waveguide dispersion conditions, which in turn affect phase matching condition. In a simple context, planar waveguides can be divided into rib and ridge categories. Similar to the concept of HNLFs, tapers and photonic crystal structures can also be incorporated into planar waveguides to further modify their modal and dispersion characteristics. Incorporating photonic crystals in nonlinear planar waveguides introduces the possibility to create devices with multiple ZDWs and out-of-plane coupling.

For the design of waveguide based frequency tripling and parametric wavelength conversion devices, (discussed in subsequent chapters of this thesis) which rely heavily on phase-matching over wide wavelength ranges, the derivation of highly accurate dispersion relations (e.g. effective refractive index of the guided modes as a function of wavelength) for the constituent guides is of paramount importance.

The use of planar waveguides for supercontinuum generation is in itself currently at an early stage of development, and is relatively under-represented in the literature. The reported SC generated from planar waveguides to date lack spectral flatness and stability as seen in section 2.3.6.3 above.

As shown in the section 2.3, the ZDW is a key parameter which largely determines which of the nonlinear optical effects is dominant in the generation of SC. Hence, the determination of the ZDW is an important issue for the waveguide design. Secondly, according to equation 13 in 2.2.7, the precise values of k (related to effective mode index) are critically important to the efficiency of nonlinear processes such as SPM, XPM, FWM, and so factors affecting these are explored in detail theoretically in this chapter.

3.2 Discussion of Numerical Accuracy

Accurate derivation of the ZDW is in practice extremely tricky, due to the fact that this is dependent on the 2nd derivative of the dispersion relation. Any factors which change the gradient of the dispersion relation by even a very small amount will have an adverse effect on the calculated ZDW. Great effort was therefore taken to ensure

that numerical accuracy of the simulations was of the order of 12 decimal places. To achieve this, material dispersion was measured on practical samples, by spectroscopic ellipsometry, and the actual values of n and k (as a function of wavelength) for the real material fed back into the simulation software. Conventional simulation methods based on simple analytic boundary condition solving algorithms (such as beam propagation method) provide good accuracy for 1-dimensional geometries but perform poorly when transferred to two-dimensional structures, particularly in weakly confined waveguide structures (such as ridge waveguides) close to cut off wavelength. Hence for the calculation of the ZDW a fully vectorial finite element method was adopted. To ensure accuracy, convergence trials were conducted, investigating the convergence value for guided mode index (n_{eff}) as a function of grid density, at wavelengths close to cut off. Having established and validate a high level of numerical accuracy, full wavelength scans were performed for specific waveguide geometries.

3.3 Simulation Results

In this section we investigate the possibility of manipulating the zero dispersion wavelength (ZDW) to shorter values by simply adjusting the waveguide cross sectional profile dimensions with the intent of creating a low power, compact planar SC device capable to be driven by a low cost solid state pump source. This section shows simulation results investigating properties of the ZDWs in slab, rib, and ridge planar waveguide geometries based on a Ta_2O_5 core and silicon dioxide (SiO_2) cladding materials. This data is also relevant to the design of tapered couplers and nano-wire waveguides for SC generation.

3.3.1 1-D Slab Waveguides

To obtain an intuitive insight into the evolution of the behaviour of planar guides, (particularly with respect to the ZDW) we start by investigating the linear dispersion properties of one-dimensional (1-D) slab waveguides, calculated using a simple analytical method in Matlab. We later investigate at how the behaviour changes as we switch to a two dimensional geometry.

Figure 30 [14] shows a slab waveguide with core thickness of $2a$. In the case of a symmetrical guide, the same materials are used for cladding and substrate. For a non-symmetrical waveguide cladding and substrate materials are not the same. The material dispersion of both Ta_2O_5 and SiO_2 are included (see Appendix A and Appendix B) in the simulation. The effective index of slab waveguides are computed through the mode calculations using eigenvalue equations as defined in [14] with respect to input wavelength. Figure 31 shows the GVD curves for a symmetrical slab waveguide with a core thickness of $4 \mu m$, where Ta_2O_5 is chosen as the core material and SiO_2 is used as cladding and substrate. The terms TE and TM correspond to the Transverse Electric and Transverse Magnetic mode of light propagation (see insets of figure 30) [14].

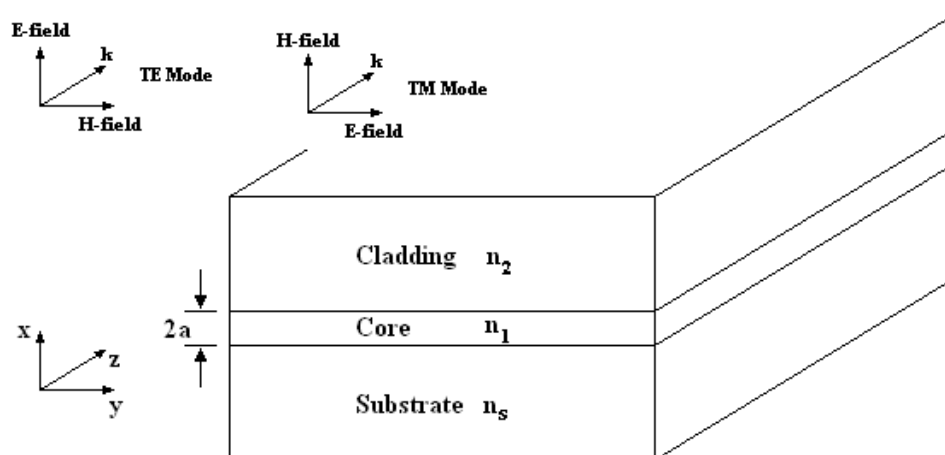


Figure 30: Slab waveguide (Insets show electromagnetic field distribution of TE and TM modes) [14]

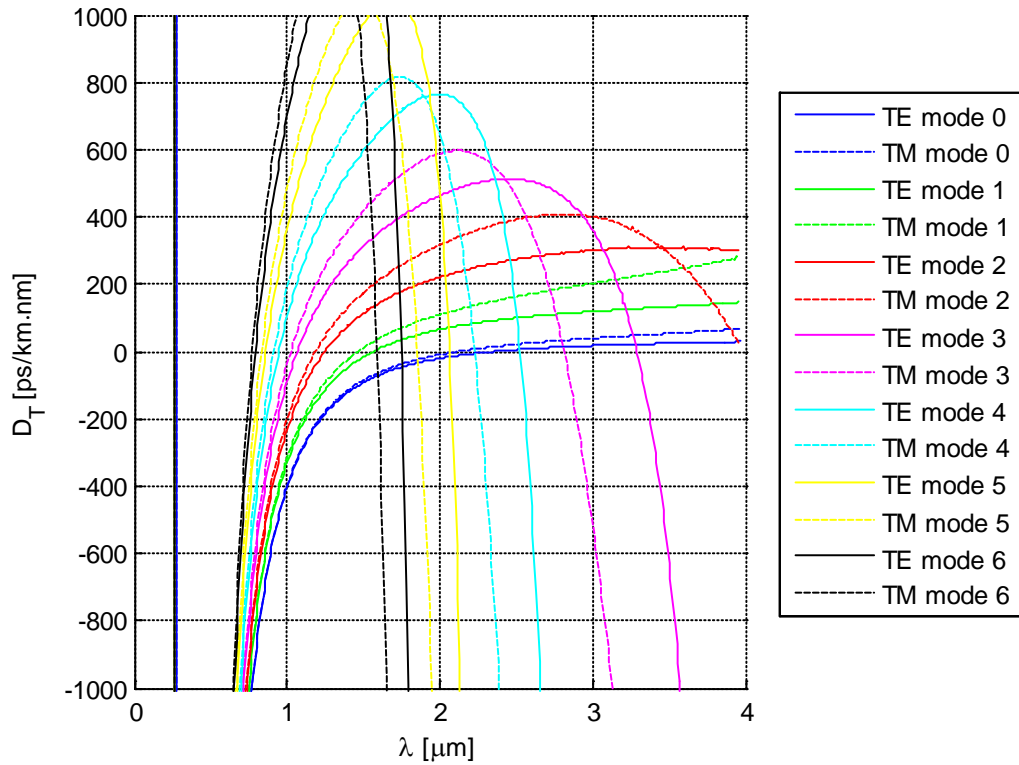


Figure 31: GVD curve of the symmetrical slab waveguide with core thickness of 4 μm

Figure 31 shows clearly that the fundamental TE mode has the largest ZDW at around 2.1 μm whereas higher-order modes may have two ZDWs. The simulations show that the position of the ZDW corresponding to each mode is also dependent on the core thickness of the slab waveguides (see fig. 32). Figure 25 indicates that the ZDW of a 1 μm thick slab waveguide is around 2100 nm. The estimated ZDW From the ZDW curve of TE fundamental mode in figure 32 is around the same as obtained in [12], therefore, the simulation results are successfully validated. It is clear from the figure that for a femtosecond pulse at 800nm, the pump must be coupled to mode 2 in order to operate close to the ZDW. In practice, higher order modes (with relatively low effective mode index values), whose mode energies extend some distance into the surrounding cladding material, experience large leakage and loss of optical power due to scattering from roughness at the core-cladding interface, compared to fundamental and lower order modes, which are well confined to the core.

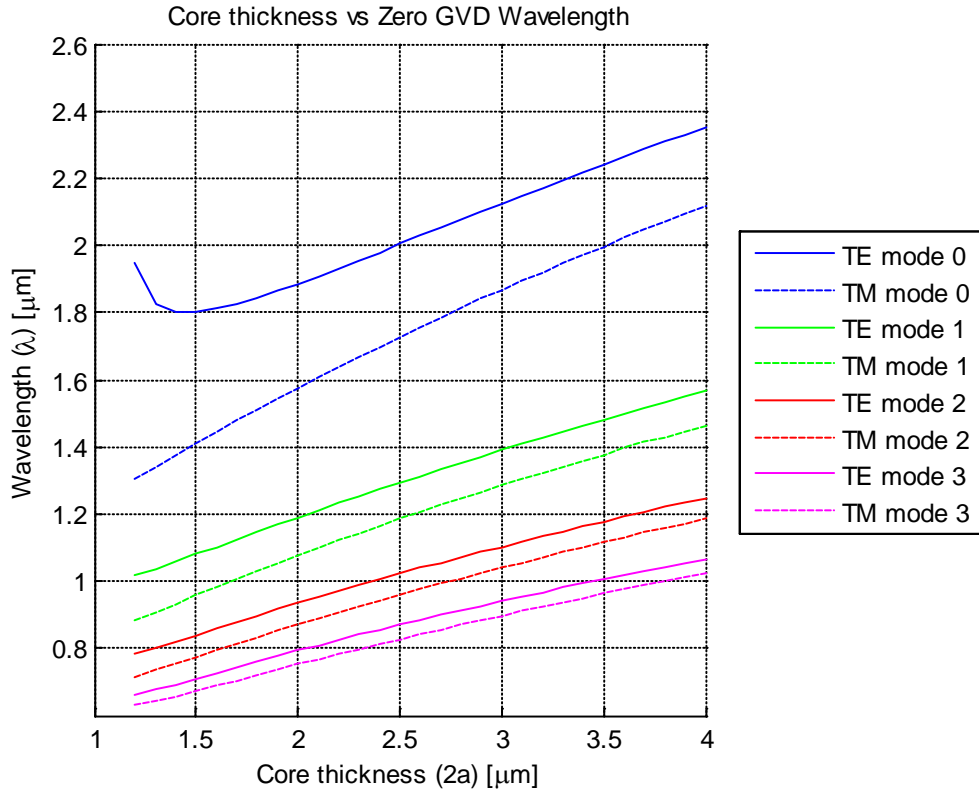


Figure 32: ZDW vs. core thickness for symmetrical slab waveguide

Although slab waveguides are not ideal for SC generation, they are useful for characterizing the basic material properties, such as material loss, in preparation for fabricating more complex structures such as the rib and ridge structures. However, if the slabs are combined with photonic crystals (photonic crystal slabs) [66], they can then be useful for SC generation since the photonic crystal can significantly modify the dispersion properties as suggested in [66] and provide alternative spatial confinement mechanisms to conventional guides.

3.3.2 2-D Rib/Ridge Waveguides

Two-dimensional (2-D) rib and ridge waveguide structures provide more flexibility for modifying waveguide dispersion properties than slab waveguides. Figure 33 shows the cross-sectional view of two ridge waveguides with etch-depths of 25% and 50%. Rib waveguides can be viewed as a special type of ridge waveguides, where the etch depth reaches 100%.

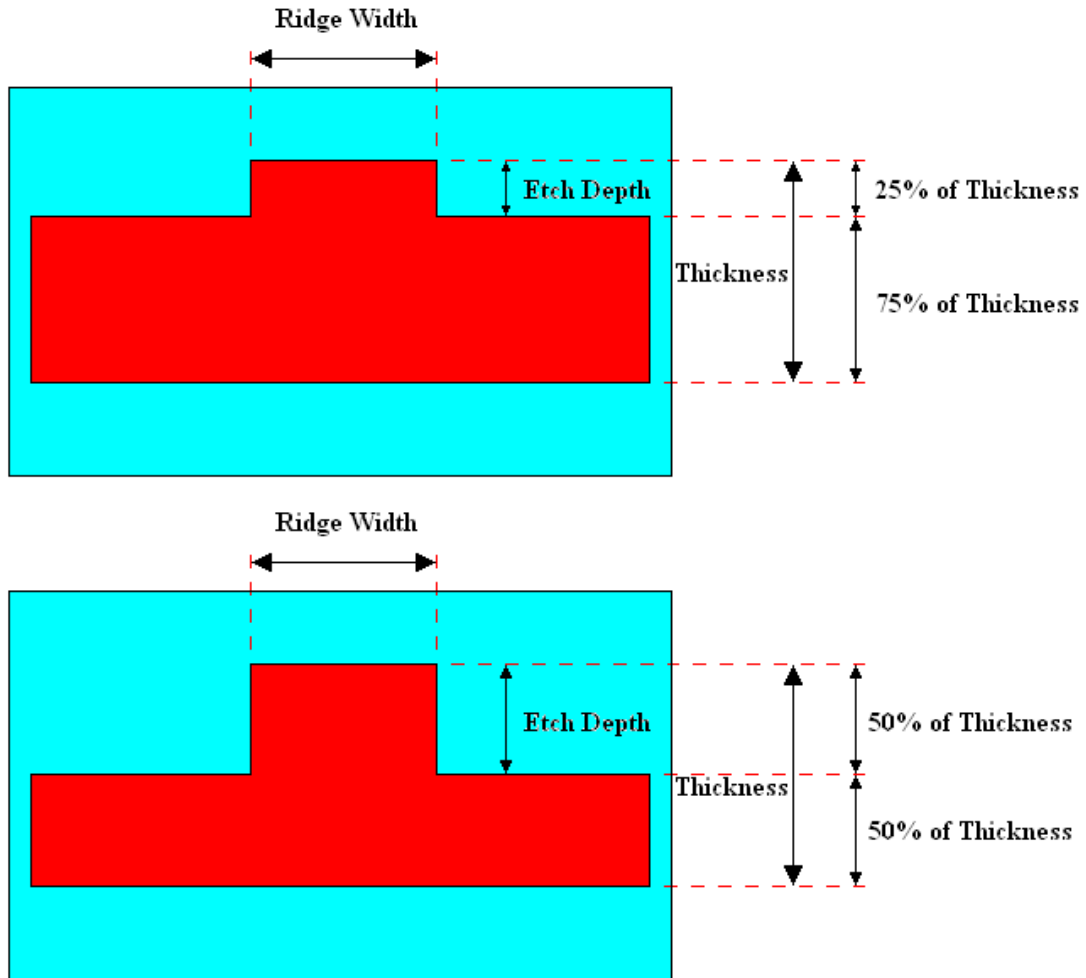


Figure 33: Cross-sectional view of the 25% and 50% etched ridge waveguides

Since the eigenvalue method loses accuracy for 2-D waveguides (particularly for modes approaching cut-off), the finite element method (FEM) is employed to solve the 2-D waveguide dispersion properties with high accuracy. The finite element method (FEM) is a numerical technique for finding approximate solutions of partial differential equations (PDE) as well as of integral equations. The solution approach is based either on eliminating the differential equation completely (steady state problems), or rendering the PDE into an approximating system of ordinary differential equations, which are then numerically integrated using standard techniques such as Euler's method. The Finite Element Method is one of the choices for solving PDE over complicated domains (like optical field), when the domain changes (as during the propagation of the optical field) [67]. Due to the large amount of calculations involved in FEM simulations, 2-D waveguide properties were computed using the RSoft CAD Suite software package. The simulation process involves:

- 1) Initial setup of the waveguide structures and material properties as follows:
Simple 2-D waveguides are defined in the RSoft CAD using rectangular shaped segments. Index profiles of each segment is defined either by using a symbol table or material editor in the RSoft CAD. In case of overlap between segments, the segment priority level must be defined that the higher level segment index will overwrite the lower level one in the overlap region. Although the sample sidewalls are not exactly vertical due to imperfect fabrication processes (as shown in figure 55 in chapter 6), the simulations show little effects of changing from vertical to diagonal side-walled segments.

- 2) Selecting the computation grid size:
To ensure the accuracy of the calculations, the grid size needs to be defined for FEM. Although the structures are in 2-D, three-dimensional simulations are required in the computation, thus, the grid size must be defined in x, y, and z directions for the waveguide structure. RSoft CAD provides an advanced feature to allow sub-grid calculation. Previous experience in solving Maxwell's Equations shows that most rapid change in electromagnetic field is expected to occur at the boundaries of the waveguide structure. Therefore, the sub-grid option is used to reduce the simulation time by defining sub-grids at the waveguide boundaries. To find the optimal grid size, the grid is progressively reduced in size, and the convergence of simulation results (in particular n_{eff}) analyzed. The optimum grid size is the largest grid size value where n_{eff} values lie within a given acceptable error value to the known convergence limit (1/10 of the waveguide size). In order to further reduce the simulation time, RSoft CAD provides a 'symmetrical option' for some of the sub-programs (such as FemSIM). Because the simple rib/ridge structures are symmetrical along the x-axis, the simulation can take the advantage of the symmetrical option to minimize the simulation time by mirroring the calculated field about this axis (rather than calculating it again), and so reduces simulation area.

3) Calculating optical mode profiles and effective indices:

The mode profile and computation is done using the FemSIM sub-program in the RSoft CAD, where up to 40 supported modes are calculated. Although only a few of the solved modes are relevant, a large number of higher order modes are computed to prevent misbehaviour of the software (the sorting algorithm can fail when there are many closely spaced solutions, again particularly close to ‘cur-off’ value). The software simulates the mode profiles and index variations with respect to changes in waveguide dimensions (thickness and width), etch profiles (for the ridge waveguides), and input wavelength. Figure 34 shows mode profiles for fundamental TE modes at a wavelength of $1 \mu\text{m}$ in a $2 \mu\text{m} \times 1.8 \mu\text{m}$ ridge waveguides with etch depth of (a) 25%, (b) 50%, (c) 75%, and (d) 100% (i.e. rib).

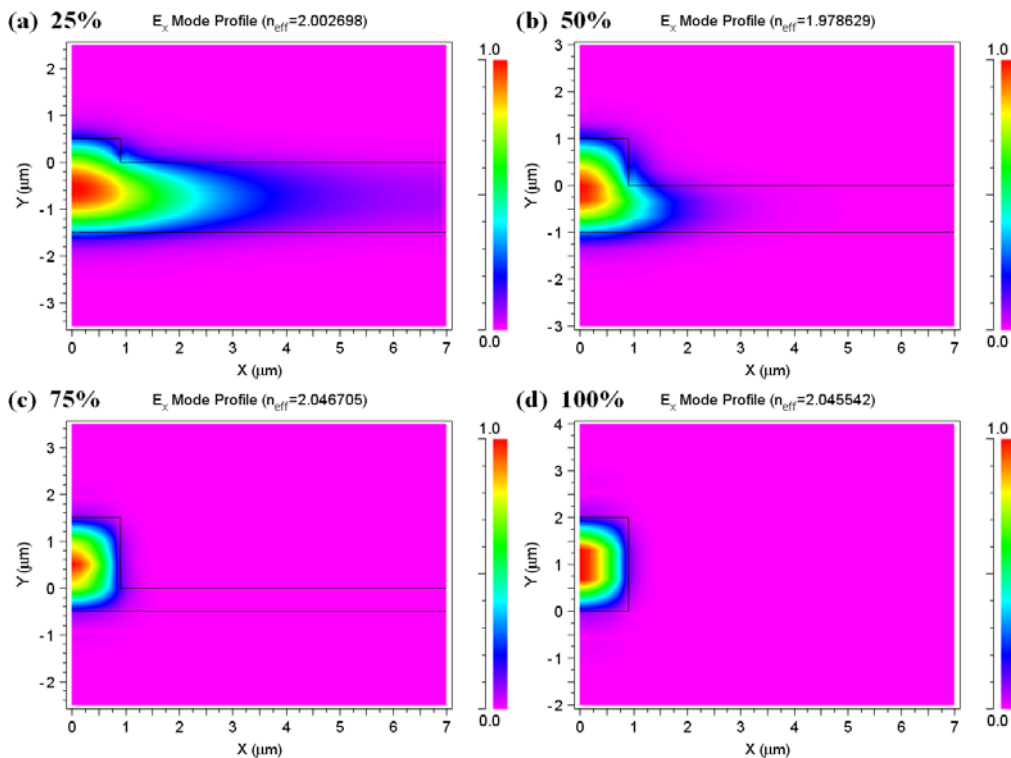


Figure 34: Fundamental TE mode profiles at input wavelength of $1 \mu\text{m}$ in $2.0 \times 1.8 \mu\text{m}$ ridge waveguides with the etching profiles: (a) 25%, (b) 50%, (c) 75%, and (d) 100% (i.e. rib)

4) Computing the GVD curves:

After step 3), all relevant mode profiles are examined to verify that the correct data is collected for each of the settings. The GVD curves are then calculated using the RSoft built-in function ‘disperse’, which is able to simultaneously

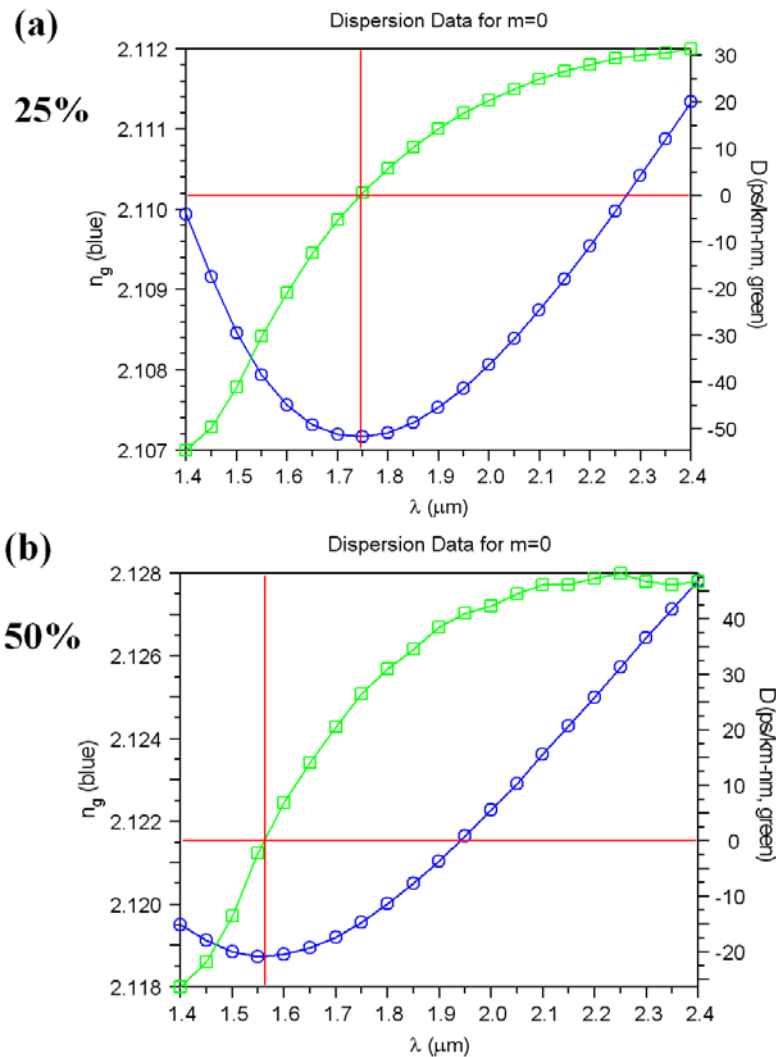
calculate the first & the second derivatives of refractive index variations giving values for group index & GVD (as given by equation 1 in section 2.1:

$$D = -\frac{\lambda}{c} \frac{d^2 n}{d\lambda^2}.$$

5) Extracting the ZDW from GVD curves:

The final step is to load all the data generated in the step 4) to Matlab to find the ZDW for each of the settings.

Figure 35 shows the GVD properties for fundamental TE mode propagation in 2-D waveguides with thickness of 2 μm and width of 1.8 μm for (a) 25% etched ridge, (b) 50% etched ridge, (c) 75% etched ridge, and (d) 100% etched ridge (i.e. rib) waveguides.



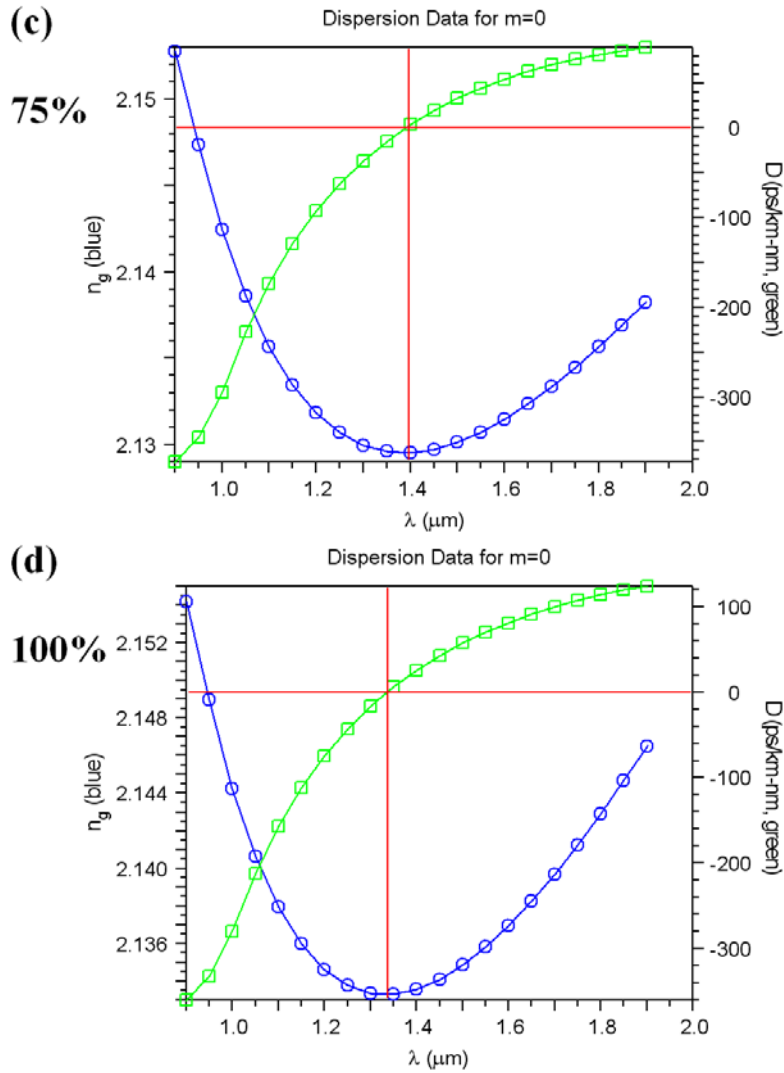


Figure 35: GVD curves of $2 \times 1.8 \mu\text{m}$ ridge waveguides with the etching profiles: (a) 25%, (b) 50%, (c) 75%, and (d) 100% (i.e. rib)

Figure 35 shows that the ZDW shifts from around $1.75 \mu\text{m}$ down to around $1.3 \mu\text{m}$ as the etch depth gets larger. The dimensions of the rib/ridge waveguides have a similar effect on the dispersion properties of the waveguide as the thickness of slab waveguides. Figures 34 and 35 show that ZDW shifts to lower values as the confinement of the light becomes better. It can be estimated from figure 34 that slab waveguides will have issues with weak confinement as the confinement in 25% etched ridge waveguide is weaker than those with higher etch depths. Figures 36-39 show size-dependence and etch profile-dependence of the ZDW for the fundamental TE mode in rib and ridge Ta_2O_5 waveguides.

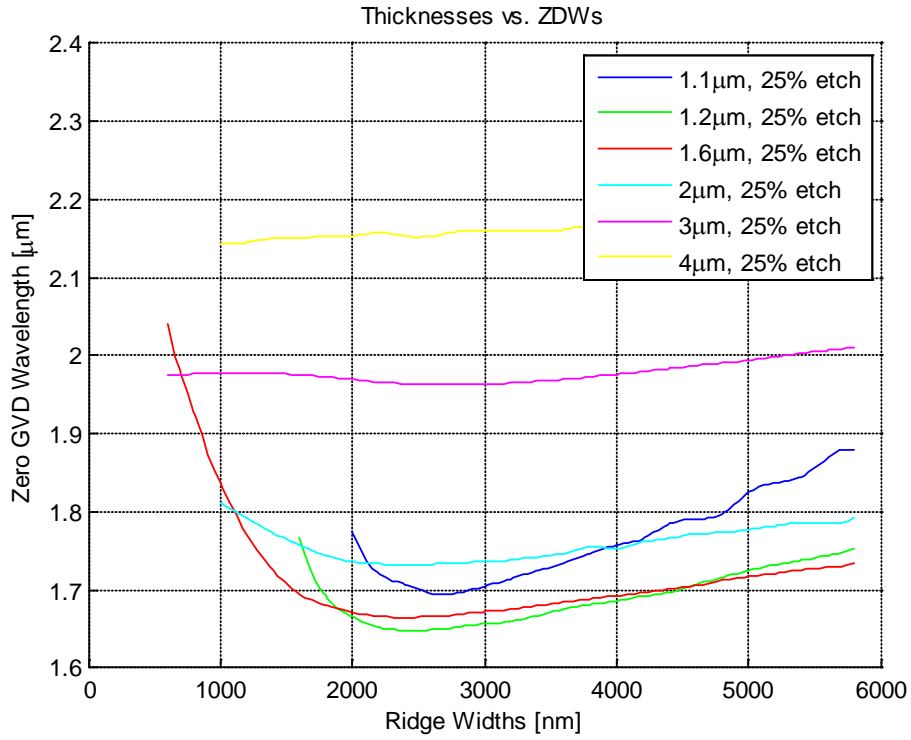


Figure 36: ZWD vs. width with respect to thickness of the 25% etched ridge waveguides

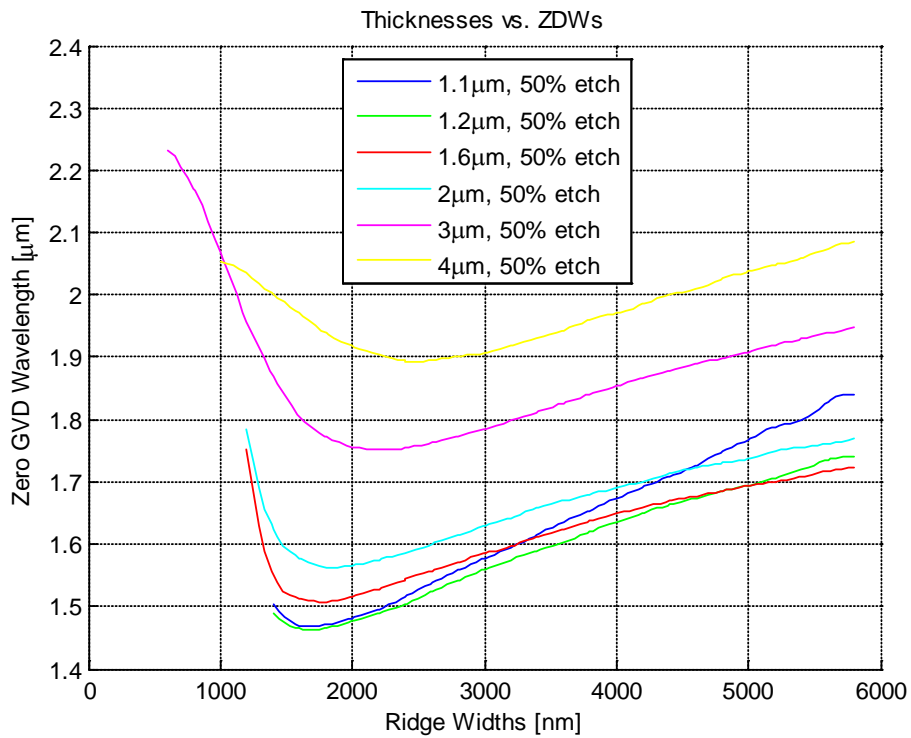


Figure 37: ZDW vs. width with respect to thickness of the 50% etched ridge waveguides

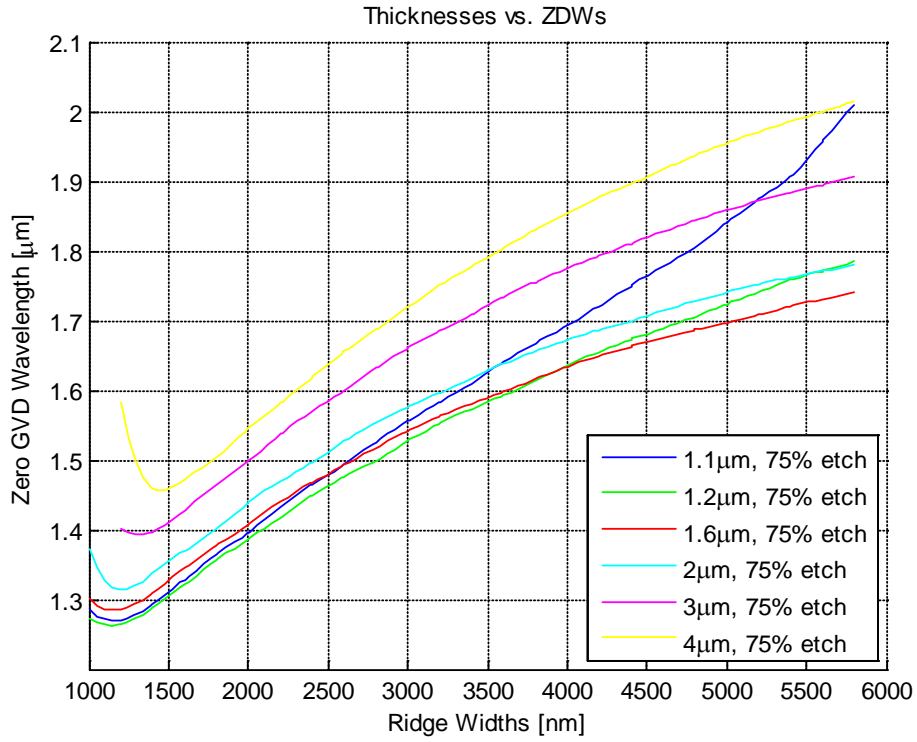


Figure 38: ZDW vs. width with respect to thickness of the 75% etched ridge waveguides

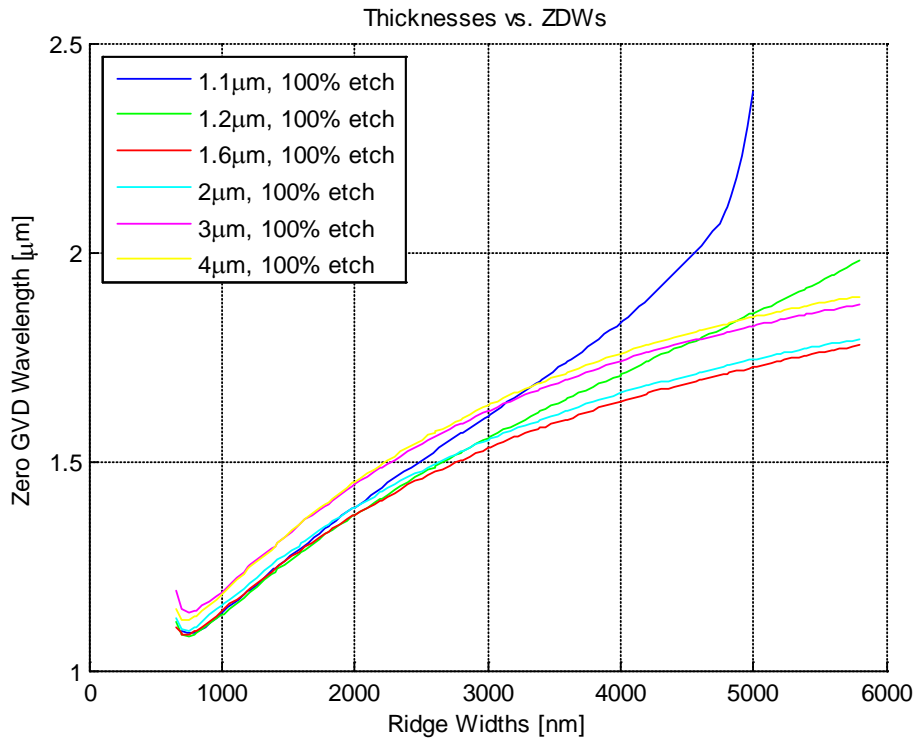


Figure 39: ZDW vs. width with respect to thickness of the 100% etched ridge waveguides (rib waveguides)

Figures 36-39 show that there is an optimum width range for the waveguide for each of the etching profiles, within which the minimum ZDW for the waveguide can be obtained, and so set the design limits for the planar waveguides. For shallow etch depth, ZDWs are greatly affected by the thicknesses of the guide for a fixed width, and ZDWs are insensitive to the width of the waveguides. For deep etching profiles, the variation in ZDWs with the thickness is not so large for the shallow etch, but ZDWs changes rapidly with changes to the width. Therefore, precise fabrication tolerance of the waveguide width is not critical for shallow etching profiles. Figure 40 shows that for the same thickness, the etch profile has great effect on the ZDW positions.

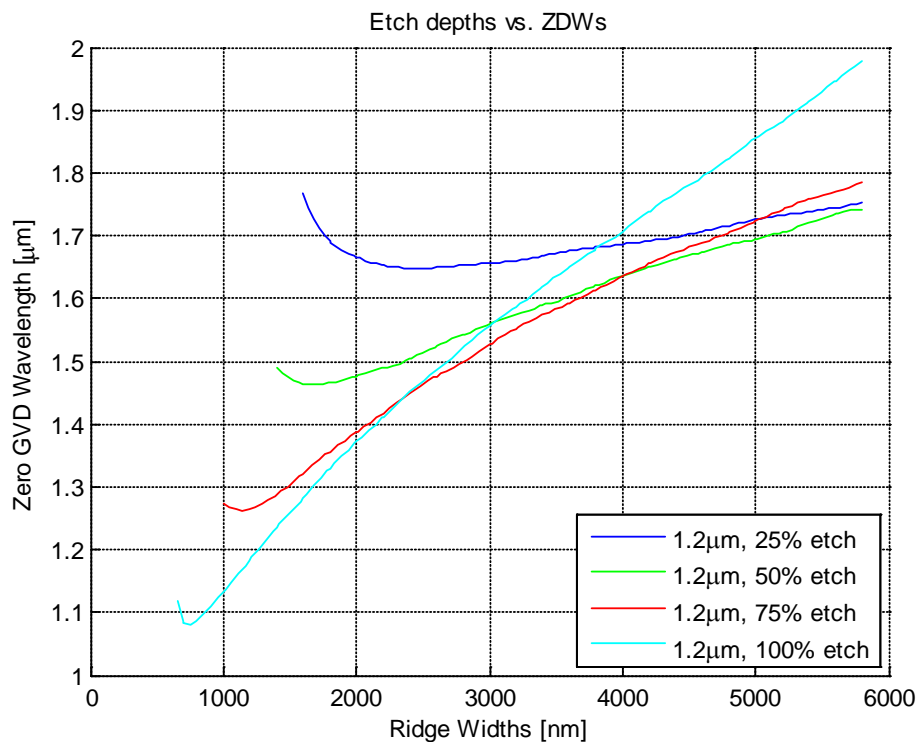


Figure 40: ZDW vs. width with respect to the etch profile of 1.2 μm thick ridge waveguides

As shown in figure 40, the rib waveguides give the best modal confinement and the lowest ZDW compared to ridge waveguides. Another interesting point is that there is a cut-off width for the waveguide in order to have a ZDW with a given thickness, and this cut-off width is larger for deep etched guides than for shallow etched guides. It is clear that mode confinement affects the dispersion properties of the waveguide significantly. There is also a minimum thickness for a waveguide in order to have a

ZDW regardless of the width. The cut-off conditions require more work in investigating the dispersion properties of the waveguide. However, the minimum ZDW obtained in the simulations is around $1.1 \mu\text{m}$ with rib dimensions of $1.2 \mu\text{m}$ thickness and around 750nm width for the TE mode. This result indicates that it is quite difficult for simple high index contrast planar waveguides to obtain a ZDW around 800nm . As suggested in the above section, highly dispersive photonic crystal structures may be etched into these 2-D waveguides to push the ZDW to around 800nm .

It is ideal if the finite difference time domain (FDTD) simulation could be performed on a planar waveguide to get information on wave propagating variations, where the building-up of nonlinear effects could be retrieved. Appendix D [68] provides a brief description of FDTD method and the advantages/disadvantages of the method. However, it is not practical for simulating a planar waveguide at centimetre-long scale using FDTD. The possible solution is to increase the nonlinear coefficient by a factor of one or more, which effectively reduced the simulation length. The outcome will not be precise but can provide a good indication on expected waveguide outputs. The simulation on photonic crystal structure is different from normal waveguide. The possible work on photonic crystal structure simulation is discussed as future works in section 7.5.

Chapter 4 Nonlinear Susceptibility of Planar Waveguides

The nonlinear susceptibilities are known to be useful in studying the physical properties of dielectrics [69]. Tantalum pentoxide (Ta_2O_5) planar waveguides have recently been shown to possess unusually large third order nonlinear susceptibilities ($\chi^{(3)}$ or ‘Chi 3’) and nonlinear Kerr coefficient (n_2) [65], leading to potential applications in nonlinear integrated optics [70-74], e.g. on-chip tunable lasers. This chapter shows the experimental observation of the third-harmonic generation (THG), and derived $\chi^{(3)}$ based on experimental results in Ta_2O_5 based planar waveguides over a wavelength range of 1470 – 1610 nm.

4.1 Third-Harmonic Generation and Measurement of Chi 3

A number of techniques for measuring $\chi^{(3)}$ of materials have been developed. These include:

- 1) Self-phase modulation (SPM) [65], which is based on femtosecond time-of-flight measurements and measurement of intensity induced spectral change, to determine the value of the nonlinear coefficient in the material.
- 2) Four-wave mixing (FWM) [17, 75-77]. This is one of the most commonly used methods for measurement of $\chi^{(3)}$, and is done by measuring either: the

intensity induced refractive index change, two-photon absorption coefficient, or the time resolved beam intensities of degenerate FWM (DFWM).

- 3) Third harmonic generation (THG) [78-80]. Previous experiments have measured the intensity/polarization fields of the THG of various samples (mainly single crystal structures) to obtain $\chi^{(3)}$ values, but require use of a fused silica samples with the same design as the test sample.
- 4) Z-scan technique [81]. This technique is good for getting both real and imagery part of $\chi^{(3)}$ of the material by using frequencies close to the surface plasmon resonance (SPR) to examine the film structures. In this method, a sample is translated longitudinally through the beam-waist region of a focused Gaussian laser beam, and the variation of the on-axis intensity in the far field is measured as a function of sample position. The variation of measured power is proportional to the nonlinear phase shift. With sample thickness and laser intensity at the sample together, n_2 of the sample could be determined from the phase shift.

Among these various methods, THG measurement is one of the simplest possible methods for obtaining $\chi^{(3)}$ as it is a purely electronic and coherent process, with no ambiguity in the mechanism in high contrast to other processes such as degenerate four-wave mixing and optical Kerr effect [80], where other competing nonlinear effects are more complex in terms of experiment setup or analysis.

THG effect has been demonstrated in many bulk crystalline materials, such as BIBO (Bismuth triborate, BiB_3O_6) [82], thin sapphire crystals [83], fused silica [84], carbon nanotubes [85], and other types of single crystals [86], but not Ta_2O_5 . In this section, an experimental setup and measurement method which is independent of other competing nonlinear effects (such as SPM, Raman effects, and FWM (including DFWM)) is presented. The results obtained also allow the calculation of $\chi^{(3)}$ without a reference material (e.g. fused silica).

4.1.1 Planar Waveguide Samples

Identical sets of Ta_2O_5 waveguides were grown on a silicon substrate by RF (radio frequency) sputtering, optical lithography, and plasma etching [87]. Ta_2O_5 is deposited on SiO_2 buffer layer on top of a silicon substrate. The Ta_2O_5 layer is then etched into rib structures before another layer of SiO_2 is deposited on top of the ribs. Inset to figure 41 shows the cross-sectional SEM (scanning electron microscope) image view of one waveguide. Robustness tests have previously shown that there is no change in waveguide loss or UV induced damage with 1 W of CW 455 nm light focused into the guide, or waveguide facet damage for 800 nm 150 fs pulses with energies up to $2 \mu J$ from a 250 kHz Ti:Sapphire regenerative amplifier [1, 12]. Before commencing this new analysis of nonlinear effects in the guides, further tests for laser induced damage were performed on a test guide with the same geometry parameters (on a different waveguide set from the same wafer). This showed that there was no damage for 150 fs pulses with energies up to $12 nJ$ (3 mW average power) over the entire 900 – 1650 nm tuning range of Coherent optical parametric amplifier (OPA).

4.1.2 Experiment Setup

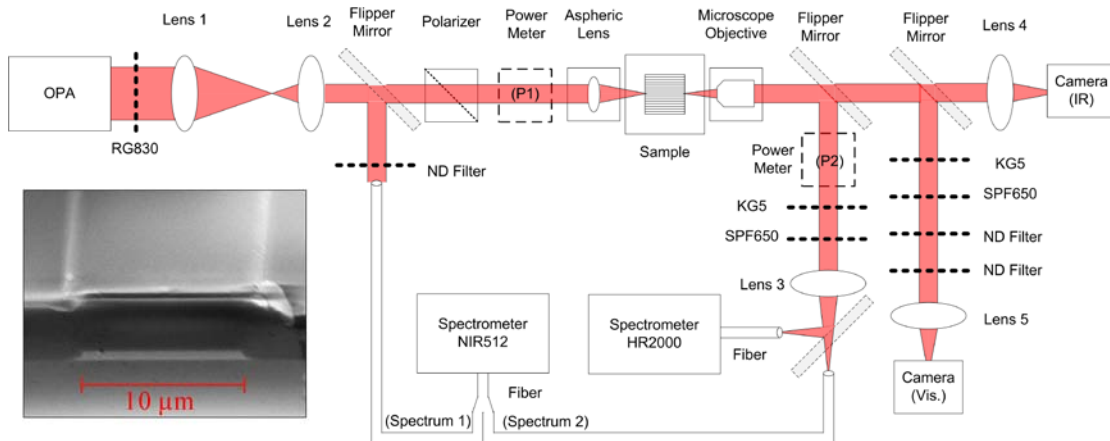


Figure 41: Experimental setup for the third-order nonlinear susceptibility (inset: SEM image of cross-sectional view)

Figure 41 shows the experiment setup for $\chi^{(3)}$ measurement with cross-sectional view SEM image and refractive index profile of the waveguide. The fundamental

pump beam is provided by an OPA (Coherent OPA9400) pumped by a mode-locked ultrafast Ti-Sapphire amplifier (Coherent Vitesse DUO + REGA). The OPA provides tunable infra-red (IR) pulses (150 fs duration) over range 900 to 1600 nm (limited by the detection equipment). A telescope is used to reduce the pump spot size for improved coupling to the guides. A linear polarizer is used as a power attenuator allowing input power to be adjusted without introducing significant distortions into the beam or affecting the coupling conditions. A short focal length lens (providing near transform limited spot) is used for input coupling to the guides and output is collected and collimated by a 10X microscope objective. The IR outputs are then fibre coupled to an IR spectrometer (Ocean Optics NIR512). A Schott KG5 glass filter and a 650 nm short-pass filter are used to remove the residual pump before fibre coupling to a visible spectrometer (Ocean Optics HR2000). Additional lenses and removable beam splitters image the waveguide output facet onto visible and IR CCD cameras placed after the microscope objective. Images from these cameras are used for optimizing pump input coupling and identifying the mode number of coupled pump and generated THG modes.

4.1.3 Third-Harmonic Generation (THG) Results

Silicon dioxide (SiO_2) clad Ta_2O_5 planar rib waveguides with a core thickness of 750 nm, and widths $2.5 \mu m$ (g5) and $18 \mu m$ (g36) were analyzed. The pump was tuned over the wavelength range 1470 nm – 1610 nm, and spectral measurements made at average pump powers over the range 0.5 mW – 2.0 mW (measured by a power meter placed between polarizer and coupling optics). Frequency tripling was observed over the wavelength range 489 nm – 538 nm. Figure 42 shows an example of the IR pulse spectrum and its corresponding THG output.

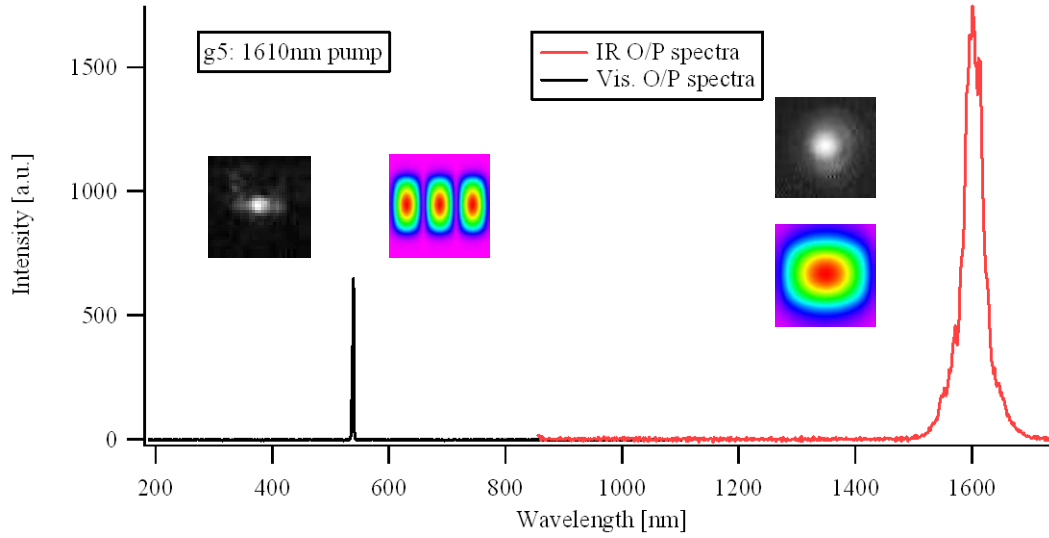


Figure 42: Output spectrum of IR and the corresponding generated THG at 2 mW pump power (insets are mode images from experiment and simulated mode profiles of IR and visible output modes, respectively)

4.2 Calculation of Third-Order Susceptibility

The relationship between $\chi^{(3)}$ and n_2 in solid semiconductors described in the work of Mohanta and Choudhury [17] is used to compare the values of the experimental results and the first reported measurement of the nonlinear coefficient (n_2) on the Ta_2O_5 planar waveguides made by Tai *et al.* [65] based on measurement of self-phase modulation at a fixed wavelength of 800 nm. In order to measure $\chi^{(3)}$ of the material, the following mathematical relations linking the intensities and $\chi^{(3)}$ can be used:

Under the simplified phase matching condition, the electric fields of second harmonic generation (SHG) and a pump propagation along the z-direction is given by [88]:

$$\frac{d}{dz} E(z, 2\omega) = i\kappa e^{-i\Delta k \cdot z} \cdot E^2(z, \omega) \quad (17)$$

where $\kappa = \frac{\omega d_{eff}}{n_0 c}$, $d_{eff} = \varepsilon_0 \cdot \chi^{(2)}$, $\Delta k = k(2\omega) - 2k(\omega)$ is the wave number difference

(i.e. the phase-mismatch), $k = \frac{2\pi}{\lambda_{wg}} = \frac{2\pi}{\lambda_{pump} / n_0} = \frac{2\pi \cdot n_0}{\lambda_{pump}}$ is the wave number inside

the waveguide. Hence,

$$|E(2\omega)|^2 = \left(\frac{\omega d_{eff}}{n_0 c} \right)^2 \cdot |E(\omega)|^4 \cdot \frac{1}{\Delta k^2} \quad (18)$$

Applying the same phase-matching condition for THG, the electric fields must satisfy the relations:

$$|E(3\omega)|^2 = \left(\frac{\omega d_{eff}}{n_0 c} \right)^2 \cdot |E(\omega)|^6 \cdot \frac{1}{\Delta k^2} \quad (19)$$

where in this case, $d_{eff} = \chi^{(3)}$ for the third harmonic generation [19]. The intensity per unit area is given by:

$$\frac{|Power|^2}{Area} = I = \frac{cn_0 \varepsilon_0}{2} E \cdot E^* = \frac{cn_0 \varepsilon_0}{2} |E|^2 \quad (20)$$

$$I(3\omega) = \frac{4\omega^2}{(cn_0)^4 \cdot \Delta k^2 \cdot \varepsilon_0^2} \cdot |\chi^{(3)}|^2 \cdot I(\omega)^3 \quad (21)$$

This is the simplified phase-matching condition for equation 14 given in section 2.2.7:

$$I(3\omega) = \frac{\omega^2}{(cn_0)^4 \cdot \varepsilon_0^2} \cdot |\chi^{(3)}|^2 \cdot I(\omega)^3 \cdot l^2 \cdot \left[\frac{\sin(\Delta k \cdot l / 2)}{(\Delta k \cdot l / 2)} \right]^2, \text{ where } n_0 = n_{eff}, \omega = \frac{2\pi \cdot c}{\lambda_{pump}},$$

$\Delta k = k(3\omega) - 3k(\omega)$. Therefore,

$$|\chi^{(3)}| = \sqrt{I(3\omega) \cdot \frac{(cn_0)^4 \cdot \Delta k^2 \cdot \varepsilon_0^2}{4\omega^2 \cdot I(\omega)^3}} \quad (22)$$

The relationship between $\chi^{(3)}$ and n_2 is described in section 2.2.2. Values required for calculating $\chi^{(3)}$ from equation 21 are: intensities of the coupled fundamental pump mode at the beginning the waveguides, intensity of the generated THG (measured at the output of the waveguide), cross-sectional area of the coupled pump

mode, wave numbers (k-vectors) for coupled fundamental pump mode and generated THG modes.

The effective mode indices, mode spot size (1/e widths), and wave vectors (k) at the test wavelengths are determined from finite element analysis utilizing RSoft CAD Suite software, taking into account material dispersion [62, 63]. The numerical accuracy of the simulation solutions was set to the 10th digit, providing more than sufficient accuracy for this analysis. Figures 43 and 44 show the refractive indices and the corresponding wave number difference (Δk) of two waveguides, g5 and g36, respectively. Inset to figure 44 shows that the modes used in simulations are verified by the mode images obtained from experiments.

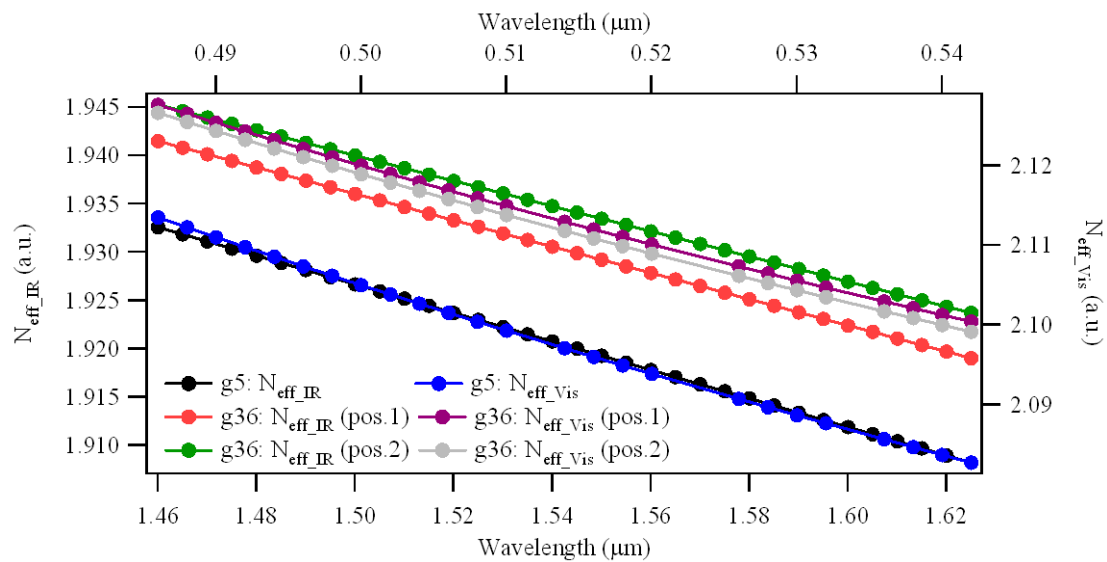


Figure 43: Refractive indices of the waveguides at corresponding wavelengths from Simulation

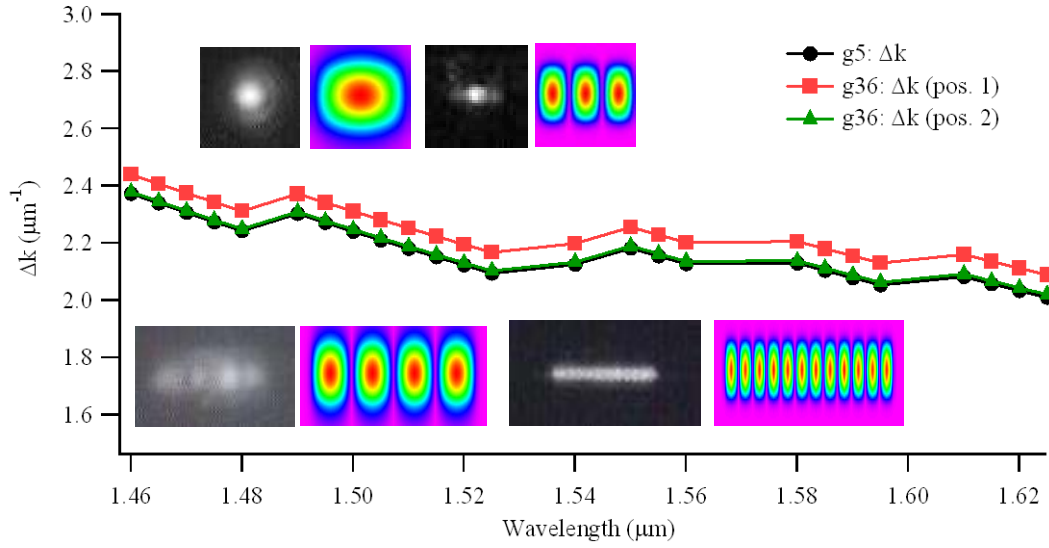


Figure 44: Wave number differences of the waveguides (Insets: mode images and mode profiles from experiment and simulation, respectively)

To determine the true output intensity of the THG beam from the fibre coupled spectrometer measurements, the spectrometer is calibrated to take into account efficiency of collection of light by the fibre in the back focal plane of the output objective. This is done by directing a CW He-Ne laser onto a 10 μm pin hole. Then light emerging from the rear of the pin hole was collected using exactly the same objective arrangement as for the THG experiments. The integrated area of the spectrum (measured on the spectrometer) is then normalized with a reading from a power meter (placed in the same position behind the objective, see P2 in Fig. 41). In this arrangement, the pin hole effectively mimics the diffractive properties of the waveguide, however, there are no further ambiguities/inaccuracies introduced by the presence of nonlinear effects or loss in the guide. As the spectrometer is pre-calibrated for all wavelengths, a single wavelength calibration measurement is sufficient for all further measurements. As shown in figure 44, the wave number difference (Δk) does not change when the pump is coupled into different waveguides. This is a clear indication of self-selective process inside the waveguides, which always finds the same phase matching condition, i.e. the same Δk , when the width of waveguide changes.

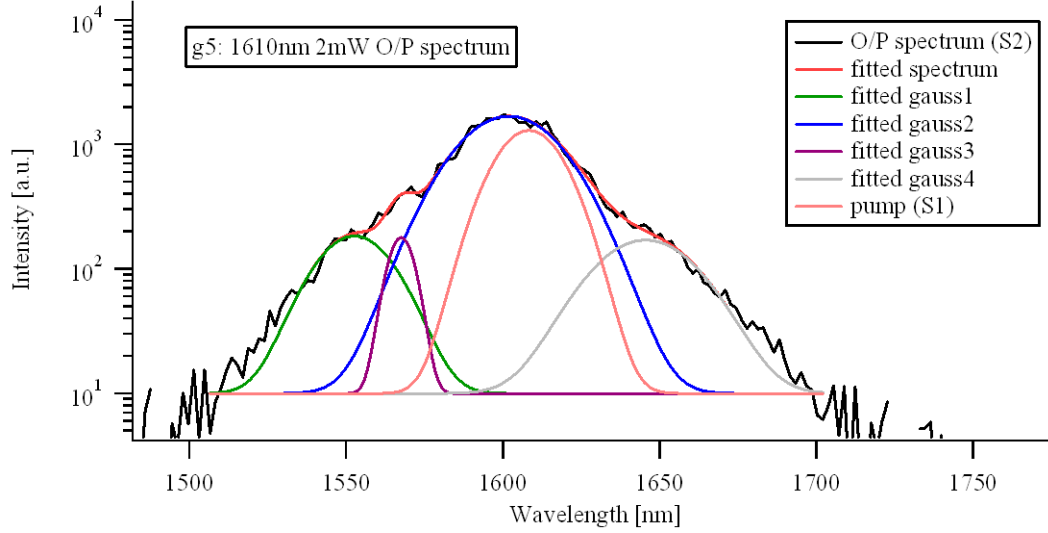


Figure 45: Spectral fitting for IR output shown in figure 42

Figure 45 shows features of the original and broadened pump beam of the IR side in figure 42 in more detail. The superimposed curves show component Gaussian waves, matched by curve fitting techniques. In this figure, we see that the pump has been significantly broadened. This is due to a combination of self-phase modulation and four-wave mixing. In order to calculate the $\chi^{(3)}$ value precisely, independent from these effects, the fundamental pump (at the waveguide input facet) has to be separated from the broadened spectral data (measured behind the objective at the output facet). This is done by normalizing the intensities of both the input spectrum taken by the IR spectrometer before the input coupling S_1 (Spectrum 1 in Fig. 41) and the output spectra S_2 (Spectrum 2 in Fig. 41) to the same level. The integrated areas of the respective spectra at each input power are then calculated, i.e. A_1 and A_2 are the integrated areas of S_1 and S_2 shown in Fig. 42, respectively.

$$A_1 = \int S_1(\lambda) d\lambda \text{ (after normalization)} \quad (23)$$

$$A_2 = \int S_2(\lambda) d\lambda \text{ (after normalization)} \quad (24)$$

The ratio of A_1 and A_2 ($R = \frac{A_1}{A_2}$) indicates how much power is responsible for the

THG (P_{THG}) from the real readings (P_2 in Fig. 41) of the power meter placed behind the objective (output coupling losses can be assumed to be negligible):

$$P_{THG} = \frac{A_1}{A_2} P_2 \quad (25)$$

Figure 45 also shows that there are several other nonlinear effects occurring inside the waveguide simultaneously at a pulse energy of 8 nJ (equivalent to 2 mW average power) for 150 fs pulses at 1610 nm. The fitted Gaussian curves 2 & 3 indicate the existence of SPM and fitted Gaussian curves 1 & 4 indicate FWM (since they show similar peak intensities, bandwidths, and central symmetrically placed either side of the pump wavelength). As the beam above 1650 nm is truncated by the cut off in sensitivity of the spectrometer, the overall spectrum could in fact be broadened well over 100 nm (compared to the pump pulse), which indicates that it is possible use these waveguides to produce supercontinuum (SC). Further design and optimization will be required for producing low power, low cost SC sources using the Ta_2O_5 based waveguides. The objective of this exercise is to determine the design limits for this.

In order to remove ambiguities associated with waveguide input coupling efficiency, the actual coupled pump power at the start of the waveguide was determined using known waveguide loss values to scale the obtained output power values from the output (P_{THG}). The relative waveguide loss was measured to be -8.5 dB in average (with 10% error) using the cutback method on identical waveguide samples from the same wafer.

4.2.1 Chi 3 Calculations

Although by inserting the appropriate measured experimental and theoretically derived parameters into equation 21, the $\chi^{(3)}$ values of Ta_2O_5 planar waveguides could be obtained, the following considerations need to be taken into account before calculating $\chi^{(3)}$ values:

- 1) The analysis must be performed under simplified, near perfect phase matching condition (otherwise the value of THG intensity will be an underestimate). In reality, the phase matching assumption is unlikely, in which case the derived $\chi^{(3)}$ value will be underestimated. In this case, the phase matching can be assumed to be optimal by tuning the pump laser wavelength to obtain

maximum intensity of the THG beam (maximum THG beam amplitude will only be achieved under optimal phase-matching condition).

- 2) Figure 45 shows that the pump beam is broadened considerably during its transit along the guide, generating side peaks due to four-wave mixing. Therefore, it is necessary to make sure that only the fundamental mode of the incident pump beam contributes to the generation of THG (i.e. the side peaks induced in the broadened pump beam by four-wave mixing do not cause THG themselves). This can be ensured by performing the analysis only up to a maximum power level where the THG beam is a clean single peak.
- 3) Output coupling is assumed to be perfect because the microscope objective is quite close to the output facet, i.e. all the output light is well coupled into the objective. As all optical components are AR (anti-reflection) coated specifically for IR wavelengths, there will be a small error in the calculations of the visible powers due to coupling loss in the output collection. The waveguide losses have 10% error as indicated from previous measurements. These two factors could introduce up to $\approx \pm 0.71 \times 10^{-13}$ esu to $\chi^{(3)}$ calculations, which lead to $\approx \pm 1.02 \times 10^{-19} \text{ m}^2 / \text{W}$ variation of the nonlinear Kerr coefficient (n_2).
- 4) Assume (as measured previously) the loss of narrow guide (g5) is -8.5 dB and wide guide (g36) is -7.5 dB.

For improved accuracy, the full analysis was performed at a range of discrete pump power levels (0.5 – 2 mW average power with steps of 0.5 mW). This reveals the evolution of spectral broadening of the pump beam, and introduction of contributing nonlinear effects. Table 1 shows the calculated average nonlinear coefficients for each pump wavelength used in the corresponding waveguide.

Table 1: Calculated average nonlinear coefficients for each pump wavelength

	Input λ (nm)	Output λ (nm)	$\chi^{(3)} \times 10^{-13}$ (esu)	
			1.5 (mW)	2.0 (mW)
g5	1470	489	0.98 ± 0.21	1.42 ± 0.21
	1500	500	0.80 ± 0.23	1.02 ± 0.23
	1550	516	2.13 ± 0.57	1.87 ± 0.57
	1610	538	4.75 ± 1.58	5.74 ± 1.58
g36	1495	497	0.77 ± 0.21	0.96 ± 0.21
	1555	522	3.09 ± 0.90	4.75 ± 0.90
	1610	536	3.16 ± 1.26	6.00 ± 1.26

The average value for $\chi^{(3)}$ over the wavelength range 1470 to 1610 nm is: $\chi^{(3)} \approx (2.67 \pm 0.71) \times 10^{-13}$ esu. Hence, the average value of the nonlinear Kerr coefficient is: $n_2 \approx (3.77 \pm 1.02) \times 10^{-19} (m^2/W) = (3.77 \pm 1.02) \times 10^{-15} cm^2/W$. This value is in agreement with previously measured value from SPM analysis [65]. It also shows that the value of nonlinear susceptibility of Ta_2O_5 is, as expected, in between the BK7 silica glasses ($\chi^{(3)} \approx 2.0 \times 10^{-14}$ esu) and titanium dioxides (TiO_2) ($\chi^{(3)} \approx 1.5 \times 10^{-12}$ esu) [4].

4.3 Chi 3 Dispersion of Tantalum Pentoxide

$\chi^{(3)}$ dispersion has been studied in material systems such as poly(dihexylsilane) (PDHS) films [89], molecules [90], and TeO_2 glass films [91] by analyzing the Kramers-Kronig dispersion relations, absorption spectrum, and THG respectively. In this experiment, the measurement of $\chi^{(3)}$ covers a range of frequencies from 1470 – 1610 nm enabling us to obtain the $\chi^{(3)}$ dispersion values for the Ta_2O_5 material system.

The advantage of this measurement method is the use of THG output, which is only dependent on $\chi^{(3)}$ of the material. By analyzing the spectra and normalizing the

fundamental pump contribution at the output, $\chi^{(3)}$ can be calculated precisely without any trouble in identifying complex effects occurring in the IR regime, such as FWM and SPM. The multi-wavelength analysis also reveals a trend for the $\chi^{(3)}$ value of Ta_2O_5 to increase as the wavelength becomes longer as shown in Figure 46.

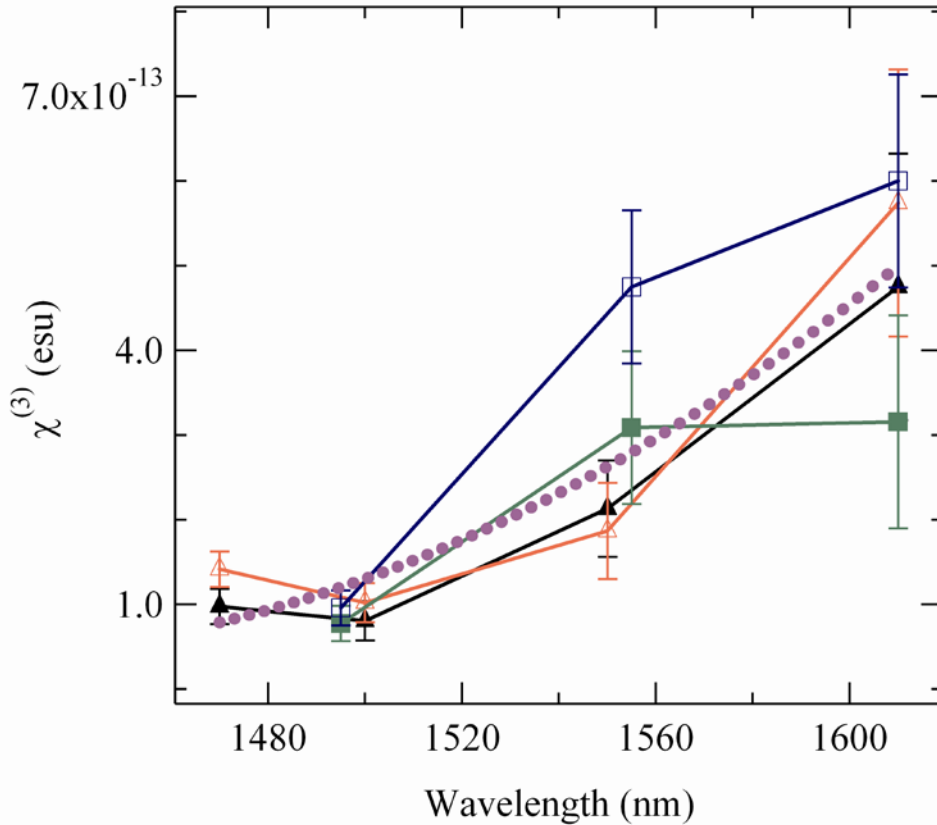


Figure 46: Calculated third-order nonlinear susceptibility of tantalum pentoxide waveguide samples. Sample A: solid triangle (black) for 1.5 mW and open triangle (red) for 2 mW pump power; Sample B: solid square (green) for 1.5 mW and open square (blue) for 2 mW pump power. Purple dotted line indicates the trend of third-order nonlinear susceptibility changes with wavelength

This multi-wavelength analysis also allows analysis of $\chi^{(3)}$ dispersion properties, revealing a trend for the $\chi^{(3)}$ value of Ta_2O_5 to increase as the wavelength becomes longer (shown in figure 46). The increase of the $\chi^{(3)}$ value can only be caused by one-, two-, or three-photon resonance [4]. According to the studies of electronic structure of Ta_2O_5 by Arranz *et al.* [92], the constant initial-state curves (See Fig. 47)

show multiple resonance maxima that are explained in terms of the Ta $5p \rightarrow 5d$, $5p \rightarrow 6sp$, and $4f \rightarrow 5d$ photoabsorption mechanisms, the spin-orbit splitting of the Ta $5p$ and Ta $4f$ core levels, and splitting of the Ta $5d$ final states by crystal-field interactions. Therefore, the projected wavelength for obtain a resonance peak of $\chi^{(3)}$ is around 1800 nm (See Fig. 48), which corresponds to a band energy of 2.07 eV. This energy level is only possible for three-photon resonance of the $4f_{7/2} \rightarrow 5d(t_{2g})$, $4f_{5/2} \rightarrow 5d(t_{2g})$, $5p_{3/2} \rightarrow 5d(t_{2g})$, or $5p_{1/2} \rightarrow 5d(t_{2g})$ transitions.

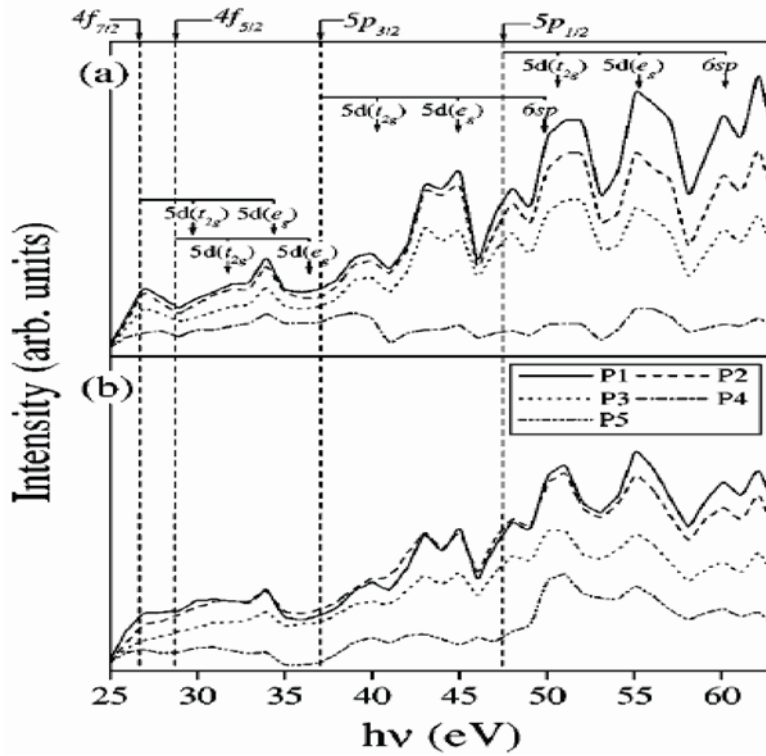


Figure 47: Constant-initial-state curves obtained from measured spectra corresponding to P1, P2, P3, P4, and P5 features of the valence band, for (a) stoichiometric and (b) reduced tantalum pentoxide [92]

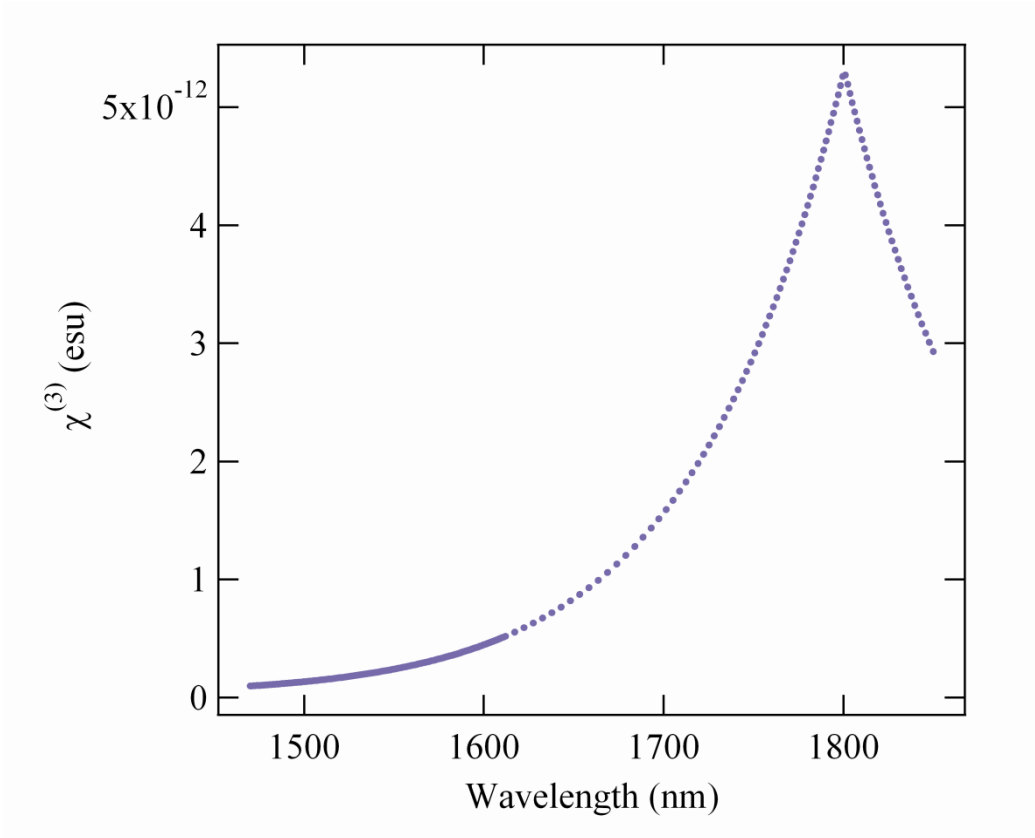


Figure 48: Estimated (dashed line) three-photon resonance peak of third-order nonlinear susceptibility of Ta_2O_5 based on experimental results (solid line)

4.4 Summary

The frequency tripling effect, i.e. THG, in Ta_2O_5 planar waveguides has been demonstrated experimentally in this chapter. Experiments show that THG can be generated over a relatively broad bandwidth (~ 140 nm) in the waveguide samples, which is within the frequency range for observing THG from other nonlinear materials such as TeO_2 . The theory for calculating the third order susceptibility of the material based on the third harmonic generation (THG) measurements has been developed. The nonlinear coefficient of Ta_2O_5 planar waveguides is derived from multi-wavelength analysis of THG outputs. Values over the wavelength range 1470 to 1610 nm are determined to be between $(0.98 \pm 0.21) \times 10^{-13}$ to $(6.00 \pm 1.26) \times 10^{-13}$ esu with an average value of $(2.67 \pm 0.71) \times 10^{-13}$ esu.

Although currently applied to measurement of $\chi^{(3)}$, the same experimental setup is equally applicable to measurement of the second order susceptibility ($\chi^{(2)}$) in any other optical guides based on other type of materials by measuring output spectra and analyzing the spectral changes within output spectra which could be the results from one or more nonlinear effects, such as sum-difference frequency generation, SPM, XPM, FWM, and etc.

This technique is suitable for studying and further understanding nonlinear effects in Ta_2O_5 and planar waveguides based on other materials. The values of nonlinear coefficients and good optical properties of the waveguides also provides opportunities for developing and optimizing the designs for other potential applications using Ta_2O_5 waveguides, for example, low input power supercontinuum (SC) source with wide spectral range and low spectral noise.

Chapter 5 Experimental Results of Supercontinuum Generation

Chapter 4 focused on examination of THG generation and calculation of the third-order susceptibility of the waveguides from the THG beam data. This chapter extends the experimental analysis to examine the behaviour, relative contributions, and interplay between nonlinear processes which contribute to SC generation in the guides, as a function of pump power and wavelength with respect to calculated dispersive properties of the guides.

As described earlier in chapter 2, the SC generation is a result from several combined linear and nonlinear effects. The most notable effects are: dispersion, SPM, XPM, and FWM. Dispersion of waveguide is determined by the material and waveguide dimensions. SPM and XPM are results from nonlinear Kerr effect, due to high intensity laser induced nonlinear refractive index change. SPM induced spectral changes are described by equation 8: $\delta\omega_{\max} \approx n_2 I_0 \frac{\omega_0}{c} L \frac{1}{\tau_0}$, in section 2.2.2. The

spectral changes in XPM are given by equations 10 and 11 in section 2.2.5. XPM also allows energy transfer between two different frequency components as mentioned. The FWM is the critical effect that responsible of creating new frequency components within the femtoseconds pulses. The general intensity relationship between input and output pulses, neglecting the pump depletion, is given by equation 14:

$$I_4 = \text{const} \cdot |\chi^{(3)}|^2 \cdot I_1 \cdot I_2 \cdot I_3 \cdot l^2 \cdot \left[\frac{\sin(\Delta k \cdot l/2)}{\Delta k \cdot l/2} \right]^2, \text{ in section 2.2.6.}$$

5.1 Supercontinuum (SC) Output Spectra

The SC output spectra for the same guides as examined in chapter 4, i.e. g5 (2.5 μm wide, 0.75 μm high) and g36 (18 μm wide, 0.75 μm high) were characterized for pump wavelengths over the range 1000 – 1610 nm and the effect of pump power and wavelength on spectral broadening is investigated for average powers up to 3 mW (experiments performed in 0.5 mW steps) to allow identification of the primary nonlinear effects contributing to the SC. Full experimental spectra are presented in Appendix E. Key results are described below.

A maximum pulse broadening of nearly 200 nm was obtained for a 2.5 μm wide guide (g5) under 2 mW pump power (8 nJ per pulse, or peak pulse power of 32 kW) at a wavelength of 1195 nm. The analysis of SC spectra for the two guides at specific pump wavelengths of ~1200 nm and ~1600 nm via Gaussian curve fitting is presented.

5.1.1 Output Spectra at ~1200 nm

Figures 49(a)-51(a) show the output spectra for two waveguides under different pump conditions for a pump wavelength of 1200 nm, which demonstrate the evolution of the output spectra with respect to pump power. Figures 49(b)-51(b) and 49(c)-51(c) show Gaussian curve fittings to the output spectra from each waveguide for several different pump powers (1.5 mW for g5, 1 mW for g36, and highest used power for both). For the wider guide (g36), the affect of pump position on SC evolution was also investigated as pump position relates to the excited pump mode number. Hence there are two sets of data for this guide. This curve fitting approach allows the spectra to be systematically de-convolved to derive the constituent frequency components.

The results show that the pulses start to become broadened at a low average power level of 0.5 mW for the narrow waveguide (g5), and broaden to bandwidths up to nearly 200 nm for 2 mW average pump power without changing the mode coupling or damaging the waveguide facet. For a wider waveguide (g36), pulses require average power to be above about 2 mW to start the broadening process, and the damage

threshold for waveguide facets are determined to be at $5 \times 10^8 \text{ GW} / \text{m}^2$ providing the focus is exactly on waveguide facet (equivalent to $\sim 60 \text{ mW}$ for guide g5 and $\sim 400 \text{ mW}$ for guide g36 in this case). The corresponding output spectra requires up to 7 Gaussian pulses to fit, with side peaks generated on the longer wavelength or both sides of the fundamental pump output wavelength. Table 2 shows the fitting parameters for each Gaussian peak contributing to the output spectra for each of the two waveguides at the highest pump power.

A non-symmetrical spectrum is observed even at 0.5 mW pump power (fig. 49) with broadening of the fundamental on the long wavelength side. This is the characteristic signature of SPM (see Equ. 8 of section 2.2.2). As power increases more, (1.5 mW) XPM occurs between the FWM side peak pairs G3 & G4 (fig. 49c) and G2 & G5 (fig. 49c). Increasing power further (2 mW) causes the SPM to broaden the side peaks further (width of the Gaussian curve fits increases). In addition, FWM occurs spontaneously creating symmetrical peaks about the fundamental, but with centre wavelength spaced further (in wavelength) from the fundamental.

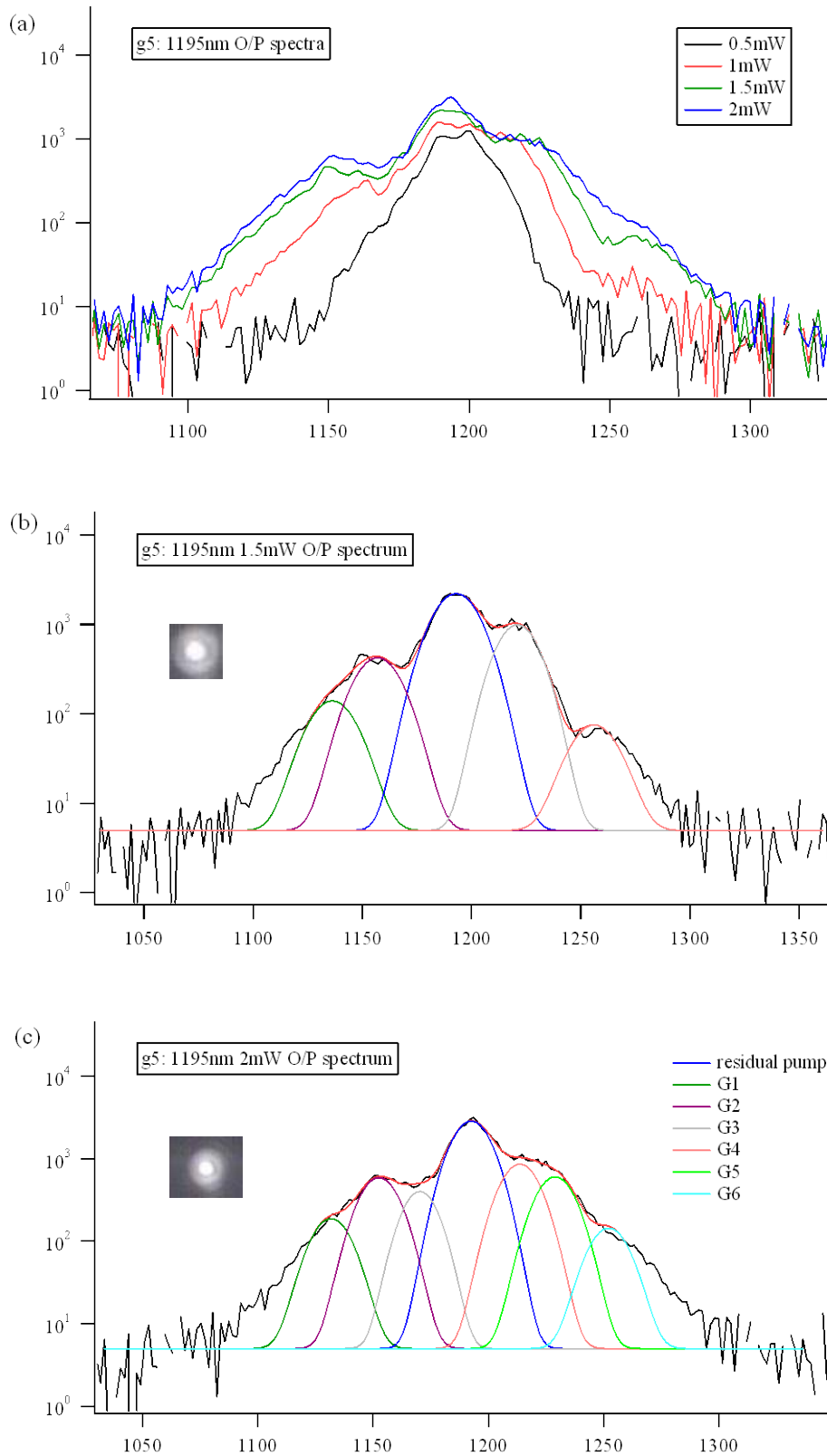


Figure 49: Output Spectra of g5 at 1195 nm: (a) at different average power levels (b) spectral fitting for 1.5 mW output (Inset: mode profile image) (c) spectral fitting for 2 mW output (Inset: mode profile image)

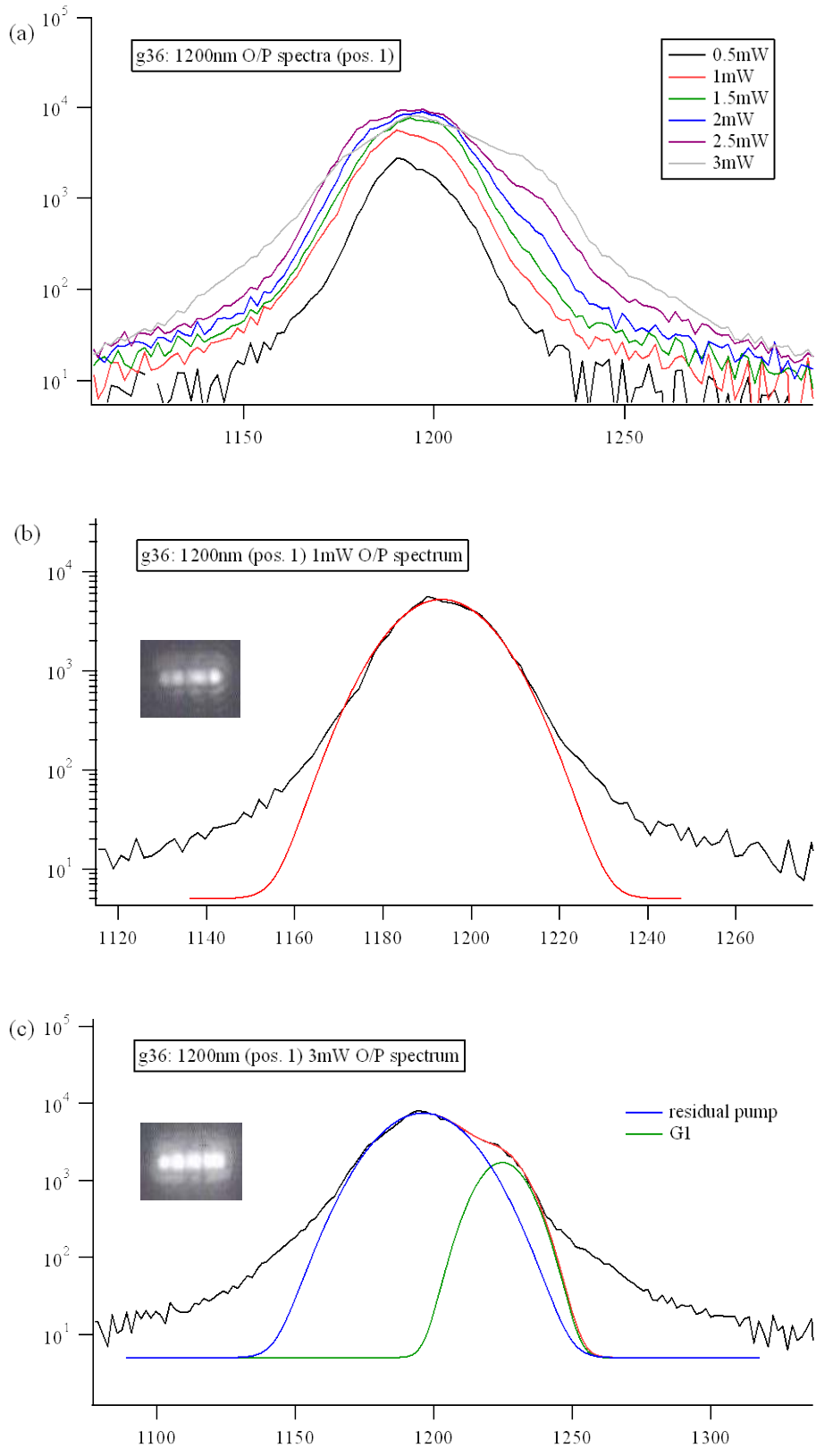


Figure 50: Output Spectra of g36 coupling position 1 at 1200 nm: (a) at different average power levels (b) spectral fitting for 1 mW output (Inset: mode profile image) (c) spectral fitting for 3 mW output (Inset: mode profile image)

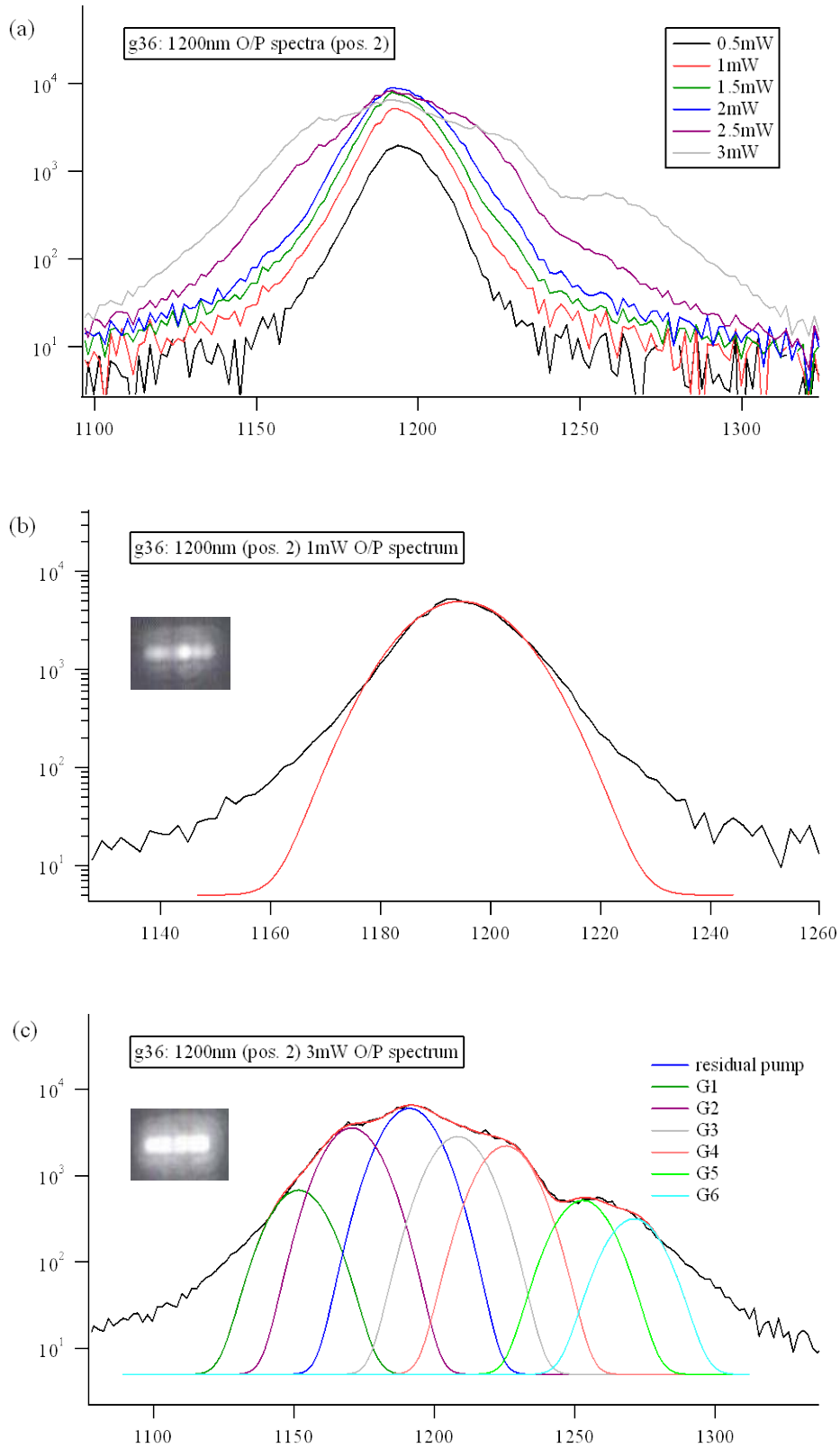


Figure 51: Output Spectra of g36 coupling position 2 at 1200 nm: (a) at different average power levels (b) spectral fitting for 1 mW output (Inset: mode profile image) (c) spectral fitting for 3 mW output (Inset: mode profile image)

Table 2: Fitting parameters of output spectra at pump wavelength of ~1200nm

λ_{pump} (nm)	P_{pump} (mW)	Guide	Fitting curve	Amplitude	Relative power (integrated area)	Peak position (nm)	Width (nm)	Position difference (with offset) (nm)
1195	2	g5	Residual pump	2878.72	57708.7	1192.58	11.2147	0
			G1	183.468	4095.61	1131.82	11.2147	-60.76
			G2	589.118	12181.8	1152.62	11.2148	-39.96
			G3	398.869	7547.93	1170.34	10.0847	-22.24
			G4	862.3	17612.1	1213.63	11.2148	21.05
			G5	601.93	12428.7	1228.95	11.2146	36.37
			G6	139.795	3227.54	1252.13	11.2149	59.55
1200	3	g36 (pos. 1)	Residual pump	7473.54	256399	1196.2	19.292	0
			G1	1708.34	34725.9	1224.72	11.3115	28.52
		g36 (pos. 2)	Residual pump	5970.99	127552	1191.11	12.0019	0
			G1	671.577	14790	1151.66	12.0019	-39.45
			G2	3550.67	76058.1	1170.56	12.0036	-20.55
			G3	2821.17	60536	1208.29	12.0033	17.18
			G4	2192.24	47152.1	1225.39	12.0025	34.28
			G5	510.403	11352.9	1252.78	12.005	61.67
		G6	309.616	7040.89	1271.01	12.0042	79.9	

From the above table: for a narrow guide (g5), curve pairs G2 & G5 and G1 & G6 (fig. 49c) both show similar amplitudes/powers, bandwidths, and are reasonably symmetrically placed on both sides of the pump wavelength (centre wavelength mismatch is considered to be results of SPM effect). This clearly shows that FWM is the dominating effect for SC output spectra for this guide. G4 (Fig. 49c) is formed by depletion of the pump due to SPM. FWM then leads to the formation of G3. XPM causes energy transfer between the G3 & G4 pair resulting in different amplitudes/powers and bandwidth, but are still located symmetrical to the pump. However, for the wider waveguide (g36), where FWM effect does not show as there is no curve fitting pairs with the same characteristics as in g5. SPM contributes the most to SC generation as G1 in fig. 50c and G3–G6 in fig. 51c all appear in the longer wavelength (lower photon energy) side of the pump wavelength. G2 & G3 and G1 &

G4 pairs in fig. 51c shows the signature of XPM effect (differences in amplitudes/powers as shown in equations 12 & 13 in section 2.2.5), but the same effect is not shown in fig. 50c, meaning that XPM requires phase-matching condition to be satisfied.

5.1.2 Output Spectra at ~1600 nm

Figures 52(a)-54(a) show the output spectra for two waveguides under different pump powers close to 1600 nm pump wavelength, and figures 52(b)-54(b) and 52(c)-54(c) show the Gaussian curve fittings to these output spectra from each waveguide at pump powers of 1.5 mW for g5, 1 mW for g36, and highest used power for both. As was the case in the previous section, g36 was coupled at two different positions under the same pump conditions. The output spectra for pump wavelength close to 1600 nm give similar bandwidth as was the case for pump wavelength close to 1200 nm for the narrow waveguide. The highest average obtainable power reached by our OPA pump source at a wavelength of 1600 nm was 2 mW instead of 3 mW, therefore, the output pulses are not broadened significantly for the wider waveguides. The other difference between the 1200 nm outputs and 1600 nm outputs is that the side peaks are generated at shorter wavelength side instead of longer wavelength side for 1200 nm or both sides of the fundamental pump output. The reasons for the difference are described later in this section. Table 3 compares the fitting parameters for each constituent Gaussian peak for output spectra from the two waveguides at the highest pump power.

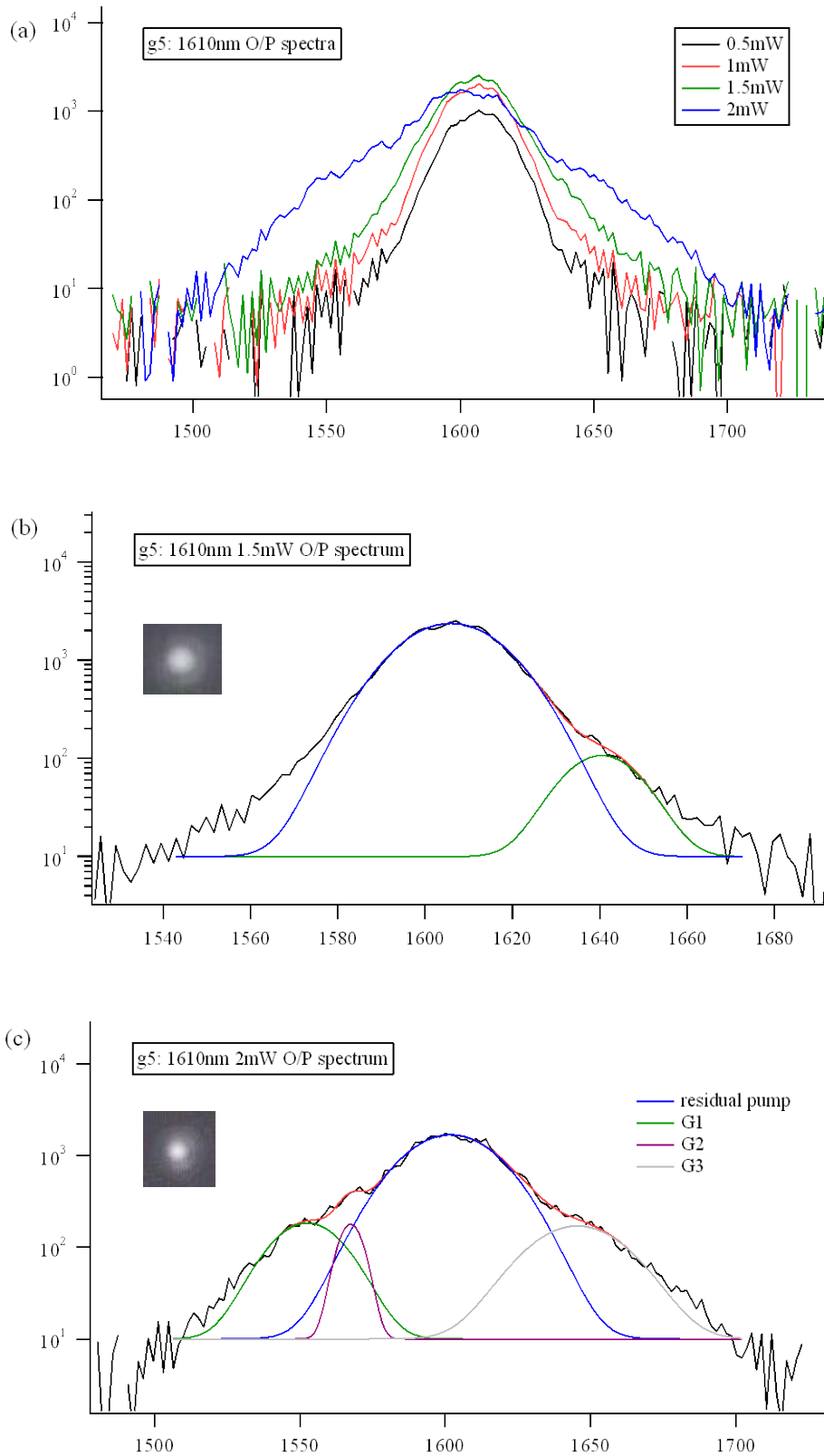


Figure 52: Output Spectra of g5 at 1610 nm: (a) at different average power levels (b) spectral fitting for 1.5 mW output (Inset: mode profile image) (c) spectral fitting for 2 mW output (Inset: mode profile image)

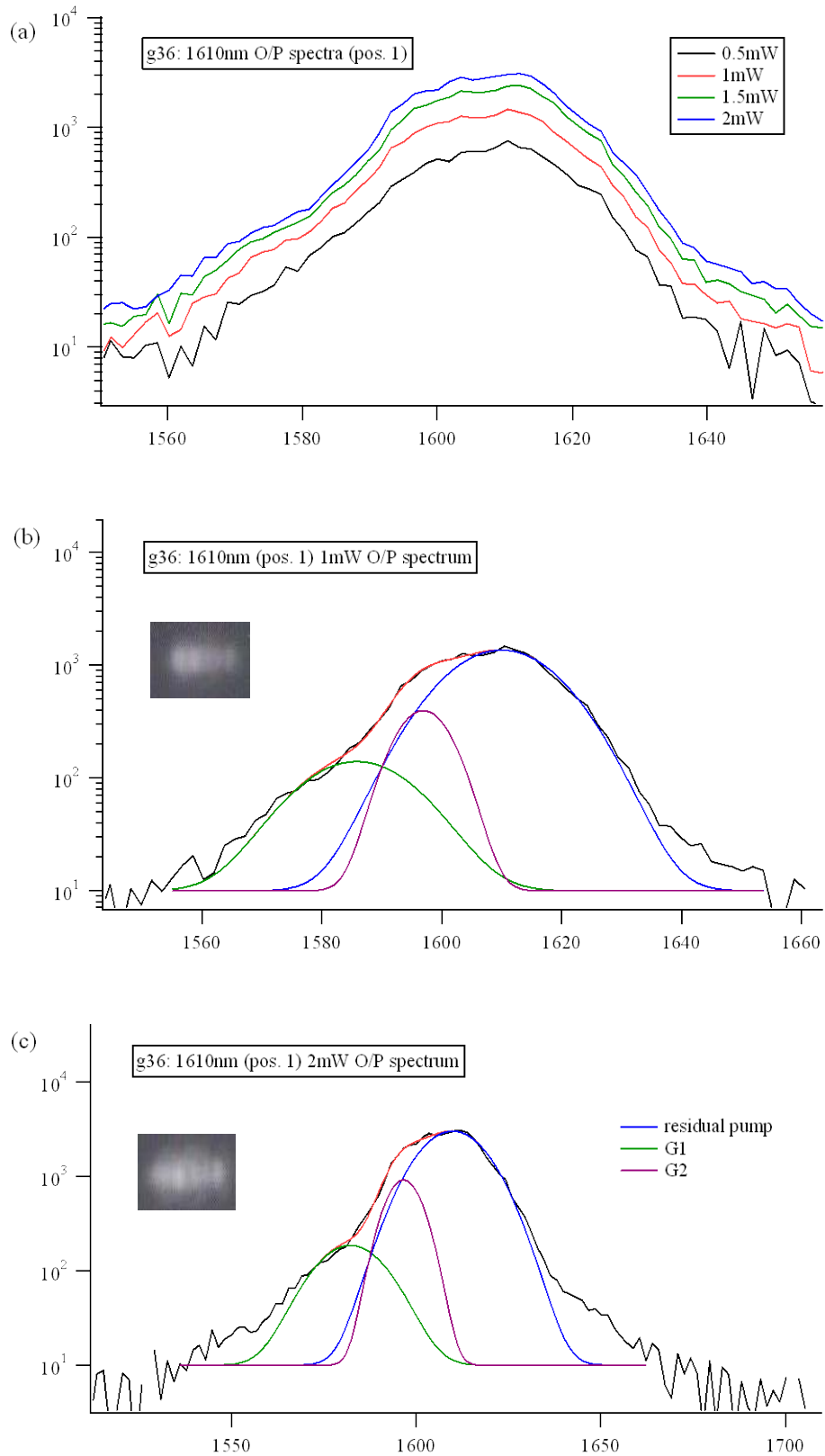


Figure 53: Output Spectra of g36 coupling position 1 at 1610 nm: (a) at different average power levels (b) spectral fitting for 1 mW output (Inset: mode profile image) (c) spectral fitting for 2 mW output (Inset: mode profile image)

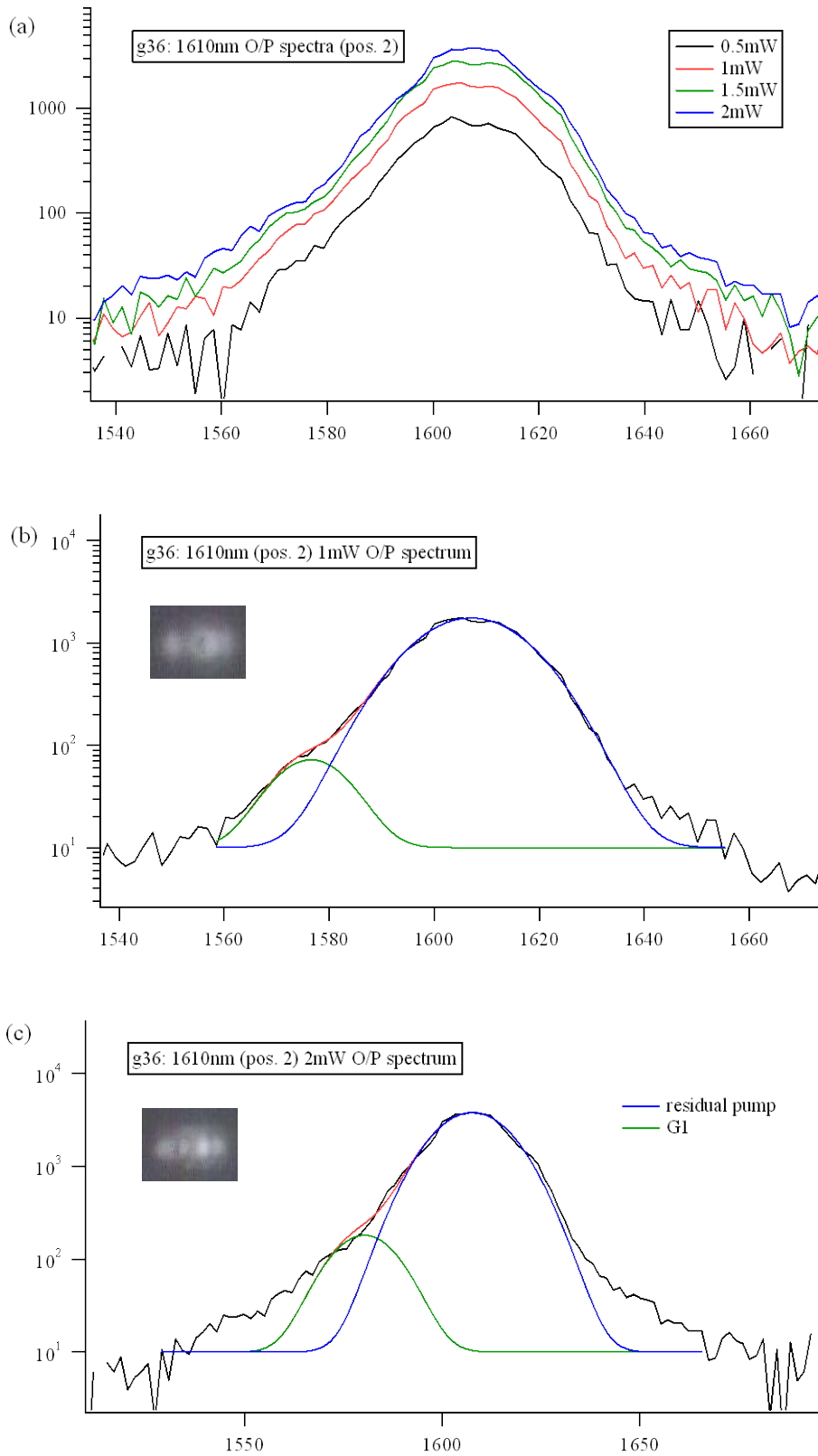


Figure 54: Output Spectra of g36 coupling position 2 at 1610 nm: (a) at different average power levels (b) spectral fitting for 1 mW output (Inset: mode profile image) (c) spectral fitting for 2 mW output (Inset: mode profile image)

Table 3: Fitting parameters of output spectra at pump wavelength of ~1600nm

λ_{pump} (nm)	P_{pump} (mW)	Guide	Fitting curve	Amplitude	Relative power (integrate area)	Peak position (nm)	Width (nm)	Position difference (with offset) (nm)
1610	2	g5	Residual pump	1684.98	67078.8	1601.83	21.8883	0
			G1	174.361	6160.08	1552.56	16.4705	-49.27
			G2	169.835	2200.8	1567.45	5.81081	-34.38
			G3	161.297	7601.84	1645.43	21.8883	43.6
		g36 (pos. 1)	Residual pump	3013.85	68233.9	1609.85	12.5869	0
			G1	176.307	4846.83	1582.14	12.5869	-27.71
			G2	908.27	11105.9	1596.55	6.58737	-13.3
		g36 (pos. 2)	Residual pump	3783.25	91359	1607.62	13.4635	0
			G1	171.544	4220.59	1580.31	11.1714	-27.31

As shown in table 3, G1 & G3 in fig. 52c forms a FWM pair with similar amplitudes/powers, bandwidths, and equal wavelength difference relative to the pump/central wavelength in narrow guide (g5), where there is no such pair for the wider guide (g36). Fig 52b indicates that for 1.5 mW pump power, there is broadening induced by SPM, and G2 in fig. 52c could be the combination resultant of SPM and XPM. SPM and XPM are not clearly shown in the analysis of g36 either, which might be caused by detection limits of the spectrometer or other factors that is currently unknown. Generation of the shorter wavelength components (G1 & G2 in fig. 53c, and G1 in fig. 54c) may be caused by the dispersion properties of the waveguide (especially for higher-order modes in wider waveguide).

5.2 Relations between Output Spectra and Material Properties

The third-order susceptibility ($\chi^{(3)}$) of the Ta_2O_5 waveguides has been calculated in section 4.2.1. There is clear evidence of SPM, XPM, and FWM effects shown by curve fitting for the output spectra (see fig. 49). Once the material properties

(especially the nonlinear properties) are determined for the waveguides, the design and optimization of the devices could then be realized. The plan of actions for the next stage of the project is outlined in chapter 7.

Chapter 6 Pump-Probe Experiment on Planar Tantalum Pentoxide Waveguides

The very large $\chi^{(3)}$ value for Ta_2O_5 measured in chapter 4 suggests that the planar Ta_2O_5 waveguides have great potential as a base material to make several useful nonlinear optical devices. One of the most interesting possibilities is the controlled use of optical parametric effects to generate wavelengths which are difficult to obtain using a purely conventional semiconductor laser design. Therefore, this chapter examines stimulated four-wave parametric amplification in the Ta_2O_5 waveguides under presence of two input laser beams (one pump and one seed) utilizing a time resolved pump-probe experiment setup.

The experimental results presented in this chapter demonstrate broadly tunable $\chi^{(3)}$ nonlinear optical parametric processes over the wavelength range of 557 nm – 600 nm and 1200 nm – 1600 nm, within 7 mm long planar tantalum pentoxide (Ta_2O_5) rib waveguides. The waveguides show parametric conversions from either higher (visible wavelengths) to lower (near infra-red wavelengths) photon energies or from lower (near infra-red wavelengths) photon energies to higher (visible wavelengths) when pumped at a wavelength of 800 nm (1.55 eV photon energy) and seeded by a visible or IR laser beam.

The dispersion properties of the waveguides are measured using a broadband, time resolved spectroscopic measurement system (based on a nonlinear Kerr gate) and

simulated using RSoft CAD package, to see if there is any possibility for making nonlinear photonic chip based on the Ta_2O_5 waveguides. The analysis of experimental results of the stimulated four-wave parametric amplification effect, dispersion measurements of the waveguides and simulation data show that there is real potential to make on-chip nonlinear photonic devices from Ta_2O_5 planar rib waveguides pumped by a compact low cost source.

6.1 Pump-Probe Experiment Setup

6.1.1 Device Fabrication and Testing

Ta_2O_5 waveguide samples made using the same fabrication process as described in section 4.1.1 are used in this experiment. Figure 55 shows a cross-sectional SEM (scanning electron microscope) image of the tested waveguide samples with widths of $6.6 \mu m$, $9.41 \mu m$, $9.85 \mu m$, and $11.65 \mu m$, designated from here on as guides g14, g20, g21, and g25, respectively. Before commencing this new investigation of nonlinear effects in the guides, further tests for laser induced damage were performed on a test guide of a selected waveguide set (made on the same wafer for sacrificial tests) and showed that there was no induced waveguide damage with 150 fs pulses at 100 kHz repetition rate from a Coherent Ti:Sapphire regenerative amplifier (RegA9000) and OPA9400 delivering 20 nJ /pulse energies (or 2 mW in average power) over the idler output tuning range of 1200 – 1650 nm and energies up to 50 nJ /pulse (or 5 mW in average power) over the parametric output range of 560 – 600 nm of OPA9400 [1].

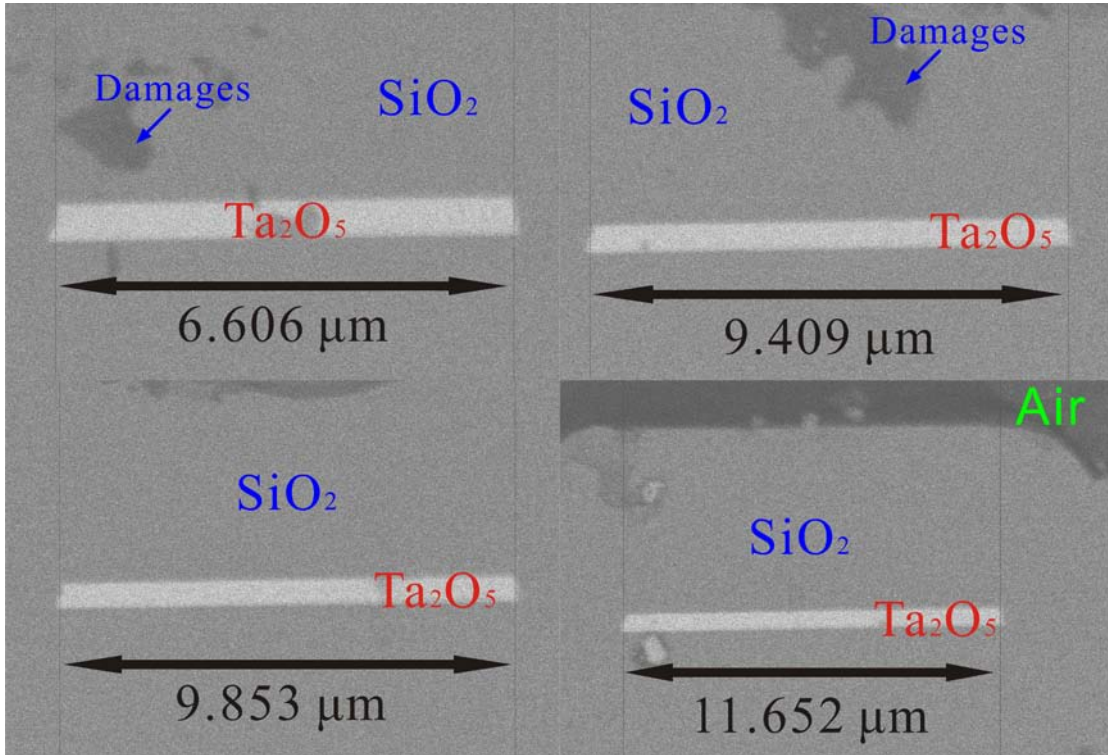


Figure 55: Cross-sectional SEM images of 7 mm long waveguide sample facets after experiments. All waveguides have thickness of 500 nm and widths as follows: 6.6 μm (top left) g14, 9.41 μm (top right) g20, 9.85 μm (bottom left) g21, and 11.65 μm (bottom right) g25 respectively

6.1.2 Pump-Probe Setup

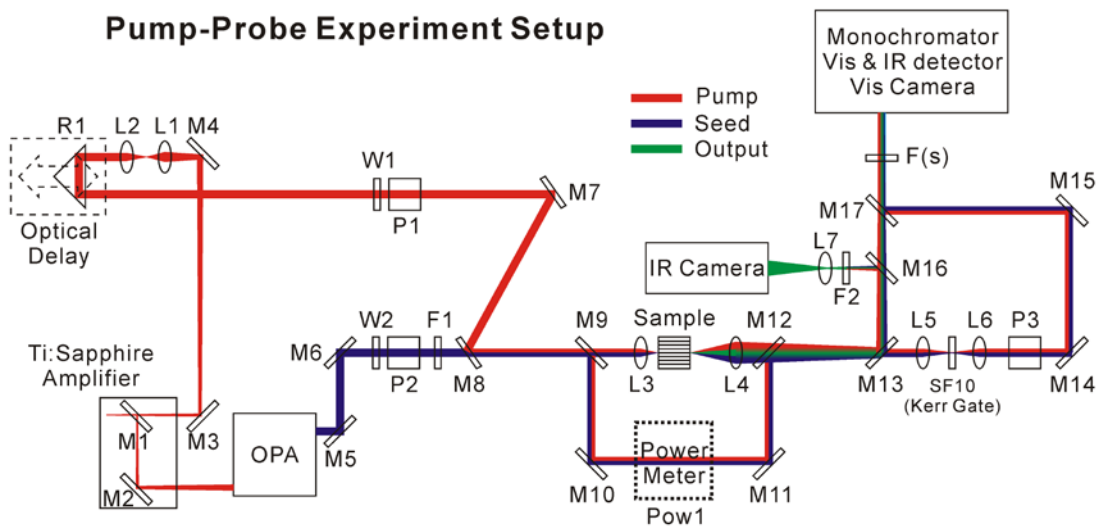


Figure 56: Experimental setup for the on-chip four-wave parametric amplification demonstration. Pump and seed beams are brought together as a co-linear beam pair using a

reflective bandpass filter (M8) before being coupled into the waveguide samples. The output consists of residual pump, residual seed, and parametric output, which passes through a Kerr Gate when required, are collected by monochromator and IR/Visible cameras

6.1.2.1 Pump and Seed Optical Path

Figure 56 shows the experimental setup used for the pump-probe experiment for demonstrating the on-chip four-wave parametric amplification. The mode-locked ultrafast Ti:Sapphire regenerative amplifier which gives 150 fs pulses at 100 kHz at 800 nm provides the pump beam utilizing just 5% of its average power. The remaining 95% power is used to pump the Coherent OPA9400 which provides tunable IR over range 900 to 1600 nm (limited by the detection limit of the spectrometer and InGaAs detector array) or visible pulses over the range 500 to 700nm for the purpose of seeding (i.e. the probe beam). The pump beam is firstly collimated by lenses L1 & L2, and then fed into a retroreflector (R1) mounted on a 400 mm long motorized linear stage. An anti-reflection (AR) coated lambda-half wave plate (W1) and an AR-coated linear polarizer (P1) is used to control the pump power and establish a fixed 45-degree polarization for the pump beam with respect to the seed beam. The seed beam power is adjusted by W2 and P2 polarization set in a similar manner. The polarization for the seed beam is set to be perpendicular to the table which allows transverse magnetic (TM) mode coupling into the waveguides sample. The seed beam then passes through a colour filter (F1), which removes residual pump and beam products from the BBO crystal in the Coherent OPA. A reflective filter (M8) which reflects the 800 nm pump beam but allows the corresponding seed beam pass through is used to bring the pump and seed beams into co-linear propagation before focusing them both into the sample or Kerr gate, (depending on the positions of removable mirrors M9 and M12).

6.1.2.2 Zero-Time Delay Detection

In order to synchronize the two beams at the sample waveguide in the time domain, i.e. setup 'zero-time delay' between pump and seed beams, removable mirrors (M9 and M12) are placed in the beam paths to divert the two beams into the Kerr gate which consists of two lenses (L5 & L6) for input and output coupling, and one SF10

nonlinear glass and a linear polarizer (P3). Figure 57 illustrates the experimental setup of the zero-time delay detection with optical path distance information. The Kerr gate is configured as polarization gate (PG), where polarizer (P3) is placed in horizontal polarization, which blocks the seed beam when SF10 is not active. The working mechanism of the PG configuration has been well established in many previous publications: when the photons from both pump and seed beams arrive at the same time, the nonlinear glass will introduce a polarization rotation to the seed photon so that the IR detector behind the collection polarizer could see the seed beam [93]. Therefore, it is critical that the two beams overlap exactly at the same spot inside the SF10 nonlinear glass plate for this experiment. The activated Kerr gate could affect the polarization of the seed beam when the pump pulse and seed pulse arrives at SF10 glass at the same time. The output of the Kerr gate is collected by a monochromator equipped with both IR and visible detectors. The visible detector is also capable of taking images from visible beam over a wavelength range of 200 to 1100 nm.

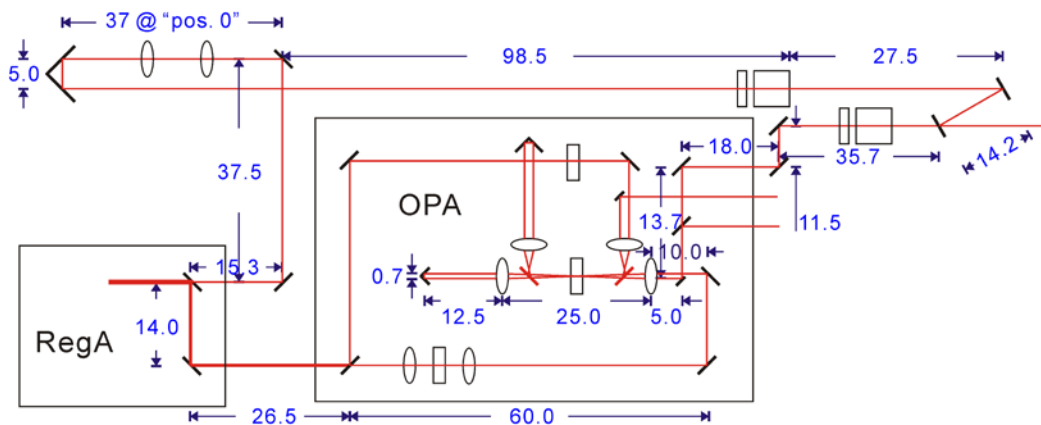


Figure 57: Experimental setup of the zero-time delay detection with optical path distance information (unit: mm)

In practice, the seed polarizer and the crossed collection polarizer pair does not eliminate the seed beam completely. Due to factors such as material dispersion, mechanical errors, and beam instabilities, the overlap of the two beams is not perfect. In addition, both pump and seed pulses have certain pulse width, 150 fs for pump, and ~ 2 ps for seed, which leads to a overlapping distance of 0.7 mm displacements on optical delay line. The approximate zero-time delay position is firstly determined by scanning the whole length of the optical time delay line with both beams coupled into

Kerr gate, and beam polarizations are orthogonal to each other. The output from Kerr gate will rise significantly once the delay line position reach near to the exact zero-time delay position. The accurate zero-time delay position for the optical delay line is then determined by scanning a $\pm 0.5\text{mm}$ distance range with a $5\ \mu\text{m}$ step size, searching for the stage position which gives maximum peak intensity of the seed beam as collected after the Kerr gate. Figure 58 shows the physical position for the optical delay to obtain zero-time delay condition between pump and seed wavelengths, for a number of seed central wavelengths. The physical position for the optical delay position follows linear relationship as seed central wavelength increases.

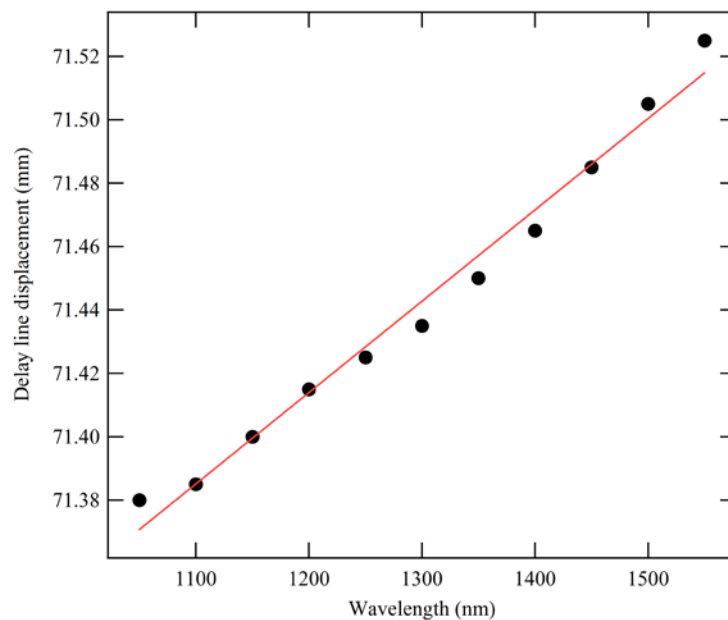


Figure 58: Optical delay line positions for zero-time delay vs. seed beam central wavelengths

Aside: It should be noted that the entire optical table layout was designed to ensure that zero time delay conditions would be obtained close to the start of travel of the moving delay line in order to maximize the adjustable time delay range which can be introduced over the remaining travel range. Whilst not directly important to this experiment, it is important for pump-probe experiments on ‘slow light’ induced by photonic crystal devices where very significant time delays can be introduced by the component on test [94].

6.1.2.3 Results Collection

As the pump and seed beams propagate co-linearly after M8, the two beams will always be synchronized once verified by the Kerr gate output. A short focal length AR-coated (coating matched to seed wavelength) aspheric lens (L3), which provides a near transform limited spot, is used for input coupling to the guides. Output from the end facets of the guides are collected and collimated by another aspheric lens (L4). IR images of the waveguide facet and corresponding mode shape are focussed onto an IR camera by lens (L7) after passing through a long pass filter (F2). Visible images of the waveguide facet and corresponding mode shape are collected by setting the silicon array detector (mounted to the monochromator) to imaging mode and placing the grating to position to 0 degrees which provides specular reflection rather than diffraction of the input beam. All the output spectra are measured by the same monochromator with colour filters that matched to expected output wavelengths, and one or more ND filters depends on the intensities of the output beam. All the results are comparable as the slit size of monochromator, and integration time is kept the same for all measurements. The noise from the measurements is kept as low as possible by taking background spectra and deduct the results from the parametric outputs.

6.2 Pump-Probe Experiment Results

6.2.1 Visible Seeding Results

Silicon dioxide (SiO_2) clad Ta_2O_5 planar rib waveguides with core thickness of 750 nm and widths of $7\ \mu m$, $10\ \mu m$, $10.5\ \mu m$, and $12.5\ \mu m$, were pumped with co-linear coupled 800 nm pump and visible seed beams. The visible wavelength seed beam, i.e. signal beam, was tuned over wavelength range 557 – 600 nm with average powers of 0.01 – 5.0 mW (adjusted by W2 and measured by a power meter (Pow1 in figure 56) for all wavelengths used. The visible beam goes through a pair of visible AR coated lambda-half wave plate and polarizer with average power limited to under 5 mW, and filtered by a KG5 filter to remove the IR products from the OPA. The pump and seed beams are brought together to propagate co-linearly by a reflective 700 nm short-pass

filter, which removes the residual 800 nm from the OPA at the same time. A visible AR coated short focal length ($f = 3.1$ mm) aspheric lens is used to couple both beams into the waveguide sample (L3 in figure 56). An identical lens is used for output coupling (L4). The outputs from the waveguide device are collected by the monochromator after passing through a colour filter that removes pump and seed beams, and one or several ND (neutral density) filters to reduce the intensity of the parametric outputs at the detector to a measurable level. The power dependent measurements were taken at average pump power range of 1.0 – 13.0 mW (adjusted by W1 and measured by power meter Pow1 in figure 56).

Figure 59 shows the parametric gain of the output beam when seeding a device at visible wavelengths with a low seed power (0.5 mW average power). At this low power the pump depletion effect is eliminated. Waveguide losses over the visible region for the same sample were measured (using end fire coupled white light transmission spectroscopy) to be approximately 18 dB on average (as shown in inset of figure 59). The measured parametric gain for this particular sample was measured to be very close to zero, despite the known high level of coupling loss (18dB) and surface scattering. This result indicates that with improvement in waveguide loss, the material and device configuration should be capable to provide parametric gain.

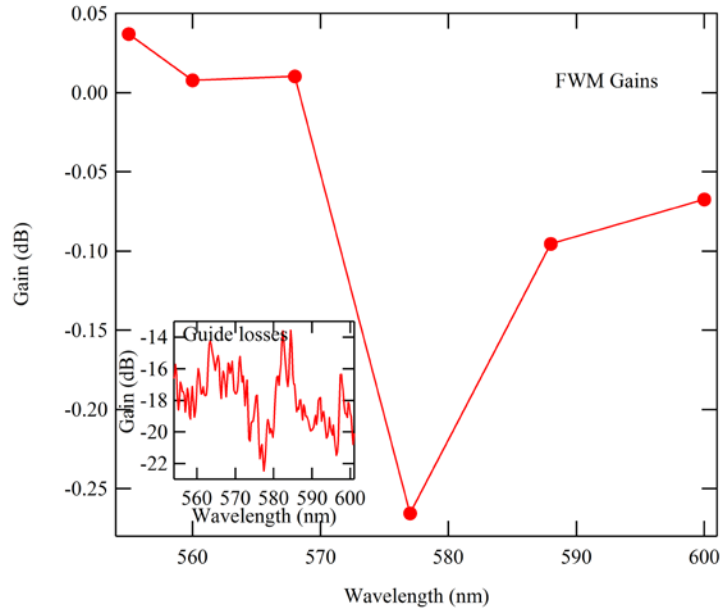
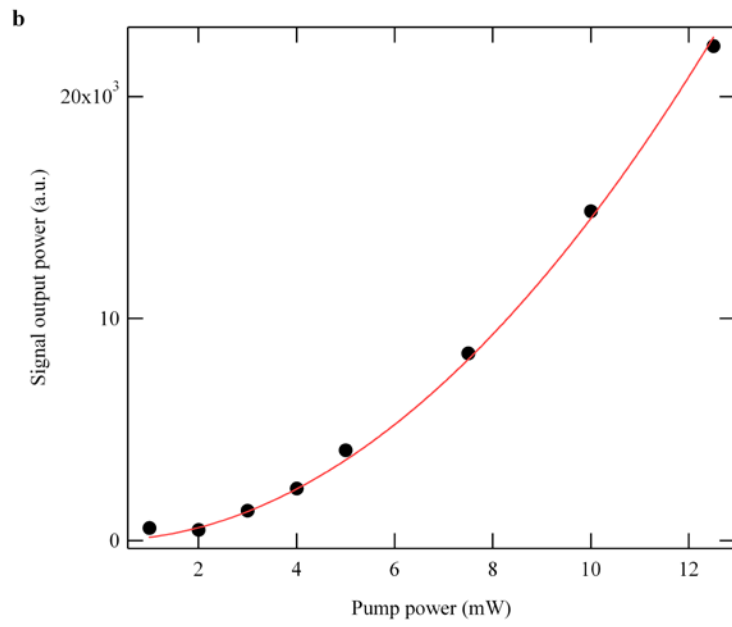
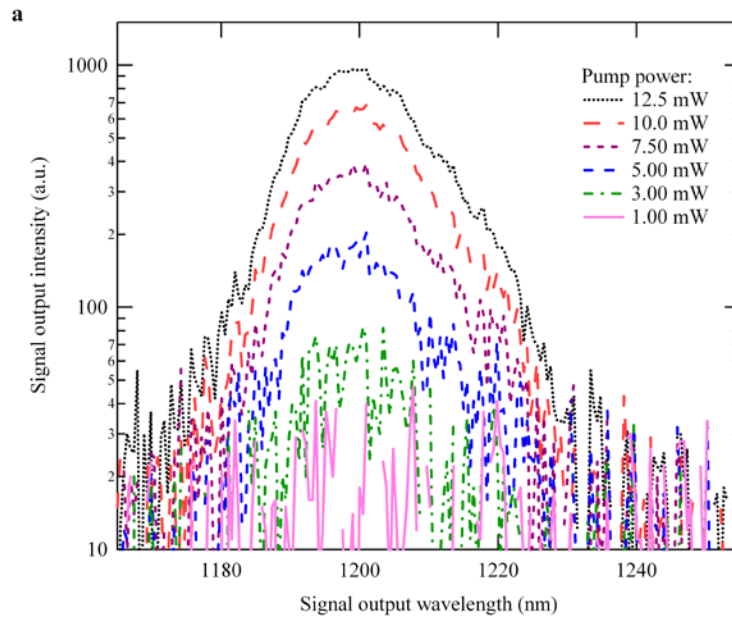


Figure 59: Parametric gains vs. visible seed (signal) wavelengths of stimulated four-wave parametric amplification from planar Ta_2O_5 waveguide g20. Inset: guide losses at examined visible wavelengths

Figure 60a shows the output spectra from guide g25 for the pump-probe experiment when seeded at around 601 nm with 5 mW average power for several 800 nm pump powers. The parametric output spectra increase with pump power. Figure 60b plots the maximum intensity with theoretically predicted values superimposed, confirming that it is proportional to the square of the pump power, i.e. $y = A \cdot x^2$, where coefficient A for the maximum pump power could represent the efficiency of each seed wavelength. Figure 60c shows the seed wavelength over the examined range with the corresponding peak parametric output wavelengths. The peak output wavelengths obtained from this experiment satisfy the $\chi^{(3)}$ parametric relations (within experimental error range), where two pump photons and one seed photon are involved.



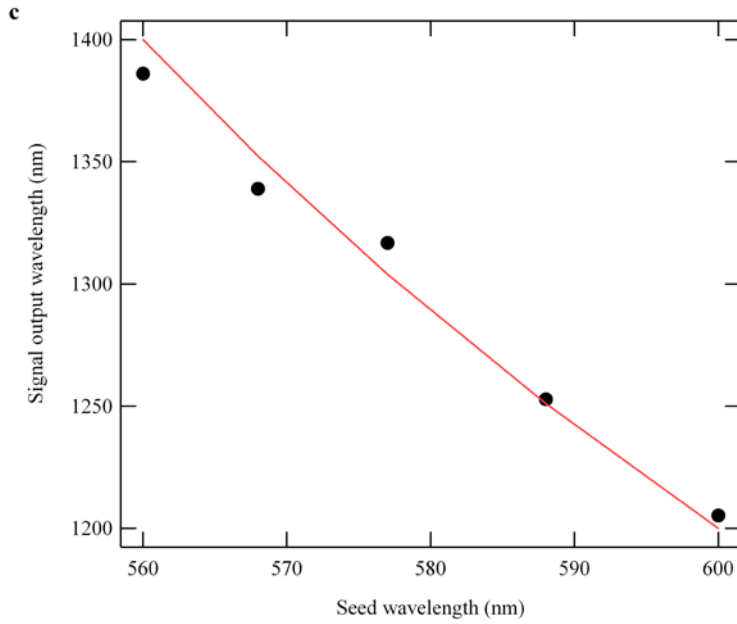


Figure 60: Parametric output data of guide g25 from visible seeding. (a) parametric output spectra for different pump power levels with the same seed power input (b) theory expectation (line) and experimental results (dots) of intensities of parametric outputs vs. input pump powers (c) theory expectation (line) and experimental results (dots) of peak parametric output wavelength vs. input seed wavelength

Having looked at the pump power dependence of the beam for fixed seed power, it is also interesting to see how the parametric output changes with seed power for fixed pump power (fig. 61). For fixed pump power, the waveguide parametric output power also increases with the visible seeding power. Figure 61b shows the visible seed power dependence of output spectra from the same waveguide, i.e. g25, at average pump power of 12.50 mW. Due to pump depletion effects, the relation between output and seed power satisfies the function in the form: $y = A \cdot (1 - e^{-\alpha \cdot x})$, i.e. due to the pump depletion, where $A = 33340.6$, and $\alpha = 0.22143$. When pump depletion is taken into account, change of seed intensity changes the phase-matching condition between pump and see, i.e. effective interaction length will change [3].

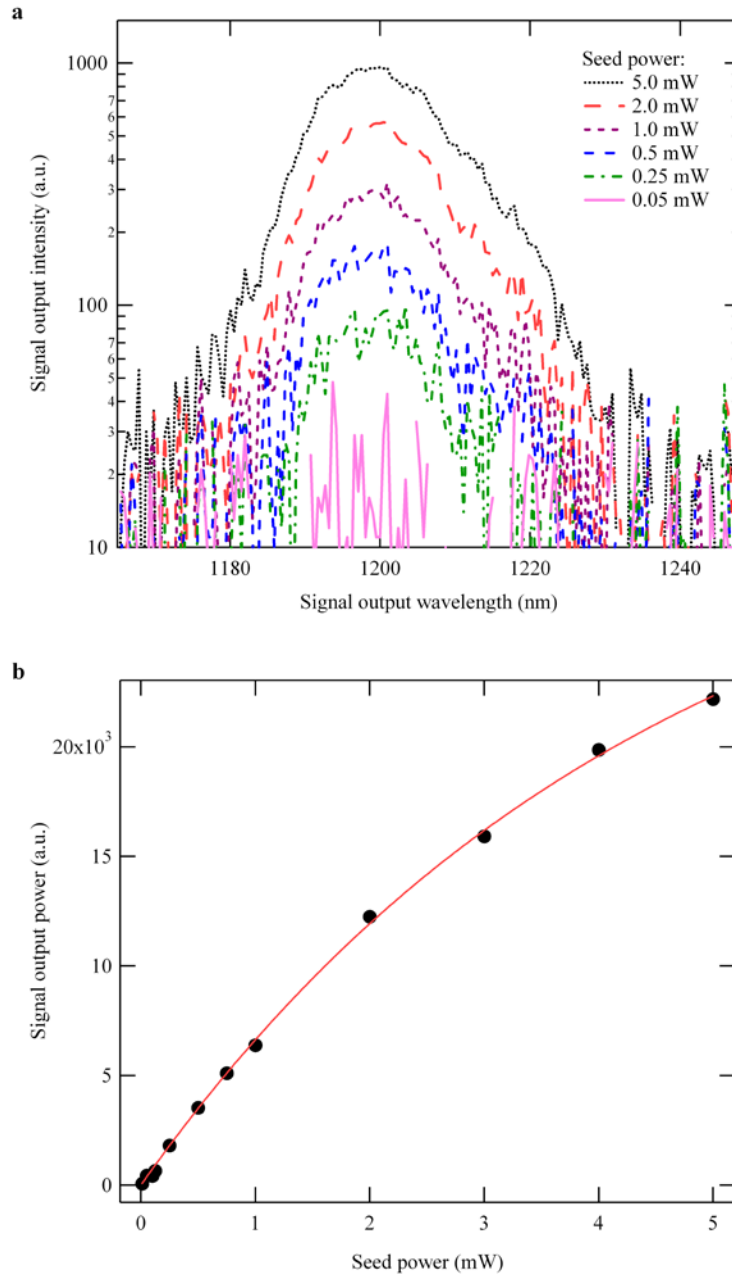


Figure 61: Parametric output data of guide g25 from visible seeding. (a) parametric output spectra for different seed power levels with the same pump power input (b) theory expectation (line) and experimental results (dots) of intensity of parametric output vs. input seed power

6.2.2 IR Seeding Results

The 10 μm wide waveguide (g20) used for visible seeding experiments was pumped with co-linear coupled 800 nm pump and IR seed beams. The IR seed was tuned over wavelength range 1200 – 1600 nm, in 50 nm steps. The idler outputs from the

OPA9400 are filtered by an RG1000 filter to remove the residual 800 nm pump and visible products. The IR beam then goes through a pair of IR AR coated lambda-half wave plate and polarizer. The two beams, pump and seed, are then brought together to propagate co-linearly by a reflective 900 nm long-pass filter. Although the average power for IR seed is below 2 mW for all wavelengths used, it proved to be sufficient enough to stimulate both THG effects and $\chi^{(3)}$ parametric effects. The co-linear beams are then focused into the waveguide by an IR AR coated short focal length ($f = 3.1$ mm) aspheric lens (L3 in figure 56), and the outputs from the waveguides collected by a IR AR coated aspheric lens with $f = 11$ mm (L4 in figure 56). The outputs are then filtered by various filters (F(s) in figure 56), including 700 nm short-pass, or 1000 nm long-pass filters with neutral density ND2.0, and/or ND3.0 filters, before collected by the detectors attached to the monochromator. The power dependence measurements were taken at average pump power range of 0.5 – 13.0 mW (adjusted by W1 and measured by power meter Pow1 in figure 56). The outputs show visible spectra with the parametric outputs and the third-harmonic generation output when the THG outputs are not getting absorbed.

Figure 62 shows the parametric gain of the idler beam when seeding at IR wavelengths with low seed power (0.5 mW average power) to eliminate the pump depletion effect. The results show similar parametric gain as shown in figure 59 to coupling losses, surface scattering, and waveguide losses of approximately 19 dB on average as shown in the inset of figure 62. It has been proved in the next section (section 6.2.3) that it is possible to get gain in seed wavelength from the waveguide if the waveguide losses are improved. It is quite interesting that the outputs, i.e. signal wavelengths, of the four-wave parametric amplification process changes with pump and seed wavelengths.

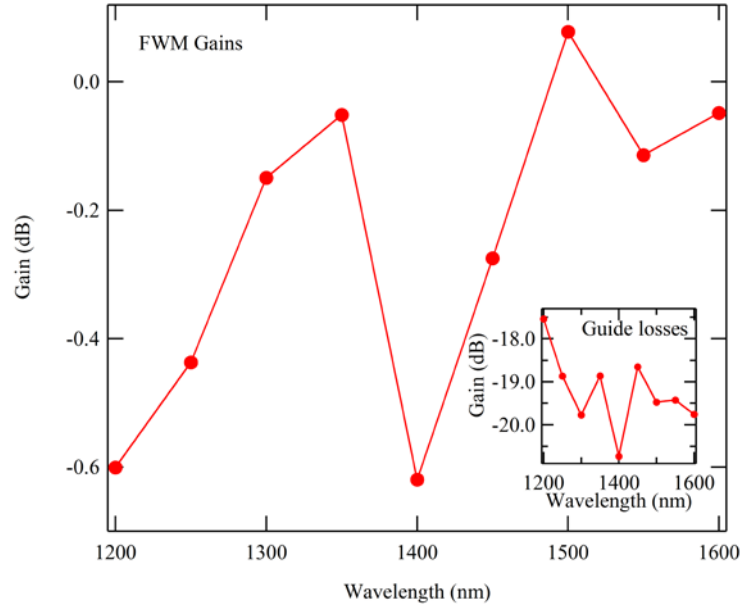
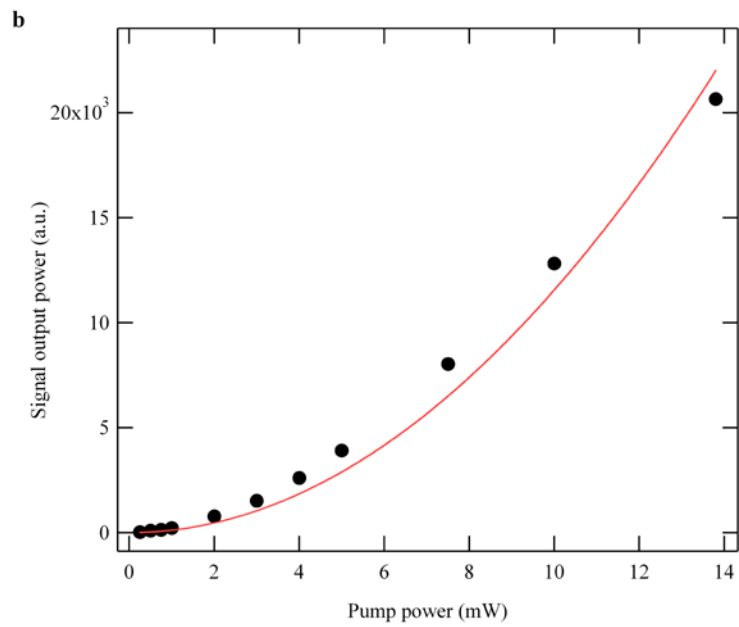
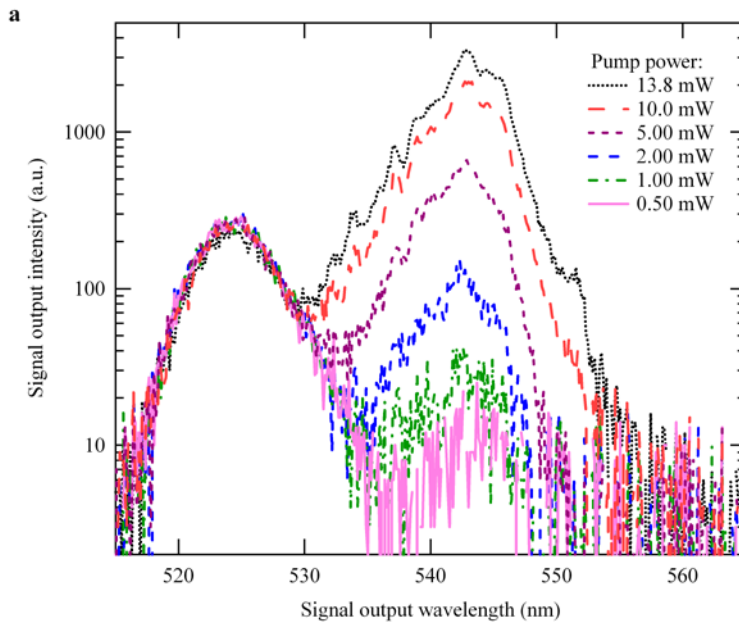


Figure 62: Parametric gains vs. IR seed (idler) wavelengths of stimulated four-wave parametric amplification from Ta₂O₅ pentoxide waveguide g20. Inset: guide losses at examined IR wavelengths

Figure 63a shows pump (800 nm) power dependence of the output spectra from the pump-probe experiment for seeding g20 at around 1550 nm with fixed power. The constant output spectra around 520 nm indicate that the THG outputs is not affected by the pump power, i.e. THG is stimulated only by the seed beam. The parametric output shows peak at around 540 nm as expected for the inverse process of the parametric conversions to the visible seeding. The power dependence relationship between the pump and IR seeded parametric output is the same as the visible seeding, i.e. quadratic relation, as shown in figure 63b. Figure 63c shows output profiles from the examined IR seed wavelengths including the THG outputs. The figure also shows the corresponding parametric output peak wavelengths. The parametric output peak wavelengths obtained from this experiment are as expected for the inverse process of the parametric conversion to the visible seeding.



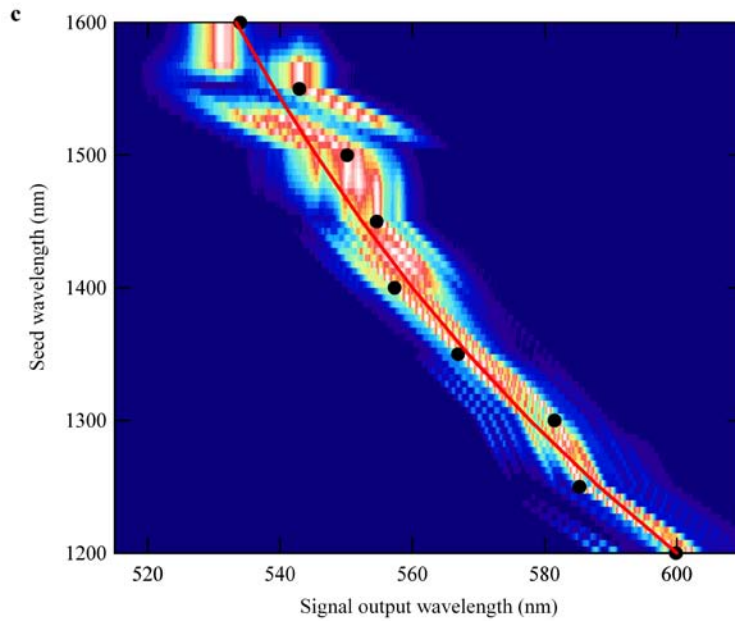


Figure 63: Parametric output data from IR seeding. (a) parametric output spectra for different pump power levels with the same seed power input (b) theory expectation (line) and experimental results (dots) of intensity of parametric outputs vs. input pump powers (c) theory expectation (line) and experimental results (dots) of peak parametric output wavelengths vs. input seed wavelengths. The image also shows expected THG outputs (dotted line), and the spectra profiles of the parametric outputs for each seed wavelength

6.2.3 Four-Wave Parametric Amplification Gain from Er doped Tantalum Pentoxide ridge waveguide devices

In the very last days of this PhD project, a new set of low loss Er doped Ta_2O_5 ridge waveguide devices became available (actually fabricated for a different project). A 2 cm long, 40% etched 1 μm thick core ridge waveguide with 1 μm and 2 μm SiO_2 cladding on top and bottom, was examined using the same pump-probe configuration as shown in figure 56. The width of the tested waveguide is 6.6 μm wide (named as guide g18). The waveguide loss for the Er doped Ta_2O_5 ridge waveguides were tested using a prism coupling method and verified to be 0.8 dB/cm for CW waves at a wavelength of 600 nm and 0.4 dB/cm at 833 nm. These new low loss devices were fabricated on the new Leybold Hellios sputtering system which was recently installed in the Southampton Cleanroom facility (this equipment was not available for the first three years of my PhD). The Hellios system works in a very different way to the OPT

system 400 which was used to produce the original samples tested in this thesis. The Hellios produces material by reactive ion beam assisted sputtering which results in very low loss films which are unobtainable by direct RF magnetron sputtering (as is the case in the OPT system).

Tests on the new waveguide sample probed at a visible seed wavelength of 600 nm showed 1 dB gain for the four-wave parametric amplification process (as shown in figure 64) as follows. Figure 64 shows the measured parametric gain of the output beam with respect to the pump coupling position on the input facet. In this case the guide is relatively wide, so adjusting the input coupling position on the facet affects the order of the coupled mode. As the dispersion for each mode is slightly different, changing facet coupling position effectively changes the phase-matching condition inside the guide.

A maximum gain of over 3 dB was measured at the extremities of the tuning range, and one of the guides (g18 coupling position 1) demonstrated significant gain over the whole wavelength range (590 – 610 nm) (1 dB on average) for the optimized coupling position. This result shows that with proper waveguide design it is possible to obtain parametric gain from Ta_2O_5 planar waveguide devices over a wide wavelength range, provided the coupling and waveguide losses are improved by improved setup and fabrication process (as is the case for these Hellios sputtered samples). We also note that the modal power confinement is much reduced in the new ridge waveguide samples than would be the case for rib waveguides as the spot size is larger and the mode less well confined to the stripe region. Hence the gain figures measured in this experiment (particularly G18 position 1) can be considered to be quite conservative, due to the fact that a large amount of pump power would be coupled to other modes which are not well phase-matched and so do not contribute to the gain. Hence with proper engineering and implementation of single mode rib waveguides (with higher associated modal power densities) we would expect the gain figures to be much higher.

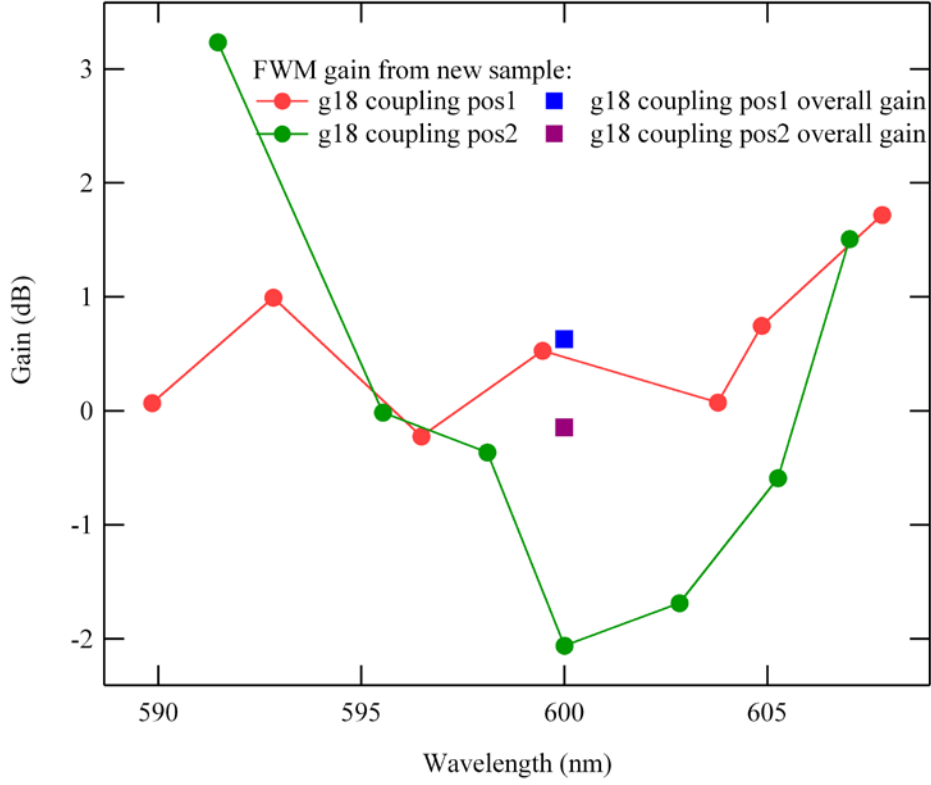


Figure 64: Four-wave parametric amplification gain measured on a 6.6 μm wide low loss Er doped tantalum pentoxide ridge waveguide (g18)

6.3 Pump-Probe Experiment Results Discussion

6.3.1 Relationships between Output Intensity and Pump/Seed Intensity

The theory of third-harmonic generation from the waveguides was described in [95]. The broadband tunable optical parametric process we investigate in this chapter is a different third-order nonlinear process to that involved in third-harmonic generation, i.e. stimulated four-wave amplification. The process involves two of pump photons and one seed photon to generate one beam photon as illustrated in fig. 65. The relationship between the three photons could be expressed as [4]:

$$\omega_{output} = 2\omega_{pump} - \omega_{seed} \quad (26)$$

whereas for THG it would be: $\omega_{output} = 3\omega_{pump}$

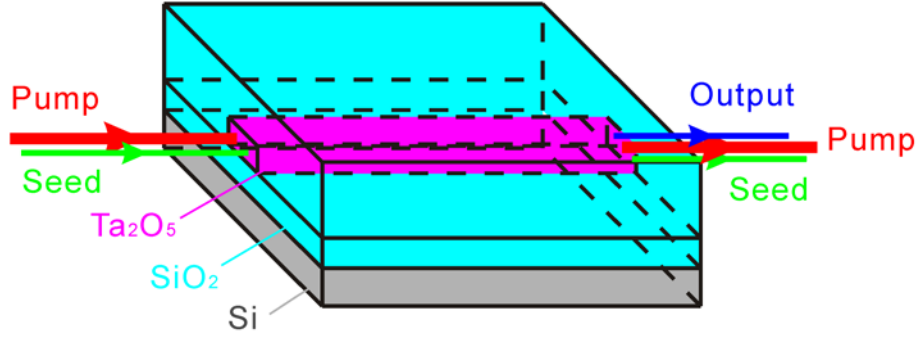


Figure 65: Illustrations of the stimulated co-linear parametric four-wave amplification process in planar Ta₂O₅ waveguides

The intensity dependence of the output beam (I_{output}) of the pump (I_{pump}) and seed intensity (I_{seed}) for the non-depletion regime is given by equation 4 in section 2.2.1 [18]:

$$I_{output} = const \cdot |\chi^{(3)}|^2 \cdot I_{pump}^2 \cdot I_{seed} \cdot l^2 \cdot \left[\frac{\sin(\Delta k \cdot l / 2)}{\Delta k \cdot l / 2} \right]^2$$

where $\Delta k = 2k_{pump} - k_{output} - k_{seed}$ is the wave number difference with the wave number $k = \frac{2\pi \cdot n_{eff}}{\lambda}$ for each component, and $const = \frac{\omega_{output}^2}{(cn_0)^4 \cdot \epsilon_0^2}$ is the same constant as for the THG effect (for the four-photon process) as described in section 4.2.

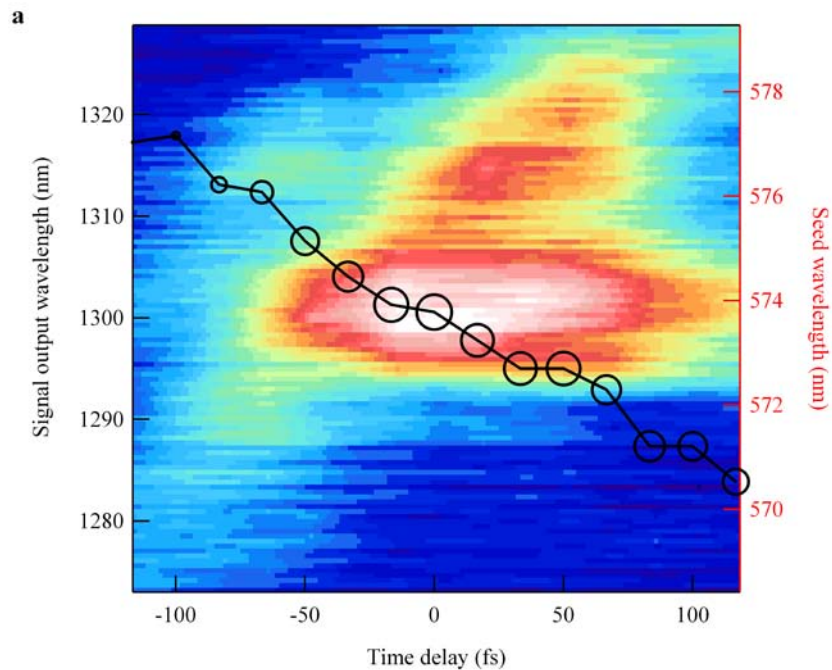
The intensities of parametric output and pump follow quadratic relationships, i.e. $P_{output} = A \cdot P_{pump}^2$ (where coefficient A reflects the efficiency of the process), as shown both in the IR and visible seed experiments (fig.60b and 63b). The IR seed is more efficient for this nonlinear process as coefficients obtained from fig 60b and 63b are similar, but the input seed power is higher for visible seed than IR seed. According to the same equation, beam intensity should be linearly proportional to the seed, but by taking account into pump depletion relations as shown below [96]:

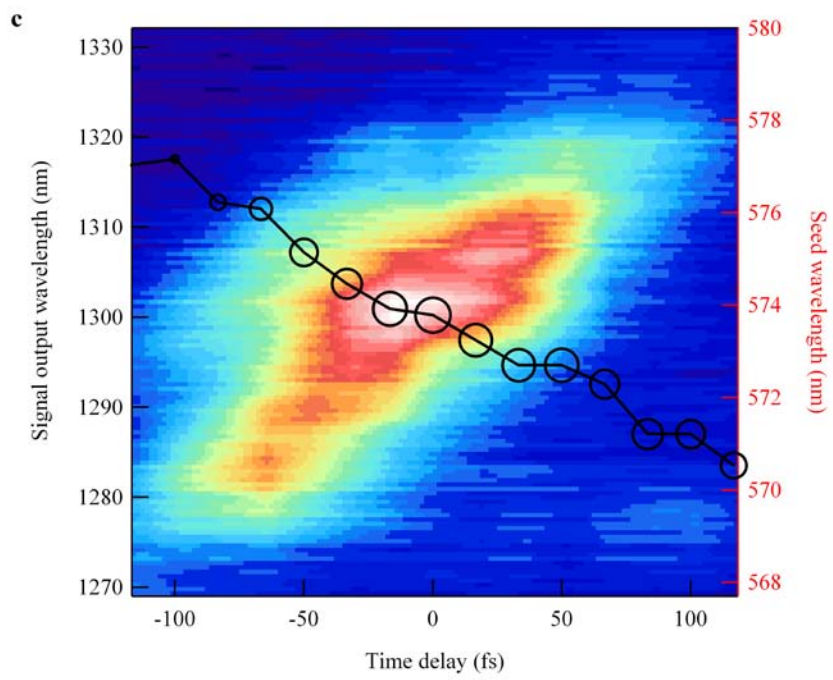
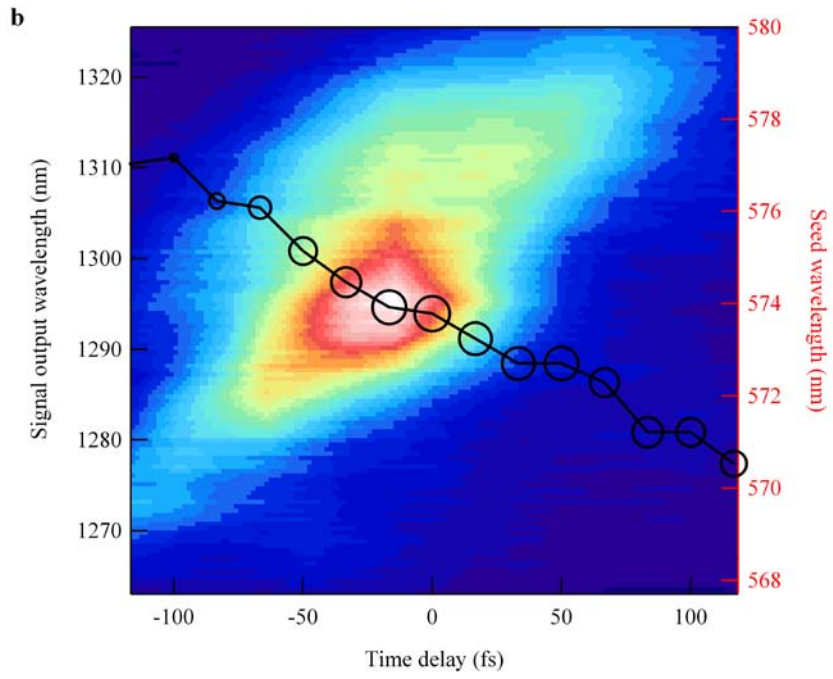
$$y = A \cdot (1 - e^{-\alpha \cdot x}) \quad (27)$$

The experiment results shown in figure 61b verify this relationship.

6.3.2 Relationship between Output Intensity and Pump-Seed Phase-Matching condition

The phase term $\left[\frac{\sin(\Delta k \cdot l/2)}{\Delta k \cdot l/2} \right]^2$ is affected by both the time-delay between pump and seed beams and the dispersion of the waveguide. Figure 66 shows that the parametric output spectra profiles and parametric output peak wavelength changes when changing the time-delay between the pump and the visible (fig 66a, 66b, and 66c) and IR (fig 66d) seed pulses within around ± 100 fs on several different waveguides. The diameter of each circle plotted in figure 66 is proportional to the intensity of the parametric output.





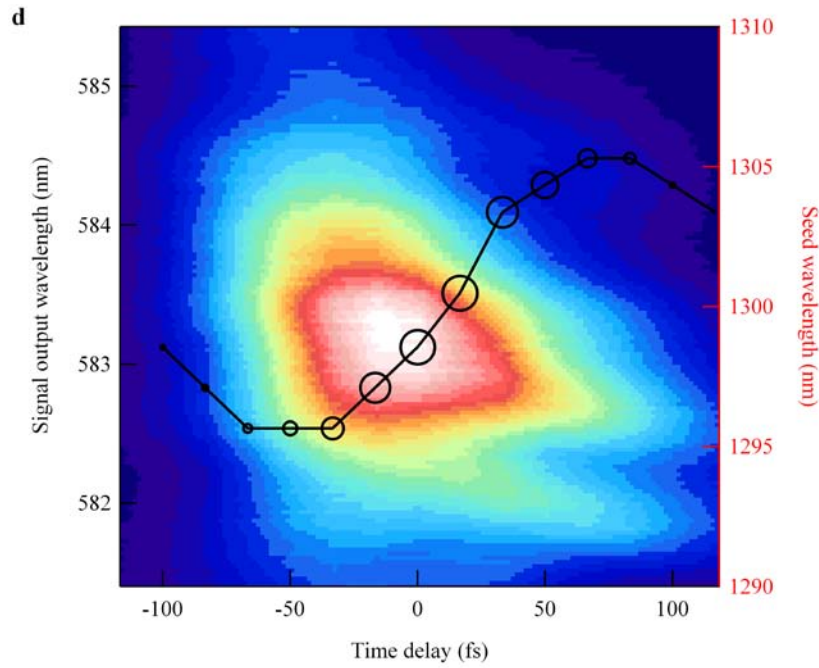
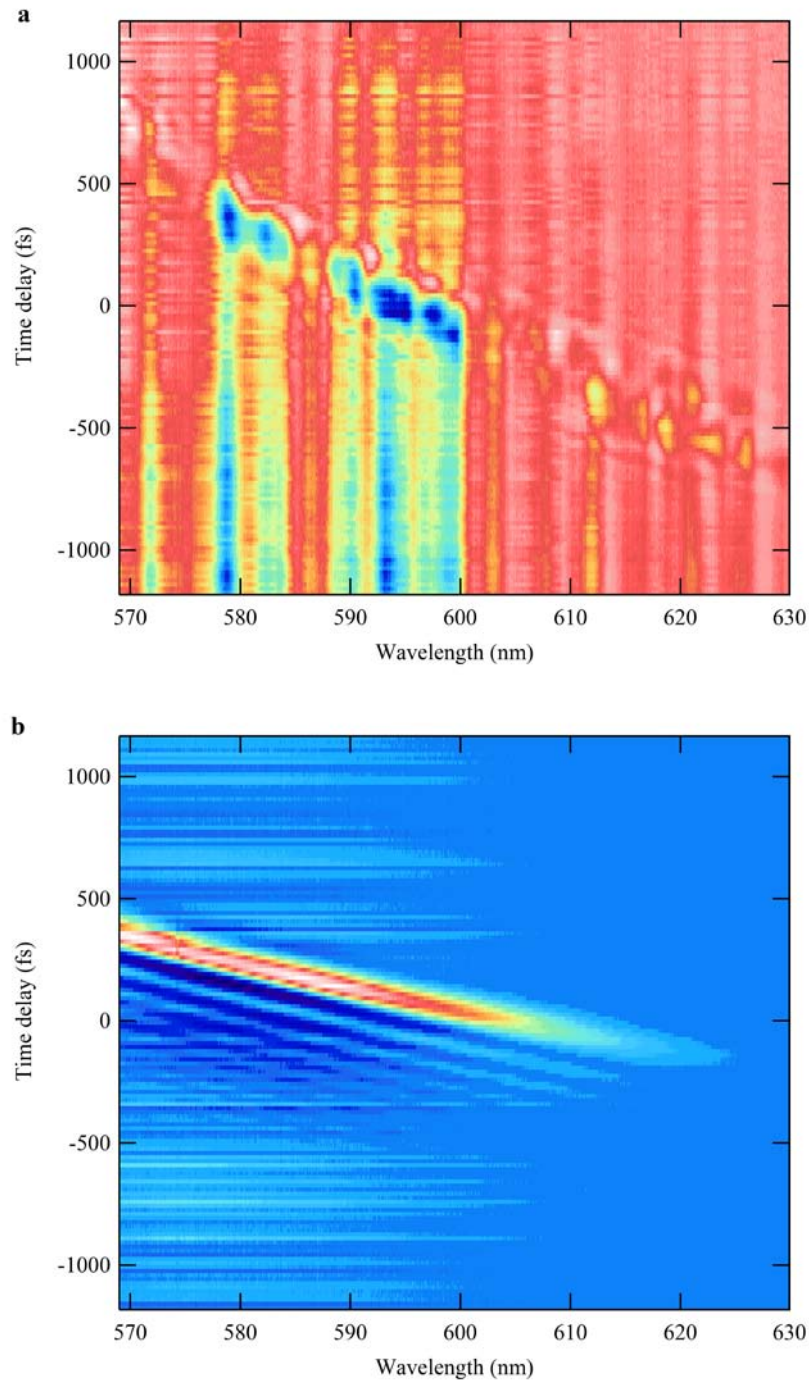


Figure 66: Time dependent spectra output profiles from tested waveguides of both visible and IR seeds with seed peak changes indicated by circles (diameters relative to intensity) within around +/- 100 fs. (a) guide g14 seeded at 577 nm, (b) guide g21 seeded at 577 nm, (c) guide g25 seeded at 577 nm, (d) guide g20 seeded at 1300 nm

The above figures show that it is possible to achieve short-range wavelength tuning by adjusting the time-delay between the pump and seed pulses, but the changing intensities indicate that the phase-mismatch has very large impact on the efficiency of the parametric effect. The other major factor that affects the phase-matching condition for FWM is the dispersion of the waveguides with respect to seed wavelength. The white light generated from sapphire plate inside the Coherent OPA9400 is used to measure the dispersion properties of the waveguides in conjunction with time resolved spectroscopy. By coupling the white light into the waveguides and examining the output through the Kerr gate (the Kerr gate is only transparent when both pump and white light arrive at the same time). The supported modes for one particular wavelength can only transmit through the Kerr gate when the pump pulse arrives at the same time. Therefore, the time-delay between the pump and white light pulses directly reflects the dispersion of the waveguides. The dispersion properties, i.e. refractive index, of the waveguides can also be obtained from software simulations using RSoft CAD. Figure 67a shows dispersion measurements on the examined waveguide (g20) without dispersion corrections. The dispersion of the waveguide is

corrected against the intrinsic dispersion of the optical path (fig. 67b). The parametric output mode images from parametric effect are shown in fig. 67c to provide information for simulation of the dispersion using RSoft CAD package using the same simulation setup as describe in section 3.2.2. Figure 67d show the time resolved dispersion measurements on the examined waveguide (g20), along with the simulated refractive index for 12 supported modes.



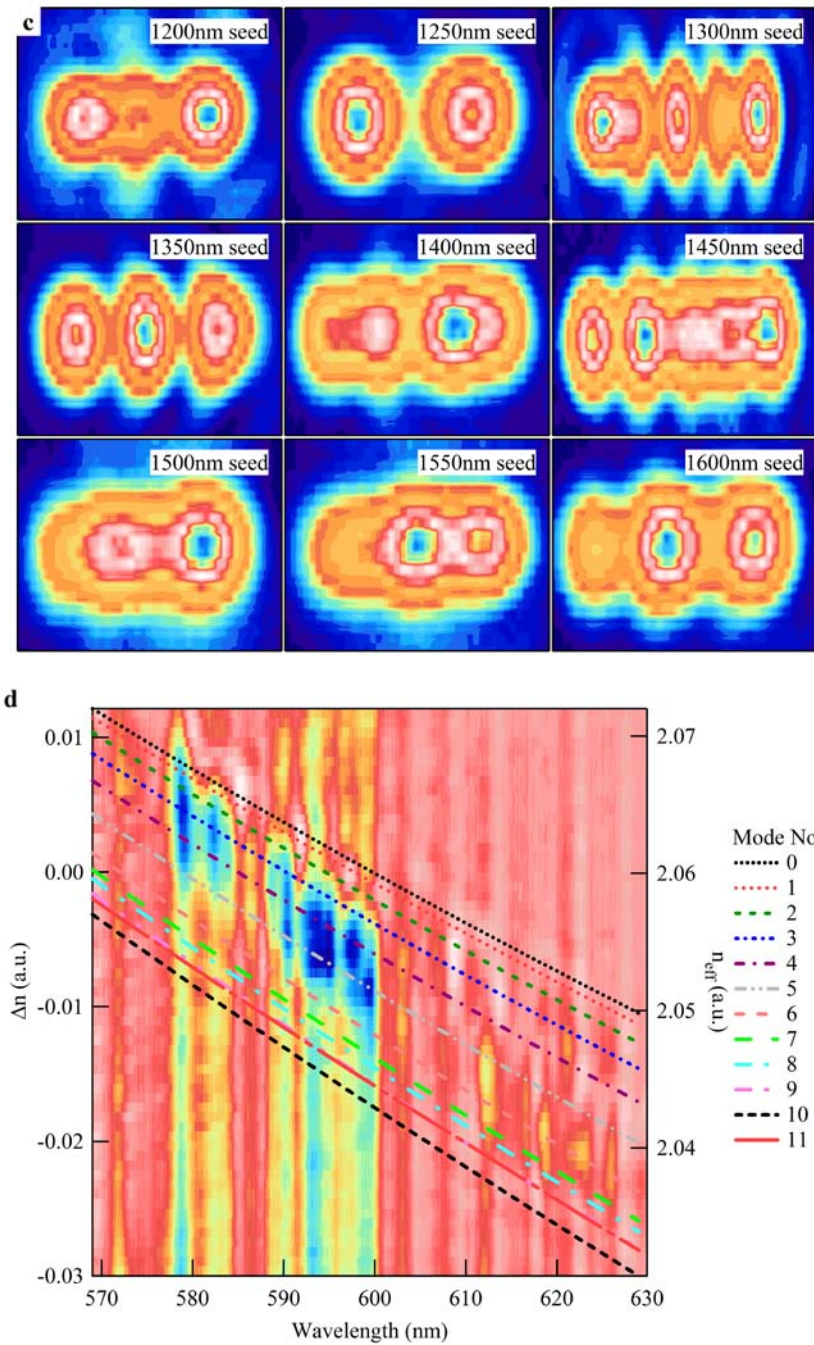


Figure 67: Dispersion measurements on the examined waveguide (g20). (a) Waveguide dispersion without path dispersion corrections, (b) Optical path dispersion, (c) Parametric output mode images from stimulated four-wave amplification effect, and (d) Dispersion measurements by Kerr Gate with the RSoft simulation results of the refractive index for 12 supported modes

The measurement results show that the supported modes are continuous through the examined wavelength range. Although there is mode hopping for different wavelengths, it is possible to tune the parametric output wavelength smoothly by

adjusting the time-delay provided a broadband seed can be coupled into the waveguides with high efficiency over its entire bandwidth along with sufficiently high energy pump pulses to stimulate the FWM effects.

6.4 Summary

In summary, the optical parametric effect has been demonstrated in 7 mm long Ta_2O_5 planar rib waveguides using a time resolved pump-probe experiment setup. The parametric effect works for both low- and high-energy conversion processes. The dispersion properties of the measured waveguides were also investigated through Kerr gate measurements, which show the possibility of making an on-chip optical parametric amplifier by coupling white light seed sources. With improvement in fabrication processes, low loss 2 cm long Er doped Ta_2O_5 planar ridge waveguide samples demonstrated parametric gain of around 1 dB at a test wavelength of 600 nm. As the ridge waveguides suffer from weak coupling (as shown in section 3.2.2), the parametric gain can be improved further by improving the input coupling using rib waveguides. The results presented in this chapter confirm the great potential for making compact ‘on-chip’ nonlinear tunable lasers based on Ta_2O_5 planar waveguides. Further ideas on how to implement this efficiently are presented in the next chapter.

Chapter 7 Future Works

The experimental results presented in the previous chapter verify the viability of developing an on-chip nonlinear photonic device using the Ta_2O_5 material system, and also show that guides may be used ‘as-is’ for dual-band optical coherence tomography (OCT) light source (described in more detail later in the next section).

Further work will explore the potential for utilizing the nonlinear optical effects from Ta_2O_5 waveguides to make useful on-chip devices, e.g. nonlinear on-chip tunable laser. This chapter outlines the ideas for optimizing the nonlinear effects in order to fulfil the objectives of this project.

7.1 Optimization of Third Harmonic Generation (THG)

The third harmonic beams reported in chapter 4 are currently centred at the desired wavelengths but have very low intensities (10^{-5} less) compared to the continuum

beams. According to equation 20, ($I(3\omega) = \frac{4\omega^2}{(cn_0)^4 \cdot \Delta k^2 \cdot \epsilon_0^2} \cdot |\chi^{(3)}|^2 \cdot I(\omega)^3$), there

are two ways to improve the THG beam intensity/conversion efficiency, i.e. to obtain intensity levels similar to the continuum beam:

- 1) Magnify the pump intensity ($I(\omega)$) into the guide
- 2) Change the wave number difference (Δk) within the guide.

- 1) Work presented in chapter 3 of this thesis shows that for a conventional planar waveguide design, changing the waveguide dimensions will not cause any

significant change to Δk , but changes in $I(\omega)$ will be significant. By shrinking the waveguide size to 1/100 of the current sizes (i.e. creating nano-wire waveguides with new dimensions of $375 \text{ nm} \times (50 \text{ nm} \sim 360 \text{ nm})$), assuming coupling loss is the same, the pump power density can be magnified by 100 times in theory. Therefore, the intensity of the THG beam increases with cubic relation and will be magnified by 10^7 times. Provided phase-matching condition is still conserved in the nano-wire waveguides, this should allow the THG beams to reach comparable power levels as the continuum beam. The two major difficulties associated with this method are: a) manufacturing and b) optical coupling. Manufacturing waveguides at nanometre scales with good quality will require very precise micro-machining facilities and careful processing. End fire coupling into the waveguide with nanometre scale sizes will not produce the magnification as expected due to increased coupling losses. Hence, tapered coupling structures (see fig. 68) will be needed to make sure pump light is efficiently coupled in at the input facet and concentrates it in the waveguide section, with maintained mode profile, where most of the nonlinear conversion process occur.

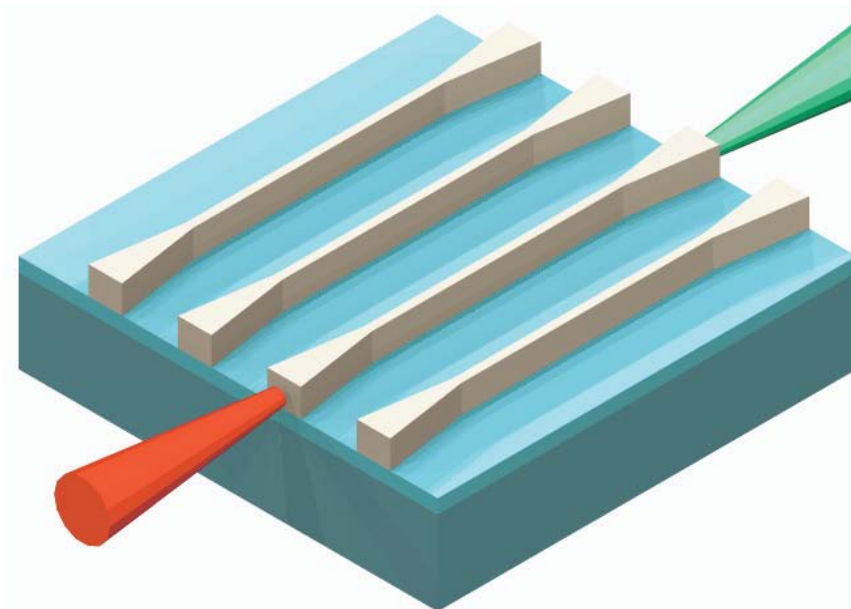


Figure 68: Tapered planar waveguide

- 2) The wave number difference (Δk) can be significantly changed by using photonic crystal (PC) structures such as photonic crystal slab (PCS), which are

capable of changing the effective mode index for certain wavelengths (dependent upon lattice layout and parameters). PCSs are also better for confining light inside small volumes of space than conventional rib or ridge waveguides as they can be designed to allow no light penetration into the cladding regions to the side of the guides, for example, photonic line defect waveguides (see fig. 69) [66]. By changing both Δk and $I(\omega)$ within the structure, high intensity of the THG beam will be much easier to obtain than using rib or ridge waveguides designs. There is a issue of loss with photonic crystal structures, but it could be controlled by modifying the refractive index of lattice holes [97].

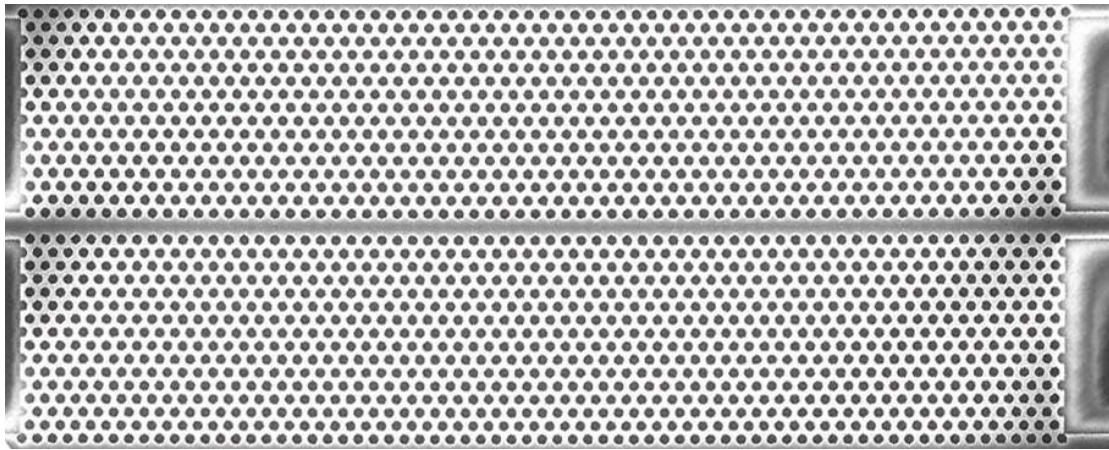


Figure 69: Photonic crystal slab with line defect [66]

7.1.1 Dual-Band Optical Coherence Tomography (OCT)

The dual-band OCT utilizes two different wavelength bands instead of one to improve the axial resolution of the system. There are two main types of dual-band OCT systems: the first uses two continuum beams with centre wavelengths at around 800nm and 1300nm to provide two images with different resolutions. By combining these two images, the resolution of the system is greatly improved (from 10 – 15 μm to less than 5 μm) [98-100]. The second type utilizes a continuum beam centred at a long wavelength for imaging, and a shorter wavelength as a resolution reference to achieve better overall system resolution (time domain sensitivity can be improved by more than 30 dB) [101-103]. The measurement results for our waveguides fit the second type of the system, in which case the low power THG beam could act as the

reference and the continuum beam used for imaging. In order to use the Ta_2O_5 waveguides for the OCT system, (which normally requires the centre wavelength to be 1300 nm) further tests should be performed to verify that there is THG at pump wavelengths lower than 1400 nm, since we have only demonstrated THG at wavelengths of 1470 nm and longer wavelengths in the work above. There should be no fundamental issue to achieve this, but there may need to be small adjustments to the phase-matching condition to optimize conversion efficiency (achieved by modifying cross-sectional profile of the waveguide). In addition, the OCT system requires relatively wide and flat continuum spectrum with low noise, hence, apart from increasing the THG beam intensity discussed above, the continuum output from the waveguides need to be optimized for the dual-band OCT system (approximately 200 nm bandwidth). Possible ways of optimizing the SC output from the waveguides are discussed in the section 7.2.

7.1.2 OCT with Fluorescence Detection

OCT with fluorescence detection is currently achieved using two separate light sources [104, 105]. If THG beams obtained in the experiments presented in chapter 4 could be magnified to a sufficient intensity level to obtain fluorescence, the waveguides would also be suitable for OCT imaging with fluorescence detection at the same time. As most fluorescence effects are excited by higher energy photons (i.e. shorter wavelengths), the THG beams must be spectrally located around 400 nm. Therefore, Ta_2O_5 waveguides used in above experiments will need to be tested for absorption and photon-darkening effects at these lower wavelengths.

7.2 Optimization of Supercontinuum (SC) Generation

Both the spectral quality and power level of a supercontinuum (SC) source is critical for making an on-chip tunable laser. The third order susceptibility ($\chi^{(3)}$) of Ta_2O_5 was characterized by analyzing THG in chapter 4, which gives the value of nonlinear coefficient (n_2). This enables us to investigate, and predict the relative contributions

from self-phase modulation (SPM) and four-wave mixing (FWM) effects in the waveguide output spectra.

It is also possible to optimize $\chi^{(3)}$ effects by adjusting the GVD of waveguides to produce the optimum supercontinuum spectra in the femtosecond regime. The GVD properties of the waveguides are currently obtained from software simulations (the subject of chapter 3). To experimentally characterize the GVD properties of nano-wire waveguides requires the use of measurement techniques such as time-of-flight [94, 106, 107] or auto-correlation [108, 109] methods. Further possibilities include utilizing FWM and XPM to generate extra frequency components and SPM to produce wider and smoother spectrum (as shown in section 5.1.1). This could be done in practice by using tapered nano-wire waveguides to increase the coupled pump intensity, and careful selection of waveguide dimensions with respect to working wavelength. Alternatively, photonic crystal structures could be employed to improve the SC outputs.

An alternative possibility is to manipulate the pulse duration within the PLC chip itself (i.e. apply pulse compression) to remove the need for a complex and expensive external femtosecond pump laser, and move to a cheaper picosecond or nanosecond pump. Pulse compression can realistically be achieved by incorporating highly dispersive photonic crystal waveguides, (i.e. use +ve or -ve dispersion introduced by an appropriately designed line defect waveguide fabricated from a nonlinear material as the Laser cavity [110-112]) in which case (providing similar results as presented in chapters 4 and 5 are obtainable) very cheap solid state laser and OCT sources could evolve from this project using a VECSEL [113] (Vertical-External Cavity Surface-Emitting Lasers), also known as semiconductor disk laser (SDL), pump source instead of prism compression with bulk optics [114].

Figure 70 [113] illustrates the operating mechanism of a VECSEL laser. Utilizing the well designed quantum well structures to provide low-divergence, circular, near-diffraction-limited, high quality mode output with a wide gain bandwidth and excellent thermal properties. The VECSEL also allows manipulation of the laser output, for example, an external cavity semiconductor saturable absorber mirror

(SESAM) could be used to give a train of short pulses in the laser output [113]. The VECSEL has been widely reported working in nanoseconds, picoseconds, and femtoseconds regimes [115-117]. With the recent development in VECSEL, a peak power of around 337 W/pulse with 1 GHz repetition rate, 120 mW average power, and 335 fs pulse duration can be achieved from VECSEL for the state of the art [116].

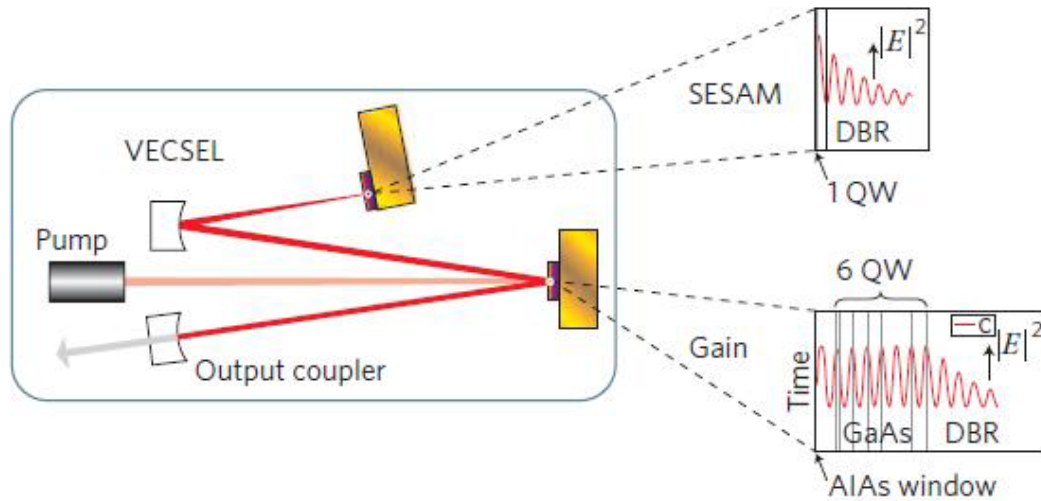


Figure 70: Illustration of the generation mechanism of VECSEL lasers [113]

Provided the fabrication process can be improved to reduce the loss to less than -4 dB/cm in waveguide samples, it should be possible to achieve similar SC generation results as those presented in chapter 5, by using a femtosecond VECSEL as the pump source in conjunction with nanowire waveguides with cross-section of 200 by 100 nm.

7.3 Optimization of Optical Parametric Conversions – Viability of Low Cost Fully Integrated On-Chip Tunable Laser

As explained in the previous two sections, by shrinking the waveguide dimensions, integrating photonic crystal components into the waveguides, and pumping using a compact low cost femtosecond pump source, (such as a VECSEL), it could be possible to create a high performance, low cost integrated ‘on-chip’ nonlinear tunable laser device that could be useful for many optical applications.

By utilizing a state of the art VECSEL device as a pump source [116, 118, 119], reducing the cross-section of the waveguides down to 100 nm by 200 nm, and reducing waveguide loss to -4 dB, the peak power of both pump and seed pulses can match a similar level to that used in experiments in chapter 6 (and so produce similar parametric output). Hence it is technically feasible to fabricate a compact low cost on-chip tunable laser device using the principles investigated in this thesis.

Similar waveguide dimensions also satisfy the requirements for producing SC as stated in section 7.2. The photonic crystal structures could also be embedded into the waveguides to further improve the intensities (optical power densities), and provide phase-matching environment between pump and seed pulses.

Based on discussions so far, an on-chip tunable laser could work in the following way: The chip could be divided into 2 regions: an input region with initial nonlinear optical processing, and a wavelength tuning region with output. The input region sub-component consists of waveguides that magnify the pump power, and produce SC generation (to act as a seed) after splitting the energy from one source into two parts. The energy could be split evenly (or by certain percentage depending on the design). The wavelength tuning with output sub-component of the chip will guide pump and seed beams into one single waveguide that provides the phase-matching environment for the parametric conversion to work. With the fixed delay provided by the photonic crystal waveguide embedded in the tuning sub-component, the wavelength tuning (in concept) could be achieved by modifying the waveguide length through metal contact embedded in the device acting as a localized heater. Parametric output beam from the tunable laser is then coupled out through another photonic crystal waveguide, whilst maintaining good mode profiles, and minimizing losses (see fig. 71). The detailed benefits of using photonic crystal embedded inside the waveguides are outlined in the next section.

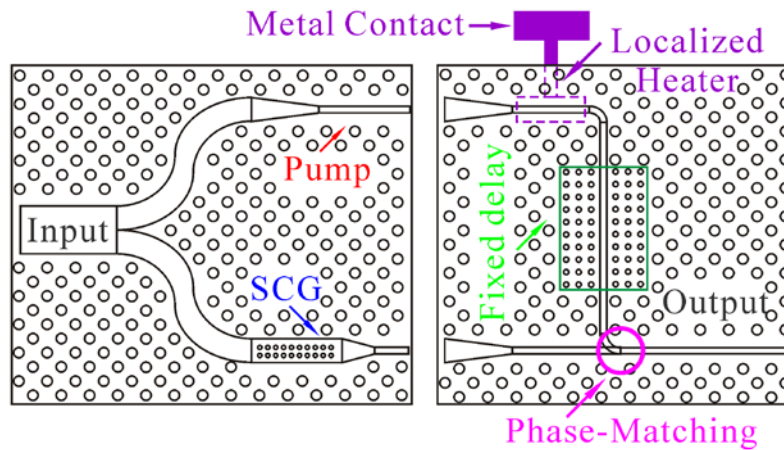


Figure 71: Concept design for on-chip tunable laser using planar photonic crystal waveguide technique

7.4 Photonic Crystal Structures Designs

The next part of the project revolves around investigating the beneficial effects of incorporating photonic crystals into nonlinear waveguides, in terms of solving limiting factors for the input of the device using a low power pump source in planar waveguides.

Introduction of photonic crystals allows several possibilities:

1) Multiple ZDW devices:

According to the results of multiple ZDW PCFs (presented in chapter 1), we would expect a wider SC with relatively good flatness at lower pulse power if similar designs were adopted for a planar device. However, it might also introduce more spectral noise than single ZDW devices in the mean time. Figure 72 shows there are 4 ZDWs for the waveguide with embedded photonic crystal.

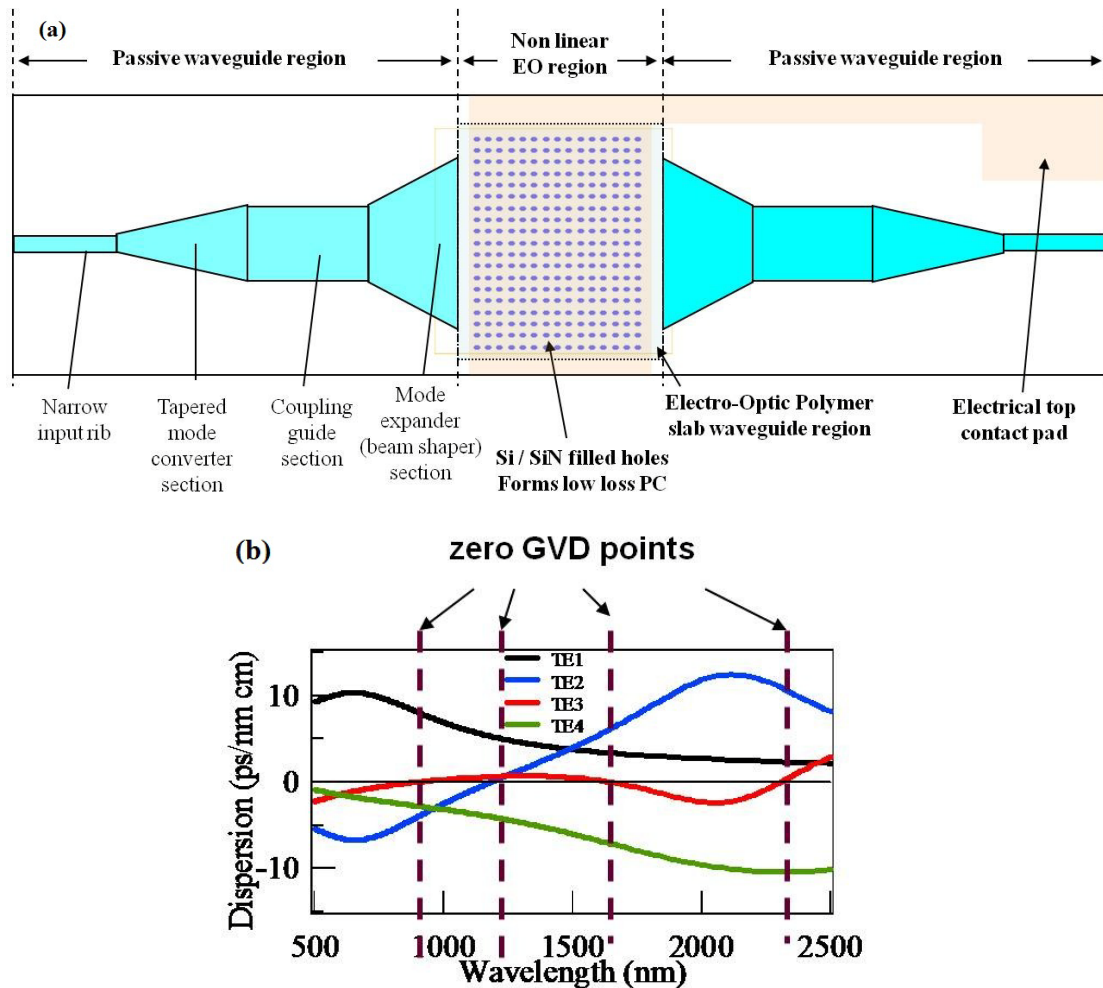


Figure 72: (a) Photonic crystal slab waveguide, and (b) Waveguide dispersion properties for 4 TE modes

2) Pulse-width manipulation:

Similar to the examples explained in [120] and [121] using grating structures, dispersive properties of photonic crystals provide a method to manipulate the pump pulse characteristics allowing on-chip pulse compression or expansion.

3) Phase-matching manipulation:

Photonic crystals may allow interesting sum and difference frequency generation effects to occur in nonlinear waveguides through parametric wavelength conversion. These would be reliant upon directional phase-matching effects within the crystal structures and could lead to single wavelength tunability by simply adjusting the incidence beam direction (fig. 73). The band diagram of a rectangular photonic crystal lattice is shown in figure 74. Effects of photonic crystal devices on sum and

difference frequency generation could be examined via angular reflectometry and in-plane coupling using pulsed pump sources on currently available samples as follows:

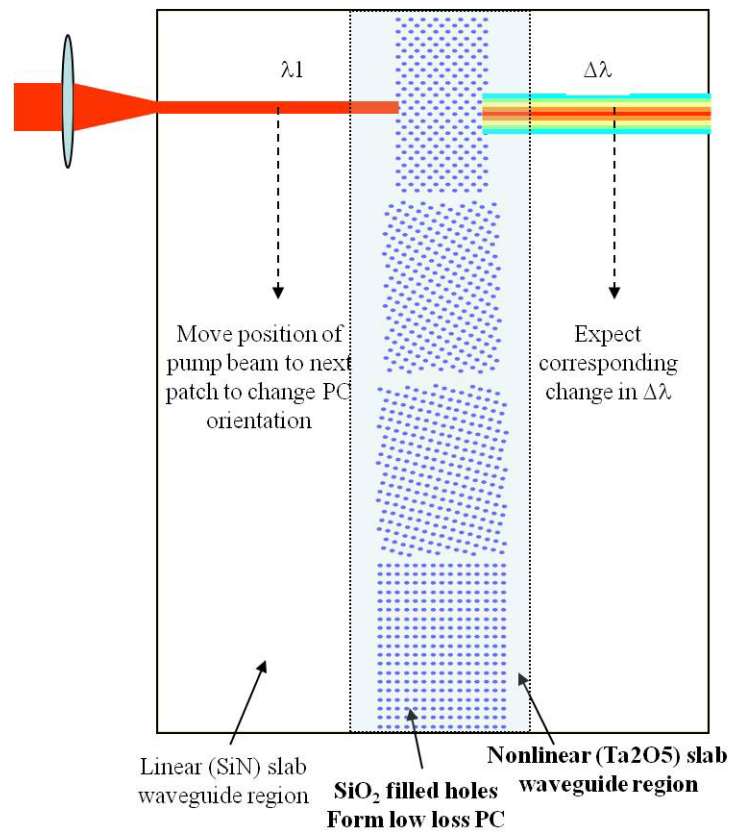


Figure 73: Setup for examining directional phase-matching effects and wavelength tuning within the crystal structures by adjusting the incidence beam direction

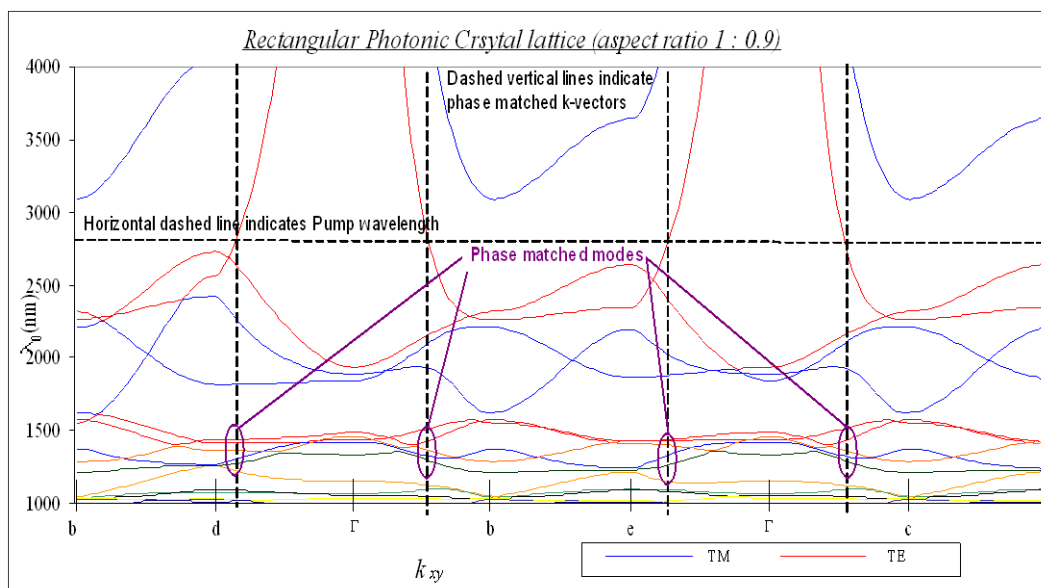


Figure 74: Band diagram of a rectangular photonic crystal lattice

Experiments should start by investigating dispersive properties, and parametric wavelength conversion effects in gratings and 2D PC lattices etched into the Ta_2O_5 waveguide cores using spectroscopic angular surface reflectometry (see fig. 75). In this case for simple dispersion measurements low power white light is coupled into the device from the top surface via leaky modes and wavelength spectra of leaky modes (which can be measured in reflection by a fibre probe) and confined guided modes (which can be seen as a line across the slab waveguide, via a colour camera mapped). Dispersive properties of the PCs can also be temporally resolved by transmission spectroscopy using end-fire coupled white light.

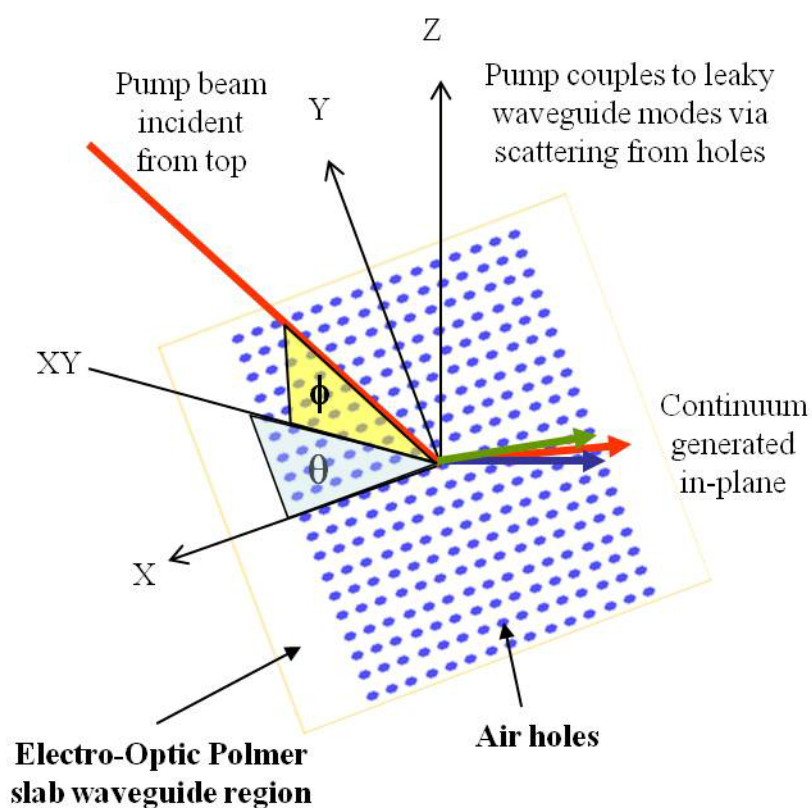


Figure 75: Spectroscopic angular surface reflectometry beam coupling via leaky modes to investigate phase-matching in PC

Once PC dispersion has been experimentally mapped and validated against theoretical band-structure, the low power white light pump source is replaced by a high power pulsed source, and the experiments repeated. This time angular reflectometry will map parametric wavelength conversion as a function of incidence angle – which in

turn relates to specific coupled Bloch mode (or dispersion band) in the PC structure. Newly generated parametrically converted modes will either couple to free space reflected beams via scattering to leaky modes (which can be mapped by a fibre probe), or will propagate as confined modes within the PC slab waveguide as coloured beams (which could be viewed by a colour camera from above). In this case, the direction of converted beams can also be mapped, giving further information about Bloch mode coupling within the PC (see fig. 75). This experiment would give full information relating to angle tuned phase-matching condition for parametric wavelength conversion in a nonlinear PC device.

A second set of experiments should study the temporal modification of the pump pulse by the PC, and determine the effect of adjusting the ZDW of the waveguides (which in turn depends on the dispersion of the particular Bloch mode to which the pump is coupled in the PC) as well as the requirements for pump power and pulse-width characteristics for generating SC (this can be done using the current transmission setup used in chapter 5). It is expected that the PC will allow greater range of control over ZDW than can be achieved by a nano-wire waveguide alone.

7.5 Computational Modelling of Photonic Crystal devices

For the purpose of investigating the photonic crystal (PC) designs, the photonic bandgap associated with different lattice patterns (geometries) must be simulated to provide a reference for device fabrication. Current experimental results show two simultaneous signals (SC generation and THG) generated inside one waveguide by the same pump. The modelling should be extended to incorporate the nonlinearity of the waveguide material (as determined by the experiment chapter 4) to investigate temporal effect of the PC structures on the input pulse. For example, to investigate the effect of pulse chirp in various PC designs in comparison to transform limited pulses.

Finite difference time domain (FDTD) [14] modelling techniques could be used for the investigation of evolution of SPM in PC structures for a transform limited input pulse propagating in a nonlinear waveguide. As the photonic crystal leads to ‘slow light’, and increased strength of nonlinear interactions, FDTD should be considerably

more practical for modelling nonlinear effects in PC devices than normal planar waveguide discussed in chapter 3. By varying the pump wavelength, incident angles, or lattice geometry, we would expect to observe in theory how complex optical effects such as FWM and XPM evolve in different PC structures. This would provide a base line for designing appropriate PC structures, and is helpful for analyzing experimental results even further.

It will be necessary to investigate the output spectrum as a function of spatial position within the PC structure and input pulse power. The setup of these simulations requires modelling pulse propagation inside the PC structures without incorporating the nonlinearity or other waveguide characteristics to provide a reference for comparison. Currently, elementary simulations are performed to observe the photonic bandgaps in order to build up more complex simulations for obtaining the theoretical model of photonic crystal structures. It is also useful to simulate the device with incorporation of different materials and patterns on the same wafer. This will provide design reference for on-chip tunable lasers.

By designing the waveguides or photonic crystal properly and processing different materials on the same wafer, it is possible to make the wave mixing or spatially separate the two different outputs on the same chip (for example, by encouraging coupling to different angularly scattered Bloch modes, or by use of line defect waveguide circuits). Then the on-chip tunable laser system will be feasible with the improved SC generation and pump signals.

Chapter 8 Conclusions

The development of planar waveguide technology has demonstrated great potential for creating an on-chip tunable laser system as both supercontinuum (SC) generation and parametric effects can be produced within a single waveguide. The characteristics of the SC suggest that it is capable to be used in many applications, including as the essential components for on-chip tunable lasers. The potential to integrate planar waveguides using modern nano-fabrication methods makes the laser system in planar waveguides very interesting and valuable. The physical effects, related to parametric conversion and SC, are reviewed in this thesis based on the research works done previously for optical (photonic crystal) fibres. It shows that the linear dispersion effect is always accompanied by the nonlinear optical effects during the formation of SC. The resulting SC depends on various factors including: input pulse duration, input power, input pulse wavelength, dispersion properties of the optical guides, nonlinear characteristics of the core materials, and the geometries of the optical guides. Then, the theoretical and experimental observations of the dispersion properties of the planar waveguides are demonstrated in this thesis, which provide the reference point for future simulations and experiments.

This thesis shows the experimental results of THG effects, SC generation, and parametric effects generated on a single rib waveguide with femtosecond pulsed laser. The third-order susceptibilities at wavelength range of 1470 – 1610 nm of Ta_2O_5 waveguides are derived from THG results. The derived values are in good agreement with values obtained in previous work using the SPM effect. The SC results show up to ~200 nm pulse broadening are also presented in the thesis, which provides the desired information for researching the nonlinear properties of Ta_2O_5 waveguides for

further optimization of the device output. The parametric effects showed two-way frequency conversions, from high- to low-energy and low- to high-energy, with amplification to the seed inputs. Further optimization steps are suggested for archiving the high efficiency wavelength conversion with the planar waveguide for tuning functions.

The other major motivation of the project is to have the SC generation embedded with other sub-systems into a single chip, which can be used for potential applications not only for on-chip tunable lasers, but also for sensors and bio-devices. The small device size and the ease of fabrication also make the project attractive in terms of the costs reduction for the products. For the next step, this project will not only be limited to on-chip tunable laser system designs. One of the possible extensions of the project is to provide light source for self-integrated dual-band OCT systems.

Appendix A: Tantalum Pentoxide and Titanium Dioxide Material Dispersion – Equations & Parameters

Refractive index calculations for Ta_2O_5 and TiO_2 [62], i.e. material dispersion calculations:

$$E(\lambda) = \frac{1.2395086}{\lambda}$$

$$\varepsilon_1(E) = \varepsilon_1(\infty) + \frac{1}{2} \frac{A}{\pi} \frac{C}{\zeta^4} \frac{a_{\ln}}{\alpha E_0} \ln \left[\frac{(E_0^2 + E_g^2 + \alpha E_g)}{(E_0^2 + E_g^2 - \alpha E_g)} \right] - \frac{A}{\pi \zeta^4} \frac{a_{\tan}}{E_0} \left[\pi - \tan^{-1} \left(\frac{2E_g + \alpha}{C} \right) \right. \\ \left. + \tan^{-1} \left(\frac{-2E_g + \alpha}{C} \right) \right] + 2 \frac{AE_0}{\pi \zeta^4 \alpha} \left\{ E_g (E^2 - \gamma^2) \left[\pi + 2 \tan^{-1} \left(\frac{2\gamma^2 - 2E_g^2}{\alpha \cdot C} \right) \right] \right\} \\ - \frac{AE_0 C}{\pi \zeta^4} \frac{E^2 + E_g^2}{E} \ln \left(\frac{|E - E_g|}{E + E_g} \right) + 2 \frac{AE_0 C}{\pi \zeta^4} E_g \ln \left[\frac{|E - E_g|(E + E_g)}{\sqrt{(E_0^2 - E_g^2)^2 + E_g^2 C^2}} \right]$$

where $a_{\ln} = (E_g^2 - E_0^2)E^2 + E_g^2 C^2 - E_0^2(E_0^2 + 3E_g^2)$,

$$a_{\tan} = (E^2 - E_0^2)(E_0^2 + E_g^2) + E_g^2 C^2,$$

$$\zeta^4 = (E^2 - \gamma^2)^2 + \frac{\alpha^2 C^2}{4},$$

$$\alpha = \sqrt{4E_0^2 - C^2},$$

$$\gamma = \sqrt{E_0^2 - C^2/2}.$$

$$\varepsilon_2(E) = \begin{cases} \left[\frac{AE_0 C (E - E_g)^2}{(E^2 - E_0^2)^2 + C^2 E^3} \cdot \frac{1}{E} \right] & E > E_g \\ 0 & E \leq E_g \end{cases}$$

$$n_{\text{Re}}(E) = \sqrt{\varepsilon_1(E)}$$

$$n_{\text{Im}}(E) = \sqrt{\varepsilon_2(E)}$$

Table 4: Fitting Parameters for Ta₂O₅ and TiO₂ Material Dispersion [63]

Fitting Parameters	Ta ₂ O ₅	TiO ₂
$\varepsilon_1(\infty)$	2.23 ± 0.05	2.19 ± 0.03
E_g [eV]	4.04 ± 0.02	3.26 ± 0.01
A	174.7 ± 6.5	247.6 ± 5.9
E_0 [eV]	5.35 ± 0.02	4.13 ± 0.02
C	1.69 ± 0.06	1.86 ± 0.03

Appendix B: Silicon Dioxide Material

Dispersion – Sellmeier Equation

Refractive index calculations for SiO_2 [14] can be well matched by the Sellmeier equation:

$$n(\lambda) = \sqrt{1 + \sum_{i=1}^3 \frac{a_i \lambda^2}{(\lambda^2 - b_i)}} \quad (\lambda : \mu m)$$

where a_i 's and b_i 's are Sellmeier coefficients. Table 5 shows the Sellmeier coefficients of pure and dope silica glasses [15].

Table 5: Sellmeier coefficients of pure and doped silica glasses [15]

Dopant (mole%)	Pure SiO_2	GeO_2 (6.3)	GeO_2 (19.3)	B_2O_3 (5.2)	P_2O_5 (10.5)
a_1	0.6961663	0.7083952	0.7347008	0.6910021	0.7058489
a_2	0.4079426	0.4203993	0.4461191	0.4022430	0.4176021
a_3	0.8974794	0.8663412	0.8081698	0.9439644	0.8952753
b_1	0.004679148	0.007290464	0.005847345	0.004981838	0.005202431
b_2	0.01351206	0.01050294	0.01552717	0.01375664	0.01287730
b_3	97.93400	97.93428	97.93484	97.93353	97.93401

Appendix C: Tellurite Material Dispersion

Refractive index calculations for TeO_2 can be well matched by the Cauchy optical equation [64]:

$$n(\lambda) = A + \frac{B}{\lambda^2} + \frac{C}{\lambda^4} \quad (\lambda : \mu m)$$

Table 6 shows the Cauchy parameters for TeO_x samples [64].

Table 6: Cauchy parameters for TeO_x [64]

x	A	B (μm^2)	C (μm^4)
2.0	2.0559	0.03393	—
2.04	2.0407	0.02791	0.00808
2.17	1.9943	0.01908	0.00188
2.18	1.9783	0.01926	0.00199
2.22	2.0026	0.01843	0.00215
2.33	1.9625	0.01808	0.00207
2.38	1.9719	0.01891	0.00201
2.42	1.9634	0.01589	0.00199
2.50	1.9693	0.02821	—
2.57	1.9660	0.01949	0.00163
2.65	1.9445	0.01995	0.00160
2.75	1.9278	0.01823	0.00192

Appendix D: Finite-Difference Time-Domain (FDTD) Method

FDTD [68] is a grid-based differential time-domain numerical modeling method. The time-dependent Maxwell's equations (in partial differential form) are discretized using central-difference approximations to the space and time partial derivatives. The resulting finite-difference equations are solved in either software or hardware in a leapfrog manner: the electric field vector components in a volume of space are solved at a given instant in time; then the magnetic field vector components in the same spatial volume are solved at the next instant in time; and the process is repeated over and over again until the desired transient or steady-state electromagnetic field behavior is fully evolved.

The advantages of FDTD include:

- FDTD is a time-domain technique, and when a broadband pulse (such as a Gaussian pulse) is used as the source, then the response of the system over a wide range of frequencies can be obtained with a single simulation. This is useful in applications where resonant frequencies are not exactly known, or anytime that a broadband result is desired.
- Since FDTD calculates the E and H fields everywhere in the computational domain as they evolve in time, it lends itself to providing animated displays of the electromagnetic field movement through the model. This type of display is useful in understanding what is going on in the model, and to help ensure that the model is working correctly.
- The FDTD technique allows the user to specify the material at all points within the computational domain. A wide variety of linear and nonlinear dielectric and magnetic materials can be naturally and easily modeled.

- FDTD allows the effects of apertures to be determined directly. Shielding effects can be found, and the fields both inside and outside a structure can be found directly or indirectly.
- FDTD uses the E and H fields directly. Since most EMI/EMC modeling applications are interested in the E and H fields, it is convenient that no conversions must be made after the simulation has run to get these values.

The disadvantages of FDTD are:

- Since FDTD requires that the entire computational domain be gridded, and the grid spatial discretization must be sufficiently fine to resolve both the smallest electromagnetic wavelength and the smallest geometrical feature in the model, very large computational domains can be developed, which results in very long solution times. Models with long, thin features, (like wires) are difficult to model in FDTD because of the excessively large computational domain required.
- FDTD finds the E/H fields directly everywhere in the computational domain. If the field values at some distance are desired, it is likely that this distance will force the computational domain to be excessively large. Far-field extensions are available for FDTD, but require some amount of postprocessing.
- Since FDTD simulations calculate the E and H fields at all points within the computational domain, the computational domain must be finite to permit its residence in the computer memory. In many cases this is achieved by inserting artificial boundaries into the simulation space. Care must be taken to minimize errors introduced by such boundaries. There are a number of available highly effective absorbing boundary conditions (ABCs) to simulate an infinite unbounded computational domain. Most modern FDTD implementations instead use a special absorbing "material", called a perfectly matched layer (PML) to implement absorbing boundaries.

- Because FDTD is solved by propagating the fields forward in the time domain, the electromagnetic time response of the medium must be modeled explicitly. For an arbitrary response, this involves a computationally expensive time convolution, although in most cases the time response of the medium (or Dispersion (optics)) can be adequately and simply modeled using either the recursive convolution (RC) technique, the auxiliary differential equation (ADE) technique, or the Z-transform technique. An alternative way of solving Maxwell's equations that can treat arbitrary dispersion easily is the Pseudospectral Spatial-Domain method (PSSD), which instead propagates the fields forward in space.

Appendix E: SC Output Spectra

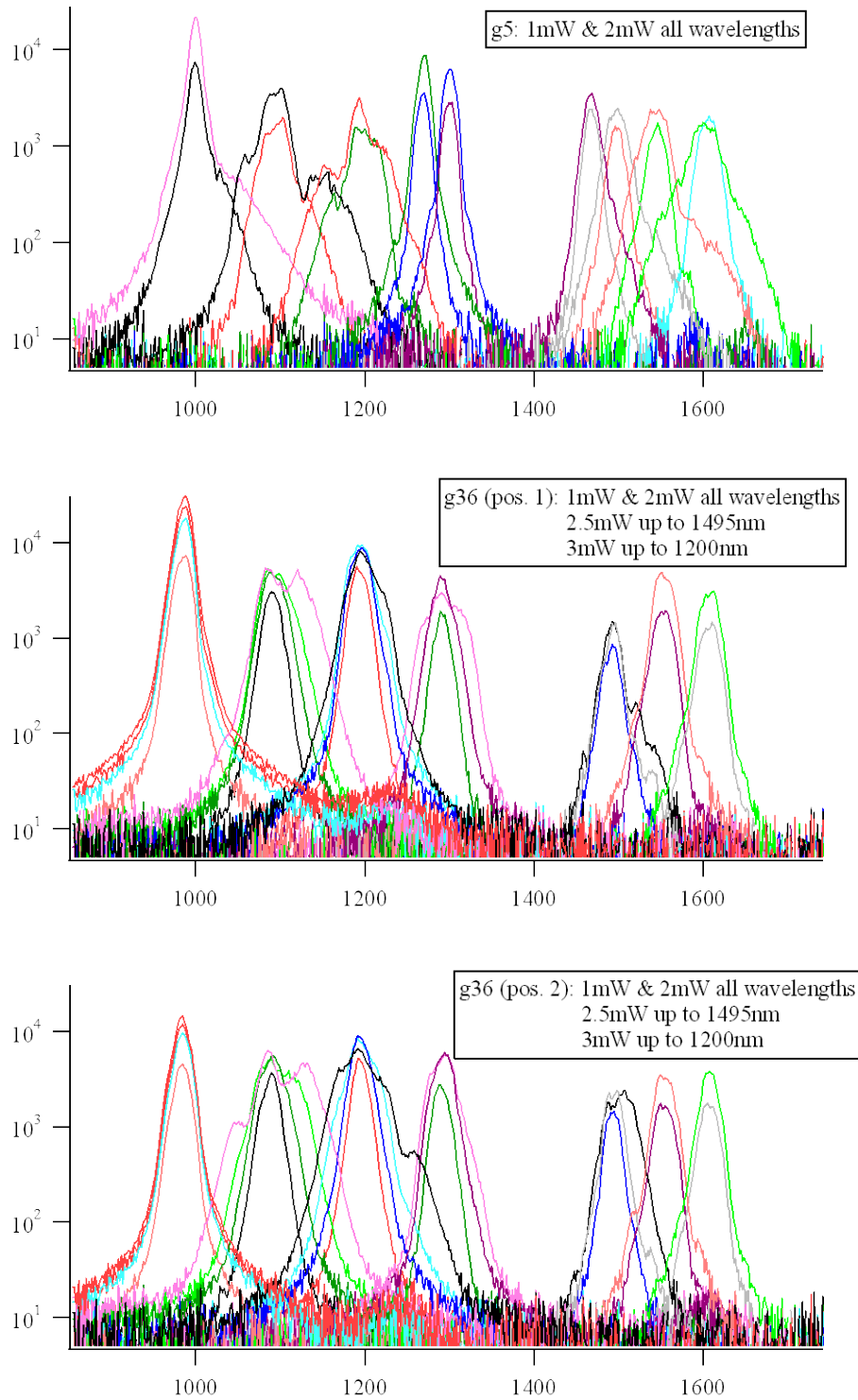


Figure 76: Output spectra with pump wavelength range of 1000 – 1610 nm

References

- [1] M. K. Reed, *et al.*, “Widely Tunable Femtosecond Optical Parametric-Amplifier at 250-kHz with a Ti-Sapphire Regenerative Amplifier,” *Optics Letters*, vol. 19, pp. 1855-1857, Nov 15 1994.
- [2] J. G. Haub, *et al.*, “Bandwidth Characteristics of a Pulsed Optical Parametric Oscillator - Application to Degenerate 4-Wave-Mixing Spectroscopy,” *Optics Letters*, vol. 20, pp. 1637-1639, Aug 1 1995.
- [3] G. P. Agrawal, *Nonlinear fiber optics*, 4th ed. Amsterdam; London: Elsevier/Academic Press, 2007.
- [4] R. W. Boyd, *Nonlinear optics*, 3rd ed. London: Academic, 2008.
- [5] A. Bassi, *et al.*, “Time-resolved spectrophotometer for turbid media based on supercontinuum generation in a photonic crystal fiber,” *Optics Letters*, vol. 29, pp. 2405-2407, 2004.
- [6] K. P. Hansen, “Introduction to nonlinear photonic crystal fibers,” *Journal of Optical and Fiber communications Reports*, vol. 2, pp. 226-254, 2005.
- [7] T. Udem, *et al.*, “Optical frequency metrology,” *Nature*, vol. 416, pp. 233-237, 2002.
- [8] I. Hartl, *et al.*, “Ultrahigh-resolution optical coherence tomography using continuum generation in an air silica microstructure optical fiber,” *Optics Letters*, vol. 26, pp. 608-610, 2001.
- [9] A. V. Husakou and J. Herrmann, “Supercontinuum generation, four-wave mixing, and fission of higher-order solitons in photonic-crystal fibers,” *Journal of the Optical Society of America B-Optical Physics*, vol. 19, pp. 2171-2182, Sep 2002.

- [10] M. Laroche, *et al.*, “Compact sub-nanosecond wideband laser source for biological applications,” *Applied Physics B: Laser and Optics*, vol. 86, pp. 601-604, 2007.
- [11] J. M. Dudley, *et al.*, “Supercontinuum generation in photonic crystal fiber,” *Reviews of Modern Physics*, vol. 78, pp. 1135-1184, Oct-Dec 2006.
- [12] C. M. Netti, *et al.*, “Octave-wide continuum generation in high-index planar waveguide by 1.5 μ m femtosecond pump,” in *Commercial and Biomedical Applications of Ultrafast Lasers V*, San Jose, CA, USA, 2005, pp. 195-199.
- [13] O. Fedotova, *et al.*, “Supercontinuum generation in planar rib waveguides enabled by anomalous dispersion,” *Optics Express*, vol. 14, pp. 1512-1517, 2006.
- [14] K. Okamoto, *Fundamentals of optical waveguides*, 2nd ed. Burlington, Mass. ; London: Academic Press, 2006.
- [15] A. K. Ghatak and K. Thyagarajan, *An introduction to fiber optics*. Cambridge; New York: Cambridge University Press, 1998.
- [16] J. Toulouse, “Optical nonlinearities in fibers: Review, recent examples, and systems applications,” *Journal of Lightwave Technology*, vol. 23, pp. 3625-3641, 2005.
- [17] D. Mohanta and A. Choudhury, “Measurement of third order susceptibility by nonresonant nondegenerate four wave mixing in polymer embedded cadmium sulfide quantum dot systems,” *Optical Materials*, vol. 29, pp. 342-347, 2006.
- [18] W. Kaiser, *Ultrashort laser pulses and applications*. Berlin: Springer, 1988.
- [19] A. Yariv, *Quantum electronics*, 3rd ed. ed. New York: Wiley, 1989.
- [20] J. E. Sharping, *et al.*, “Optical parametric oscillator based on four-wave mixing in microstructure fiber,” *Optics Letters*, vol. 27, pp. 1675-1677, Oct 1 2002.
- [21] T. Sloanes, *et al.*, “Optimisation of high average power optical parametric generation using a photonic crystal fiber,” *Optics Express*, vol. 16, pp. 19724-19733, Nov 24 2008.
- [22] D. Kip and E. Kratzig, “Anisotropic 4-Wave-Mixing in Planar LiNbO₃ Optical Wave-Guides,” *Optics Letters*, vol. 17, pp. 1563-1565, Nov 15 1992.

- [23] K. Yamada, *et al.*, “All-optical efficient wavelength conversion using silicon photonic wire waveguide,” *IEEE Photonics Technology Letters*, vol. 18, pp. 1046-1048, May-Jun 2006.
- [24] M. A. Foster, *et al.*, “Broad-band optical parametric gain on a silicon photonic chip,” *Nature*, vol. 441, pp. 960-963, Jun 22 2006.
- [25] M. D. Pelusi, *et al.*, “Ultra-high Nonlinear As₂S₃ planar waveguide for 160-Gb/s optical time-division demultiplexing by four-wave mixing,” *IEEE Photonics Technology Letters*, vol. 19, pp. 1496-1498, Sep-Oct 2007.
- [26] M. D. Pelusi, *et al.*, “Applications of highly-nonlinear chalcogenide glass devices tailored for high-speed all-optical signal processing,” *IEEE Journal of Selected Topics in Quantum Electronics*, vol. 14, pp. 529-539, May-Jun 2008.
- [27] M. R. E. Lamont, *et al.*, “Net-gain from a parametric amplifier on a chalcogenide optical chip,” *Optics Express*, vol. 16, pp. 20374-20381, Dec 8 2008.
- [28] F. Luan, *et al.*, “Dispersion engineered As₂S₃ planar waveguides for broadband four-wave mixing based wavelength conversion of 40 Gb/s signals,” *Optics Express*, vol. 17, pp. 3514-3520, Mar 2 2009.
- [29] M. D. Pelusi, *et al.*, “Wavelength Conversion of High-Speed Phase and Intensity Modulated Signals Using a Highly Nonlinear Chalcogenide Glass Chip,” *IEEE Photonics Technology Letters*, vol. 22, pp. 3-5, Jan 1 2010.
- [30] J. Van Erps, *et al.*, “High-Resolution Optical Sampling of 640-Gb/s Data Using Four-Wave Mixing in Dispersion-Engineered Highly Nonlinear As₂S₃ Planar Waveguides,” *Journal of Lightwave Technology*, vol. 28, pp. 209-215, Jan 15 2010.
- [31] (2010, 18 Dec. 2010). *Optical parametric amplifier*. Available: http://en.wikipedia.org/wiki/Optical_parametric_amplifier
- [32] R. Paschotta. (2008, 18 Dec. 2010). *Optical Parametric Amplifiers*. Available: http://www.rp-photonics.com/optical_parametric_amplifiers.html
- [33] A. F. Fercher, “Optical coherence tomography - development, principles, applications,” *Zeitschrift für Medizinische Physik*, vol. 20, pp. 251-276, 2010.
- [34] J. M. Dudley, “Supercontinuum Generation in Photonic Crystal Fiber,” Seminar Presentation, 2007 seminar series of Optical Research Centre, University of Southampton, 2007, unpublished.

- [35] B.-E. Olsson and D. J. Blumenthal, "Pulse restoration by filtering of self-phase modulation broadened optical spectrum," *Journal of Lightwave Technology*, vol. 20, pp. 1113-1117, 2002.
- [36] S. Shen, *et al.*, "Effects of self-phase modulation on sub-500 fs pulse transmission over dispersion compensated fiber links," *Journal of Lightwave Technology*, vol. 17, pp. 452-461, 1999.
- [37] G. Steinmeyer and G. Stibenz, "Generation of sub-4-fs pulses via compression of a white-light continuum using only chirped mirrors," *Applied Physics B: Laser and Optics*, vol. 82, pp. 175-181, 2006.
- [38] M. Nisoli, *et al.*, "Generation of high energy 10 fs pulses by a new pulse compression technique," *Applied Physics Letters*, vol. 68, pp. 2793-2795, 1996.
- [39] R. L. Fork, *et al.*, "Negative dispersion using pairs of prisms," *Opt. Lett.*, vol. 9, pp. 150-152, 1984.
- [40] T. Nakasyotani, *et al.*, "Wavelength-Division-Multiplexed Millimeter-Waveband Radio-on-Fiber System Using a Supercontinuum Light Source," *J. Lightwave Technol.*, vol. 24, p. 404, 2006.
- [41] R. Stegeman, *et al.*, "Tellurite glasses with peak absolute Raman gain coefficients up to 30 times that of fused silica," *Optics Letters*, vol. 28, pp. 1126-1128, 2003.
- [42] P. A. Thielen, *et al.*, "Small-core As-Se fiber for Raman amplification," *Optics Letters*, vol. 28, pp. 1406-1408, 2003.
- [43] R. Zhang, *et al.*, "Theoretical design of a liquid-core photonic crystal fiber for supercontinuum generation," *Optics Express*, vol. 14, pp. 6800-6812, 2006.
- [44] R. H. Stolen, *et al.*, "Development of the stimulated Raman spectrum in single-mode silica fibers," *Journal of the Optical Society of America B*, vol. 1, pp. 652-657, 1984.
- [45] P. Baldeck and R. Alfano, "Intensity effects on the stimulated four photon spectra generated by picosecond pulses in optical fibers," *Journal of Lightwave Technology*, vol. 5, pp. 1712-1715, 1987.
- [46] I. Ilev, *et al.*, "Highly efficient wideband continuum generation in a single-mode optical fiber by powerful broadband laser pumping," *Applied Optics*, vol. 35, pp. 2548-2553, 1996.

- [47] A. Hasegawa and F. Tappert, "Transmission of stationary nonlinear optical pulses in dispersive dielectric fibers. I. Anomalous dispersion," *Applied Physics Letters*, vol. 23, pp. 142-144, 1973.
- [48] Y. Kodama and A. Hasegawa, "Nonlinear pulse propagation in a monomode dielectric guide," *IEEE Journal of Quantum Electronics*, vol. 23, pp. 510-524, 1987.
- [49] S. Leon-Saval, *et al.*, "Supercontinuum generation in submicron fibre waveguides," *Optics Express*, vol. 12, pp. 2864-2869, 2004.
- [50] C. M. B. Cordeiro, *et al.*, "Engineering the dispersion of tapered fibers for supercontinuum generation with a 1064 nm pump laser," *Optics Letters*, vol. 30, pp. 1980-1982, 2005.
- [51] T. A. Birks, *et al.*, "Supercontinuum generation in tapered fibers," *Optics Letters*, vol. 25, pp. 1415-1417, 2000.
- [52] J. Cascante-Vindas, *et al.*, "Tapering photonic crystal fibres for supercontinuum generation with nanosecond pulses at 532nm," *Optics Communications*, vol. 281, pp. 433-438, 2008.
- [53] J. C. Knight, *et al.*, "All-silica single-mode optical fiber with photonic crystal cladding," *Optics Letters*, vol. 21, pp. 1547-1549, 1996.
- [54] S. Coen, *et al.*, "White-light supercontinuum generation with 60-ps pump pulses in a photonic crystal fiber," *Optics Letters*, vol. 26, pp. 1356-1358, 2001.
- [55] A. K. Abeeluck, *et al.*, "High-power supercontinuum generation in highly nonlinear, dispersion-shifted fibers by use of a continuous-wave Raman fiber laser," *Optics Letters*, vol. 29, pp. 2163-2165, 2004.
- [56] J. K. Ranka, *et al.*, "Visible continuum generation in air silica microstructure optical fibers with anomalous dispersion at 800nm," *Optics Letters*, vol. 25, pp. 25-27, 2000.
- [57] P. Domachuk, *et al.*, "Over 4000 nm bandwidth of mid-IR supercontinuum generation in sub-centimeter segments of highly nonlinear tellurite PCFs," *Optics Express*, vol. 16, pp. 7161-7168, May 2008.
- [58] P.-A. Champert, *et al.*, "White-light supercontinuum generation in normally dispersive optical fiber using original multi-wavelength pumping system," *Optics Express*, vol. 12, pp. 4366-4371, 2004.

- [59] F. Bahloul, *et al.*, “Supercontinuum generation in microstructure optical fiber with two zero dispersion wavelengths,” in *Proceedings of IEEE/LEOS Workshop on Fibres and Optical Passive Components*, 22-24 June 2005, pp. 32-35.
- [60] L. De Boni, *et al.*, “Pump polarization-state preservation of picosecond generated white-light supercontinuum,” *Optics Express*, vol. 16, pp. 957-964, Jan 2008.
- [61] M. Lehtonen, *et al.*, “Supercontinuum generation in a highly birefringent microstructured fiber,” *Applied Physics Letters*, vol. 82, pp. 2197-2199, 2003.
- [62] G. E. Jellison and F. A. Modine, “Parameterization of the optical functions of amorphous materials in the interband region,” *Applied Physics Letters*, vol. 69, pp. 371-373, 1996.
- [63] K. Postava, *et al.*, “Spectroellipsometric characterization of materials for multilayer coatings,” *Applied Surface Science*, vol. 175-176, pp. 276-280, 2001.
- [64] S. M. Pietralunga, *et al.*, “Optical properties of reactively sputtered TeO_x amorphous films,” *Applied Optics*, vol. 44, pp. 534-537, 2005.
- [65] C. Y. Tai, *et al.*, “Determination of nonlinear refractive index in a Ta₂O₅ rib waveguide using self-phase modulation,” *Optics Express*, vol. 12, pp. 5110-5116, 2004.
- [66] S. G. Johnson and J. D. Joannopoulos, *Photonic crystals: the road from theory to practice*. Boston, Mass.; London: Kluwer Academic Publishers, 2002.
- [67] (2010, 18 Dec. 2010). *Finite element method*. Available: http://en.wikipedia.org/wiki/Finite_element_method
- [68] (2010, 18 Dec. 2010). *Finite-difference time-domain method*. Available: http://en.wikipedia.org/wiki/Finite-difference_time-domain_method
- [69] Y. Ishibashi, *et al.*, “Dispersion Relation of the Third Order Nonlinear Dielectric Susceptibility in Poly-dispersive System,” *Journal of the Physical Society of Japan*, vol. 73, pp. 2323-2325, 2004.
- [70] M. Florjanczyk, *et al.*, “Multiaperture planar waveguide spectrometer formed by arrayed Mach-Zehnder interferometers,” *Optics Express*, vol. 15, pp. 18176-18189, 2007.

- [71] B. Vincent, *et al.*, “Green light generation in a periodically poled Zn-doped LiNbO₃ planar waveguide fabricated by He⁺ implantation,” *Applied Physics B: Lasers and Optics*, vol. 89, pp. 235-239, 2007.
- [72] J. J. Perina, *et al.*, “Squeezed-light generation in a nonlinear planar waveguide with a periodic corrugation,” *Physical Review A (Atomic, Molecular, and Optical Physics)*, vol. 76, pp. 033813-14, 2007.
- [73] M. Ayre, *et al.*, “Photonic crystal waveguides for coarse-selectivity devices,” *Photonics and Nanostructures - Fundamentals and Applications*, vol. 6, pp. 19-25, 2008.
- [74] L. Xiao, *et al.*, “High-power Nd:YAG planar waveguide laser with YAG and Al₂O₃ claddings,” *Optics Communications*, vol. 281, pp. 3781-3785, 2008.
- [75] L. Geng and J. C. Wright, “Measurement of the resonant third-order nonlinear susceptibility of C60 by nondegenerate four-wave mixing,” *Chemical Physics Letters*, vol. 249, pp. 105-111, 1996.
- [76] H. B. Liao, *et al.*, “Large third-order optical nonlinearity in Au:TiO₂ composite films measured on a femtosecond time scale,” *Applied Physics Letters*, vol. 72, pp. 1817-1819, 1998.
- [77] B. Derkowska, *et al.*, “Study of the third order nonlinear optical properties of Zn_{1-x}Mg_xSe and Cd_{1-x}Mg_xSe crystals,” *Opto-Electronics Review*, vol. 16, pp. 8-11, 2008.
- [78] U. Gubler and C. Bosshard, “Optical third-harmonic generation of fused silica in gas atmosphere: Absolute value of the third-order nonlinear optical susceptibility $\chi^{(3)}$,” *Physical Review B*, vol. 61, p. 10702, 2000.
- [79] G. R. Meredith, *et al.*, “Third-order optical susceptibility determination by third harmonic generation. I,” *The Journal of Chemical Physics*, vol. 78, pp. 1533-1542, 1983.
- [80] T. Kobayashi, *et al.*, “Multiplex method for the measurement of nonlinear susceptibility spectrum applied to third-harmonic generation in a polydiacetylene,” *Chemical Physics Letters*, vol. 433, pp. 379-384, 2007.
- [81] S. Debrus, *et al.*, “Z-scan determination of the third-order optical nonlinearity of gold:silica nanocomposites,” *Journal of Applied Physics*, vol. 88, pp. 4469-4475, 2000.

- [82] M. Ghotbi, *et al.*, “Efficient third harmonic generation of microjoule picosecond pulses at 355 nm in BiB₃O₆,” *Applied Physics Letters*, vol. 89, pp. 173124-3, 2006.
- [83] D. Stoker, *et al.*, “Optical third-harmonic generation using ultrashort laser pulses,” *Physical Review A (Atomic, Molecular, and Optical Physics)*, vol. 71, pp. 061802-4, 2005.
- [84] H. Guillet de Chatellus and E. Freysz, “Measurement of the third-order susceptibility of glasses by EFISH of femtosecond pulses,” *Optics Express*, vol. 9, pp. 586-591, 2001.
- [85] C.-J. Zhang, *et al.*, “Third harmonic generation of semiconductor carbon nanotubes,” *Chemical Physics Letters*, vol. 433, pp. 101-104, 2006.
- [86] P. S. Banks, *et al.*, “High-intensity third-harmonic generation,” *Journal of the Optical Society of America B*, vol. 19, pp. 102-118, 2002.
- [87] J. D. Mills, *et al.*, “Observation of the developing optical continuum along a nonlinear waveguide,” *Opt. Lett.*, vol. 31, pp. 2459-2461, 2006.
- [88] R. C. Eckardt, *et al.*, “Absolute and relative nonlinear optical coefficients of KDP, KD*P, BaB₂O₄, LiIO₃, MgO:LiNbO₃, and KTP measured by phase-matched second-harmonic generation,” *IEEE Journal of Quantum Electronics*, vol. 26, pp. 922-933, 1990.
- [89] H. Kishida, *et al.*, “Dispersion relation in the third-order electric susceptibility for polysilane film,” *Physical Review Letters*, vol. 70, p. 3724, 1993.
- [90] H. Murakami, *et al.*, “Determination of Third-Order Optical Nonlinearity Dispersion of 1-Methyl-1'-Octadecyl-2,2'-Cyanine Perchlorate Langmuir-Blodgett Films Using Electroabsorption Spectroscopy,” *Japanese Journal of Applied Physics*, vol. 39, pp. 5838-5841, 2000.
- [91] F. D'Amore, *et al.*, “Sputtered stoichiometric TeO₂ glass films: Dispersion of linear and nonlinear optical properties,” *Journal of Applied Physics*, vol. 94, pp. 1654-1661, 2003.
- [92] A. Arranz, *et al.*, “Electronic structure of stoichiometric and reduced Ta₂O₅ surfaces determined by resonant photoemission,” *Physical Review B*, vol. 66, p. 075420, 2002.

- [93] R. Trebino, *et al.*, “Measuring ultrashort laser pulses in the time-frequency domain using frequency-resolved optical gating,” *Review of Scientific Instruments*, vol. 68, pp. 3277-3295, 1997.
- [94] C. E. Finlayson, *et al.*, “Slow light and chromatic temporal dispersion in photonic crystal waveguides using femtosecond time of flight,” *Physical Review E*, vol. 73, pp. 016619-10, 2006.
- [95] R. Y. Chen, *et al.*, “Chi 3 dispersion in planar tantalum pentoxide waveguides in the telecommunications window,” *Optics Letters*, vol. 34, pp. 1135-1137, Apr 1 2009.
- [96] R. Lytel, “Pump-Depletion Effects in Noncollinear Degenerate 4-Wave-Mixing in Kerr Media,” *Journal of the Optical Society of America B-Optical Physics*, vol. 3, pp. 1580-1584, Nov 1986.
- [97] M. D. B. Charlton, *et al.*, “Realisation of ultra-low loss photonic crystal slab waveguide devices,” *Microelectronics Journal*, vol. 36, pp. 277-281, 2005.
- [98] A. Aguirre, *et al.*, “Continuum generation in a novel photonic crystal fiber for ultrahigh resolution optical coherence tomography at 800 nm and 1300 nm,” *Opt. Express*, vol. 14, pp. 1145-1160, 2006.
- [99] H. Wang and A. M. Rollins, “Optimization of dual-band continuum light source for ultrahigh-resolution optical coherence tomography,” *Applied Optics*, vol. 46, pp. 1787-1794, 04 2007.
- [100] F. Spoler, *et al.*, “Simultaneous dual-band ultra-high resolution optical coherence tomography,” *Optics Express*, vol. 15, pp. 10832-10841, Aug 2007.
- [101] A. G. Podoleanu, *et al.*, “Simultaneous low coherence interferometry imaging at two depths using an integrated optic modulator,” *Optics Communications*, vol. 191, pp. 21-30, 2001.
- [102] Y. Jiang, *et al.*, “Second-harmonic optical coherence tomography,” *Opt. Lett.*, vol. 29, pp. 1090-1092, 2004.
- [103] M. V. Sarunic, *et al.*, “Spectral domain second-harmonic optical coherence tomography,” *Opt. Lett.*, vol. 30, pp. 2391-2393, 2005.
- [104] Y. T. Pan, *et al.*, “Enhancing early bladder cancer detection with fluorescence-guided endoscopic optical coherent tomography,” *Opt. Lett.*, vol. 28, pp. 2485-2487, 2003.

- [105] Z. G. Wang, *et al.*, “Fluorescence Guided Optical Coherence Tomography for The Diagnosis of Early Bladder Cancer in a Rat Model,” *The Journal of Urology*, vol. 174, pp. 2376-2381, 2005.
- [106] J. Takeda, *et al.*, “Time-resolved luminescence spectroscopy by the optical Kerr-gate method applicable to ultrafast relaxation processes,” *Physical Review B*, vol. 62, pp. 10083-10087, 2000.
- [107] M. C. Netti, *et al.*, “Separation of photonic crystal waveguides modes using femtosecond time-of-flight,” *Applied Physics Letters*, vol. 81, pp. 3927-3929, 2002.
- [108] H. Garcia, *et al.*, “New approach to the measurement of the nonlinear refractive index of short (< 25 m) lengths of silica and erbium-doped fibers,” *Optics Letters*, vol. 28, pp. 1796-1798, 2003.
- [109] G. von Freymann, *et al.*, “Measurement of group velocity dispersion for finite size three-dimensional photonic crystals in the near-infrared spectral region,” *Applied Physics Letters*, vol. 86, pp. 053108-3, 2005.
- [110] C. Tun, *et al.*, “Fast-Light Based Pulse Compression in 2-D Photonic Crystal Waveguides,” *Lightwave Technology, Journal of*, vol. 25, pp. 2590-2598, 2007.
- [111] Z.-Y. Li and K.-M. Ho, “Light propagation in semi-infinite photonic crystals and related waveguide structures,” *Physical Review B*, vol. 68, p. 155101, 2003.
- [112] A. V. Andreev, *et al.*, “Compression of femtosecond laser pulses in thin one-dimensional photonic crystals,” *Physical Review E*, vol. 63, p. 016602, 2000.
- [113] (18 Dec. 2010). *VECSEL basics*. Available: <http://www.vecsel.phys.soton.ac.uk/basics.html>
- [114] L. Xu, *et al.*, “Programmable chirp compensation for 6-fs pulse generation with a prism-pair-formed pulse shaper,” *Quantum Electronics, IEEE Journal of*, vol. 36, pp. 893-899, 2000.
- [115] V. G. Savitski, *et al.*, “Cavity-dumping of a semiconductor disk laser for the generation of wavelength-tunable micro-Joule nanosecond pulses,” *Optics Express*, vol. 18, pp. 11933-11941, 2010.
- [116] K. G. Wilcox, *et al.*, “High Peak Power Femtosecond Pulse Passively Mode-Locked Vertical-External-Cavity Surface-Emitting Laser,” *Photonics Technology Letters, IEEE*, vol. 22, pp. 1021-1023, 2010.

- [117] M. E. Barnes, *et al.*, “Gain bandwidth characterization of surface-emitting quantum well laser gain structures for femtosecond operation,” *Optics Express*, vol. 18, pp. 21330-21341, 2010.
- [118] K. G. Wilcox, *et al.*, “Subpicosecond quantum dot saturable absorber mode-locked semiconductor disk laser,” *Applied Physics Letters*, vol. 94, pp. 251105-3, 2009.
- [119] A. H. Quarterman, *et al.*, “A passively mode-locked external-cavity semiconductor laser emitting 60-fs pulses,” *Nat Photon*, vol. 3, pp. 729-731, 2009.
- [120] B. J. Eggleton, *et al.*, “Compression of Optical Pulses Spectrally Broadened by Self-Phase Modulation with a Fiber Bragg Grating in Transmission,” *Applied Optics*, vol. 37, pp. 7055-7061, 1998.
- [121] R. E. Slusher and B. J. Eggleton, *Nonlinear photonic crystals*. Berlin ; London: Springer, 2003.